

AD-A260 671



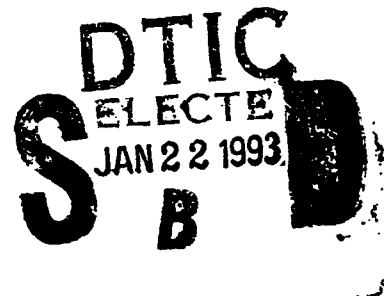
①

SHEAR-WAVE SEISMIC REFLECTION EXPLORATION FOR CAVITIES AND TUNNELS

VOLUME I – STUDY AND DESIGN OF TECHNIQUES

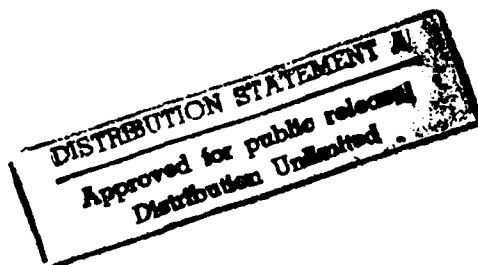
FINAL TECHNICAL REPORT

Contract No. DACA39-86-K-0017
SwRI Project No. 14-1421



Prepared for:

U.S. Army Engineer Waterways Experiment Station
Corps of Engineers
P.O. Box 631
Vicksburg, MS 39180-0631



September 1987

93-00968



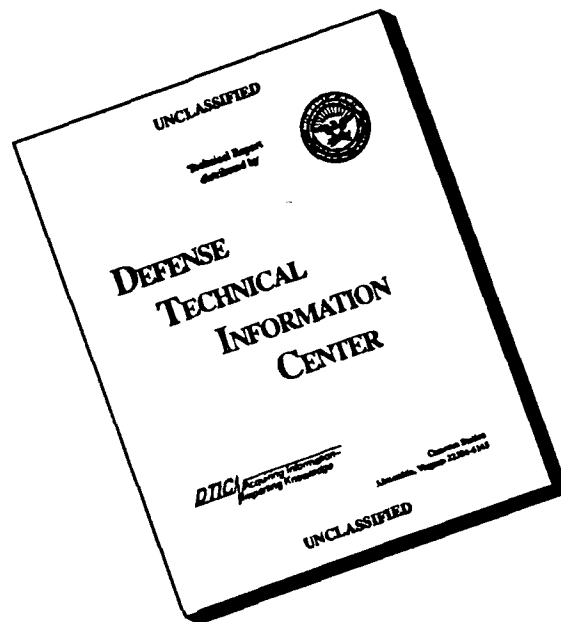
14288



SOUTHWEST RESEARCH INSTITUTE
SAN ANTONIO HOUSTON

93 1 19 024

DISCLAIMER NOTICE



THIS DOCUMENT IS BEST QUALITY AVAILABLE. THE COPY FURNISHED TO DTIC CONTAINED A SIGNIFICANT NUMBER OF PAGES WHICH DO NOT REPRODUCE LEGIBLY.

305
Unclassified

US-C-E-Property of the
United States Government

410765.2
084
1901 v.1

SECURITY CLASSIFICATION OF THIS PAGE

REPORT DOCUMENTATION PAGE

Form Approved
OMB No 0704-0188
Exp Date Jun 30 1986

REPORT SECURITY CLASSIFICATION Unclassified		1b RESTRICTIVE MARKINGS	
SECURITY CLASSIFICATION AUTHORITY		3 DISTRIBUTION/AVAILABILITY OF REPORT Approved for public release; Distribution unlimited	
DECLASSIFICATION/DOWNGRADING SCHEDULE		5 MONITORING ORGANIZATION REPORT NUMBER(S)	
PERFORMING ORGANIZATION REPORT NUMBER(S)		7a NAME OF MONITORING ORGANIZATION USAEWES Geotechnical Laboratory	
NAME OF PERFORMING ORGANIZATION outhwest Research Institute	6b OFFICE SYMBOL (if applicable)	7b ADDRESS (City, State, and ZIP Code) P.O. Box 631 Vicksburg, MS 39180-0631	
ADDRESS (City, State, and ZIP Code) O. Box 28510, 6220 Culebra Road San Antonio, TX 78284		9 PROCUREMENT INSTRUMENT IDENTIFICATION NUMBER DACA39-86-K-0017	
NAME OF FUNDING/SPONSORING ORGANIZATION S. Army Belvoir Research, Development & Engineering Center	8b OFFICE SYMBOL (if applicable)	10 SOURCE OF FUNDING NUMBERS	
ADDRESS (City, State, and ZIP Code) Fort Belvoir, VA 22060-5606		PROGRAM ELEMENT NO	PROJECT NO
		TASK NO	WORK UNIT ACCESSION NO

TITLE (Include Security Classification) Shear-Wave Seismic Reflection Exploration for Cavities and Tunnels, Volumes I and II.			
PERSONAL AUTHOR(S) Wen, Thomas E., Parra, Jorge O., and Biard, James C.			
1 TYPE OF REPORT Final Report	13b TIME COVERED FROM TO	14 DATE OF REPORT (Year, Month, Day) January 1988	15 PAGE COUNT

SUPPLEMENTARY NOTATION			
------------------------	--	--	--

COSAT CODES			18 SUBJECT TERMS (Continue on reverse if necessary and identify by block number) Tunnels Tunnel Detection Seismic Reflection Polarized Waves Cavities
FIELD	GROUP	SUB-GROUP	

ABSTRACT (Continue on reverse if necessary and identify by block number) A theoretical analysis of horizontally polarized shear (SH) waves was performed to determine the seismic reflection characteristics and practical seismic frequency range for detecting cylindrical cavities representative of man-made tunnels. The two-dimensional analytical model consists of an SH-wave line source in an absorptive two-layered half-space containing a cylindrical cavity in a high-quality bedrock layer underlying a lossy low-velocity surface layer. Seismic wave scattering patterns and synthetic reflection seismograms were computed to illustrate the reflection response of SH waves polarized parallel to the cavity axis. The influence of the lossy surface layer on the reflected SH waves was found to be significant enough to require the use of subsurface-coupled source and detectors for practical detection of the cavity. Based upon these analytical model results, technical specifications were developed for a high-resolution SH-wave seismic exploration system designed specifically for search and detection of tunnels. A borehole-coupled asymmetrical (cont'd)	
---	--

DISTRIBUTION/AVAILABILITY OF ABSTRACT <input checked="" type="checkbox"/> UNCLASSIFIED/UNLIMITED <input type="checkbox"/> SAME AS RPT <input type="checkbox"/> DTIC USERS		21 ABSTRACT SECURITY CLASSIFICATION Unclassified	
NAME OF RESPONSIBLE INDIVIDUAL		22b TELEPHONE (Include Area Code)	22c OFFICE SYMBOL

19. Abstract (cont'd)

force transducer operating on the electrical arc discharge principle is recommended as the source device and three-component borehole-coupled seismic detectors are recommended for complete SH-wave data acquisition. This seismic exploration system, designed to operate in the frequency range of 400-1,600 Hz together with specialized data processing techniques capable of preserving the high-frequency timing accuracies in the seismic signals and enhancing reflections from localized cavity targets, is recommended for future prototype development and field evaluation.

DATE NOT YET EXPECTED 5

Accession For	
NTIS GRA&I	<input checked="" type="checkbox"/>
DTIC TAB	<input type="checkbox"/>
Unannounced	<input type="checkbox"/>
Justification	
By	
Distribution/	
Availability Codes	
Dist	Avail and/or Special
A-1	

PREFACE

This report was prepared by Dr. Thomas E. Owen, Dr. Jorge O. Parra, and Mr. James C. Biard of the Department of Geosciences, Electronic System Division, Southwest Research Institute, under contract number DACA39-86-K-0017. It represents the first task in investigating and applying high-resolution shear-wave seismic reflection exploration techniques to the problem of search and detection of subversive intrusion tunnels of military concern. The study was done during FY 87 under funding provided by LABCOM Headquarters to the U.S. Army Engineering Waterways Experiment Station (WES) as a part of the research and development effort to solve the Korean tunneling problem. Dr. Donald Eccleshall of the U.S. Army Ballistic Research Laboratory, Army Material Command (AMC), is the technical reviewer of the overall tunnel detection program.

This report is presented in two volumes. Volume I contains the body of the report including the technical results, discussions, and conclusions. Volume II contains the appendices in which the complete theoretical analyses, computer numerical calculations, and computer programs are presented.

Mr. Robert F. Ballard, Jr., Earthquake Engineering and Geophysics Division (EEGD), Geotechnical Laboratory (GL), WES, was the Contracting Officer's Representative and Program Manager and Coordinator for tunnel detection research. General supervision was provided by Dr. Arley G. Franklin, Chief, EEGD, and Dr. William F. Marcuson III, Chief, GL.

Commander and Director of WES during the publication of this report was Colonel Dwayne G. Lee, CE. Dr. Robert W. Whalin was the Technical Director.

TABLE OF CONTENTS

VOLUME I

	<u>Page</u>
LIST OF ILLUSTRATIONS	vi
LIST OF TABLES	x
I. INTRODUCTION AND SUMMARY OF PROJECT	1
A. Background	1
B. Summary of Project Efforts	1
II. THEORETICAL ANALYSIS OF SHEAR-WAVE MODELS	5
A. Status of Modeling Seismic Reflections from Tunnel Cavities	5
B. Rationale for Horizontally Polarized Shear Waves	5
C. Organization of Theoretical Model Analyses	7
D. SH-Wave Scattering from a Cylindrical Cavity in an Unbounded Homogeneous Medium	8
1. Formulation	8
2. Scattering of Plane SH Waves by a Cylindrical Cavity	10
3. Scattered Energy	17
4. Scattering of Spherical SH Waves by a Cylindrical Cavity ..	20
5. Scattering of Cylindrical SH Waves by a Cylindrical Cavity	24
6. Attenuation and Dispersion Along the Ray Path	26
E. SH-Wave Scattering from a Cylindrical Cavity in a Homogeneous Half-Space	28
1. Scattering of Spherical SH Waves by a Cylindrical Cavity ..	28
2. Scattering of Cylindrical SH Waves by a Cylindrical Cavity	35
F. SH-Wave Scattering from a Cylindrical Cavity in a Two-Layer Half-Space	39
1. Formulation	39
2. The Two-Layer Half-Space Green's Function	39
3. Incident SH-Wave Displacement for a Line Source in a Two-Layer Half-Space	45
4. Integral Equation Solution for SH-Wave Scattering from a Cylindrical Cavity in a Two-Layer Half-Space for a Detector in the Bedrock	48
a. Steady-State and Transient Solutions for the SH-Wave Particle Motion	51
b. Check of the Steady-State Solution	54
c. The Steady-State Approximate Solution	56
d. The High-Frequency Limit Approximation	57

TABLE OF CONTENTS (Cont'd)

	<u>Page</u>
5. Integral Equation Solution for SH-Wave Scattering from a Cylindrical Cavity in a Two-Layer Half-Space for the Detector in the Surface Layer	62
a. Steady-State and Transient Solutions	62
b. The High-Frequency Limit Approximation	65
6. Numerical Applications using the Transient Analytical Solutions	68
III. NUMERICAL EVALUATION OF MODELS	75
A. Plane Wave Source in a Lossless Unbounded Medium	75
1. Overview of the Plane Wave Analysis Computer Programs	75
a. Energy Scattering Cross-Section Calculation	76
b. SH-Wave Displacement Amplitude	76
B. Line Source in a Half-Space	77
1. Overview of the Program	77
a. Direct Wave Calculation	78
b. Scattered Wave Calculation	78
2. Line Source in a Homogeneous Half-Space	79
a. Lossless Medium	79
b. Lossy Medium	79
3. Line Source in a Two-Layer Lossy Half-Space	79
a. Source and Detector in Lower Layer	79
b. Source in Lower Layer and Detector in Surface Layer	80
C. Graphing Programs	80
IV. MODEL CALCULATIONS AND RESULTS	81
A. Plane SH Waves Scattered from a Cylindrical Cavity in a Lossless Unbounded Medium	81
1. Energy Scattering Cross-Section	81
2. Polar Amplitude Scattering Patterns	83
3. Seismic Survey Traverse Simulations	84
4. Hole-to-Hole SH-Wave Scattering Simulations	84

TABLE OF CONTENTS (Cont'd)

	<u>Page</u>
B. Synthetic Seismograms of SH Waves Scattered from a Cylindrical Tunnel in a Lossy Unbounded Medium	84
C. Synthetic Seismograms of SH Waves Scattered from a Cylindrical Cavity in a Two-Layered Lossy Half-Space	96
1. Effect of Surface Layer Attenuation	102
2. Effect of Surface Layer Thickness	102
3. Effect of Surface Layer SH-Wave Velocity	105
4. Direct-Wave Interference	105
V. SPECIALIZED TECHNIQUES FOR SH-WAVE TUNNEL DETECTION	111
A. Coherent Interference Reduction	111
1. Reduction of Direct Arrival Signals	111
2. Tunnel Reflection Signal Enhancement	113
3. Static Corrections	114
B. Use of Tunnel Reflection Models in Data Analysis	114
C. Field Data Acquisition System	115
1. Portable Seismic Data Recording System	116
2. Seismic Source Transducer	117
3. Seismic Detector Transducers	121
4. Custom Seismic Survey Cable	121
5. Roll-Along Switch	122
6. Borehole Auger Drill	122
7. Spare Parts	122
8. Field Vehicles	122
VI. CONCLUSIONS AND RECOMMENDATIONS	123
LIST OF REFERENCES	127
APPENDIX A - THE GREEN'S FUNCTION FOR THE UNBOUNDED MEDIUM	
APPENDIX B - THE INTEGRAL EQUATION FORMULATION	
APPENDIX C - FORMAL SOLUTION OF THE INTEGRAL P_{nm}	
APPENDIX D - ASYMPTOTIC SOLUTION OF THE INTEGRAL P_{nm}	
APPENDIX E - SH-WAVE SEISMIC PULSES RADIATED BY A LINE SOURCE IN A TWO-LAYER HALF-SPACE	
APPENDIX F - ASYMPTOTIC SOLUTION OF THE INTEGRAL Q_{nm}	
APPENDIX G - SYNTHETIC SEISMOGRAMS OF SH-WAVE REFLECTIONS FROM A CYLINDRICAL CAVITY IN A TWO-LAYER LOSSY HALF-SPACE	
APPENDIX H - COMPUTER PROGRAMS	

LIST OF ILLUSTRATIONS

<u>Figure</u>		<u>Page</u>
II-1	Geometry of Cylindrical Cavity and Coordinate System	9
II-2	Geometry of Plane SH-Wave Incident on a Cylindrical Cavity	10
II-3	Geometry of Spherical SH-Wave Incident on a Cylindrical Cavity	21
II-4	Cross-Section of a Cylindrical Cavity in a Homogeneous Half-Space	29
II-5	Whole-Space Containing Real and Image Cavities and Real and Image Sources Symmetrically Placed with Respect to the $y = h$ Plane	31
II-6	Two-Layer Half-Space for an SH-Wave Line Source and a Detector Located in the Bedrock	40
II-7	Geometry for the Green's Function in Polar Coordinates	43
II-8	SH-Wave Line Source and Cylindrical Cavity in the Bedrock	46
II-9	Geometry of the Zero Order Term Distances and Angles for SH-Wave Displacements (a) Scattered (b) Incident	61
II-10	Geometry of the Zero Order Term Distance and Angle for the Scattered and Incident SH-Wave Displacements	69
II-11	Two-Layer Earth Model and Line Source in the Bedrock (a) Detector in the Bedrock (b) Detector on the Surface of the Earth	71
II-12	The Total SH-Wave Transient Response for an SH-Line Source and a Detector in the Bedrock	72
II-13	The Total SH-Wave Transient Response Without the Direct Pulse for an SH-Line Source and a Detector in the Bedrock	73
II-14	Synthetic Seismic Pulses Associated with an SH-Line Source for the Bedrock and the Detector at the Surface of a Two-Layer Lossless Half-Space	74
IV-1	Geometry of Plane SH-Wave Incident on a Cylindrical Cavity in an Unbounded Medium	81
IV-2	Normalized Energy Scattering Cross-Section of a Cylindrical Cavity for an Incident Plane SH Wave	82

LIST OF ILLUSTRATIONS (Cont'd)

<u>Figure</u>		<u>Page</u>
IV-3	Plane SH-Wave Polar Amplitude Scattering from a Cylindrical Cavity (a) Total SH-Wave Polar Amplitude (b) SH-Wave Reflected Polar Amplitude Component	83
IV-4	Total Plane SH-Wave Amplitude Profiles Along a Simulated Reflection Seismic Detector Line	85
IV-5	Total Plane SH-Wave Amplitude Profiles Between Boreholes (a) Cavity Distance 5 meters (b) Cavity Distance 10 meters (c) Cavity Distance 15 meters (d) Cavity Distance 25 meters ...	86
IV-6	Geometry of Cylindrical Wave Line Source and Cylindrical Cavity in an Unbounded Medium	87
IV-7	Synthetic Seismogram of the Combined Direct and Reflected SH-Wave Particle Displacement for a 2-m Diameter Cylindrical Cavity and a SH-Line Source in a Lossless Medium Having an SH Velocity of 2,500 m/s. The Cavity is Located at a Depth of 50 m Below the Surface and the SH-Line Source is Located at the Position (-52 m, 0). The Traces Correspond to the Outputs of Detectors Spaced 2 m Apart.	88
IV-8	Synthetic Seismogram of Direct-Traveling SH-Waves Only from an SH-Line Source Located in a Lossless Medium at the Source Position (-52 m, 0). The SH-Wave Velocity in the Medium is 2,500 m/s and the Detector Spacing is 2 m. The Amplitude Plotting Scale Used in These Traces is Reduced by a Factor of 12.5 from that in Figure IV-7.	89
IV-9	Synthetic Seismogram of Direct-Traveling SH-Waves from an SH-Line Source Located in a Lossy Medium at the Source Position (-52 m, 0). The SH-Wave Velocity and the Quality Factor in the Medium are $c = 2,500$ m/s and $Q = 100$, Respectively. The Detector Spacing is 2 m. The Amplitude Plotting Scale Used in These Traces is the Same as that in Figure IV-8.	90
IV-10	Synthetic Seismogram of Scattered SH-Waves Only from a 2-m Diameter Cylindrical Cavity Located in a Lossless Medium at a Depth of 50 m. The SH-Wave Velocity is 2,500 m/s. The Detector Spacing is 2 m. The Amplitude Plotting Scale Used in These Traces is Increased by a Factor of Four Above that in Figure IV-7.	91
IV-11	Synthetic Seismograms of Scattered SH-Waves Only from a 2-m Diameter Cylindrical Cavity Located in a Lossy Medium at a Depth of 50 m. The SH-Wave Velocity and the Quality Factor in the Medium are $c = 2,500$ m/s and $Q = 100$, Respectively. The Detector Spacing is 2 m.	92

LIST OF ILLUSTRATIONS (Cont'd)

<u>Figure</u>		<u>Page</u>
IV-12	Synthetic Seismogram of Scattered SH-Waves Only from a 2-m Diameter Cylindrical Cavity Located in a Lossless Medium at a Depth of 50 m. The SH-Wave Velocity in the Medium is 2,500 m/s and the Detector Spacing is 2 m. The Amplitude Plotting Scale Used in These Traces is the Same as in Figure IV-10.	93
IV-13	Synthetic Seismogram of Scattered SH-Waves Only from a 2-m Diameter Cylindrical Cavity Located in a Lossy Medium at a Depth of 100 m. The SH-Wave Velocity and the Quality Factor of the Medium are $c = 2,500$ m/s and $Q = 100$, Respectively. The Detector Spacing is 2 m.	94
IV-14	The SH-Wave Pulse Source Signal and Its Frequency Spectrum	95
IV-15	Geometry and Model Parameters for an SH-Line Source and a Cylindrical Cavity in a Two-Layer Half-Space (a) Detectors in the Bedrock (b) Detectors at the Surface.	97
IV-16	Synthetic Seismograms of Scattered SH-Waves Only from a 2-m Diameter Cylindrical Cavity Located in a Two-Layer Lossy Half-Space at a Depth of 50 m. The Surface Layer Thickness is 5 m. The Constitutive Parameters of the Surface Layer and the Bedrock are $c_1 = 200$ m/sec, $\rho_1 = 1,500$ kg/m ³ , $c_2 = 2,500$ m/sec, and $\rho_2 = 2,700$ kg/m ³ . The Quality Factor of the Bedrock is $Q_2 = 100$. The Source and Array of Detectors Having a Detector Spacing of 2 m are in the Bedrock.	103
IV-17	Synthetic Seismograms of Scattered SH-Waves Only from a 2-m Diameter Cylindrical Cavity Located in a Two-Layer Lossy Half-Space at a Depth of 50 m. The Surface Layer Thickness is 5 m. The Constitutive Parameters of the Surface Layer and the Bedrock are $c_1 = 200$ m/sec, $\rho_1 = 1,500$ kg/m ³ , $c_2 = 2,500$ m/sec, and $\rho_2 = 2,700$ kg/m ³ . The Quality Factor of the Bedrock is $Q_2 = 100$. The Source is in the Bedrock, and the Array of Detectors Having a Detector Spacing of 2 m is at the Surface.	104
IV-18	Synthetic Seismograms of Scattered SH-Waves Only from a 2-m Diameter Cylindrical Cavity Located in a Two-Layer Lossy Half-Space at a Depth of 50 m. The Constitutive Parameters of the Surface Layer and the Bedrock are $c_1 = 200$ m/sec, $\rho_1 = 1,500$ kg/m ³ , $c_2 = 2,500$ m/sec, and $\rho_2 = 2,700$ kg/m ³ . The Quality Factors of the Surface Layer and Bedrock are $Q_1 = 50$ and $Q_2 = 100$, Respectively. The Source and the Array of Detectors Having a Detector Spacing of 2 m are in the Bedrock.	106

LIST OF ILLUSTRATIONS (Cont'd)

Figure		Page
IV-19	Synthetic Seismograms of Scattered SH-Waves Only from a 2-m Diameter Cylindrical Cavity Located in a Two-Layer Lossy Half-Space at a Depth of 50 m. The Constitutive Parameters of the Surface Layer and the Bedrock are $c_1 = 200$ m/sec, $\rho_1 = 1,500$ kg/m ³ , $c_2 = 2,500$ m/sec, and $\rho_2 = 2,700$ kg/m ³ . The Quality Factors of the Surface Layer and Bedrock are $Q_1 = 50$ and $Q_2 = 100$, Respectively. The Source is in the Bedrock, and the Array of Detectors Having a Detector Spacing of 2 m is at the Surface of the Earth.	107
IV-20	Synthetic Seismograms of Scattered SH-Waves Only from a 2-m Diameter Cylindrical Cavity Located in a Two-Layer Lossy Half-Space at a Depth of 50 m. The Surface Layer Thickness is 5 m. The Constitutive Parameters of the Surface Layer and the Bedrock are $\rho_1 = 1,500$ kg/m ³ , $c_2 = 2,500$ m/sec, and $\rho_2 = 2,700$ kg/m ³ . The Quality Factors of the Surface Layer and Bedrock are $Q_1 = 50$ and $Q_2 = 100$, Respectively. The Source and the Array of Detectors Having a Detector Spacing of 2 m are in the Bedrock.	108
IV-21	Synthetic Seismograms of Scattered SH-Waves Only from a 2-m Diameter Cylindrical Cavity Located in a Two-Layer Lossy Half-Space at a Depth of 50 m. The Surface Layer Thickness is 5 m. The Constitutive Parameters of the Surface Layer and the Bedrock are $\rho_1 = 1,500$ kg/m ³ , $c_2 = 2,500$ m/sec, and $\rho_2 = 2,700$ kg/m ³ . The Quality Factors of the Surface Layer and Bedrock are $Q_1 = 50$ and $Q_2 = 100$, Respectively. The Source is in the Bedrock, and the Array of Detectors Having a Detector Spacing of 2 m is at the Surface of the Earth.	109
V-1	Electrodeless Arc Discharge Transducer for Generating Asymmetrical Lateral Force in a Borehole	118
V-2	Preliminary Tests of Arc Discharge Pulse Transducer Modified to Produce Asymmetrical Pressure Force on Borehole Wall to Generate Horizontally Polarized Shear Waves	120

LIST OF TABLES

<u>Table</u>		<u>Page</u>
IV-1	List of Parameters for the Two-Layer Loss half-Space	98
IV-2	Two-Layer Model with Detectors in the Bedrock	99
IV-3	Two-Layer Model with Detectors at Surface	100
IV-4	Two-Layer Model Showing Higher Order Reflections in the Surface Layer	101
VI-1	Ratio of SH-Wave Tunnel Reflections to Direct SH-Wave Interference for the Layered Half-Space Model	124

I. INTRODUCTION AND SUMMARY OF PROJECT

A. Background

During the past decade, military priority has been given to the search, detection, mapping, and neutralization of subversive intrusion tunnels constructed by North Korea in the DMZ and into South Korea. Three such tunnels have been found to date and others are expected to exist. The fact that approximately eight years have elapsed since the third and largest tunnel was discovered, reinforced by evidence that such tunnel construction has been continued by North Korea, implies that additional tunnels could now be finished in construction and lie dormant for future subversive use by North Korea. Therefore, while current military efforts have emphasized the detection of the tunnel construction process using passive monitoring to detect and record seismic waves generated by such underground operations, there is now a need for other search methods capable of detecting dormant tunnels.

Extensive military drilling efforts are currently being used to investigate suspected tunnel construction activities inferred from the information collected and analyzed from passive seismic signal monitoring. This procedure has encouraged the use of relatively deep borehole drilling, combined with hole-to-hole electromagnetic probing, as a means of exploring for tunnel targets. As a supplemental method of tunnel exploration applicable to locating dormant tunnels, surface-based seismic reflection techniques are judged to offer good potential for efficient operation without the need for deep drilling. In this regard, high-resolution seismic reflection exploration techniques offer greater promise for detecting the subversive tunnel targets than any other surface-based geophysical technique.

B. Summary of Project Efforts

This project has been directed toward the study and evaluation of shear-wave reflection seismic exploration techniques for detecting cavities and tunnels. Shear waves offer certain specialized advantages for the tunnel detection application because the polarization of shear waves may be usefully aligned with the generally known directional orientation of the North Korea intrusion tunnels and, because of their lower velocity, shear waves offer inherently greater resolving power in comparison with compressional waves. Horizontally polarized shear waves, in particular, offer an added advantage in that the interference and masking effects caused by the directly transmitted waves are significantly less than those associated with compressional waves or vertically polarized shear waves.

Volume I - Study and Design of Techniques, as reported herein, presents a comprehensive study of horizontally polarized shear-wave exploration concepts specialized to the military tunnel search and detection problem. The primary efforts have been directed toward the formulation of analytical models representative of high-resolution shear-wave reflections and scattering from cylindrical tunnel targets in dissipative media and their numerical evaluation to produce characteristic synthetic seismograms. Special attention was given to comparing the effectiveness of surface-coupled and borehole-coupled seismic sources and detectors because of the significant differences in the time and

logistics required to apply these two methods in the field. Finally, an optimum shear-wave seismic reflection survey system and special-purpose data analysis techniques are specified for future development and application to military requirements for tunnel search and detection.

Tractable analytical solutions for the scattering of plane and cylindrical horizontally polarized (SH) waves from a cylindrical cavity located in homogeneous dissipative media were developed and computer model evaluations were carried out for cases of primary interest. The plane-wave analysis was useful in providing insights into the intrinsic scattering of SH waves polarized parallel to the axis of the cylindrical cavity. In particular, these results present the SH-wave energy scattering cross-section of a cylindrical tunnel cavity as a function of frequency, the angular amplitude scattering pattern about the cavity axis, and the steady-state frequency response of the cavity reflections as observed by a seismic detector array in a lossless homogeneous whole-space medium. The cylindrical wave analysis has provided synthetic seismograms illustrating reflections from the tunnel cavity in a lossless homogeneous half-space and in a two-layer half-space in which different dissipative absorption conditions may be specified for each layer.

The energy scattering cross-section of the cylindrical cavity for incident plane SH waves is greater than the projected area of a unit length of the cavity whenever the wavelength of the incident wave is equal to or less than the circumference of the cylindrical cavity. At longer wavelengths, the scattered signal amplitude decreases rapidly in proportion to the -2.5 power of frequency. At shorter wavelengths, the energy scattering cross-section becomes independent of frequency and approaches a value of twice the projected area of a unit length of the cavity at very high frequencies. These results are significant in that they indicate the most practical frequency range for detecting scattered signals from a tunnel cavity to be the two-octave range extending from a lower limit of approximately $f_1 = v/\pi D$ to an upper limit of approximately $f_2 = 4v/\pi D$. That is, for incident SH waves having wavelengths greater than about one circumference of the cylindrical cavity, the scattered energy rapidly becomes negligible whereas, for incident waves having wavelengths less than about one fourth of the cavity circumference, the increase in scattered energy becomes less significant as frequency increases, whereas the scattering and absorption of practical geological host media become more and more significant. In the granite rock host formations of Korea, the optimum SH-wave frequency range for detecting the tunnels of interest is approximately 400 Hz to 1,600 Hz.

The synthetic seismograms derived in this study are most important for the lossy two-layer half-space case. In this case, reflections from the cylindrical cavity form a hyperbolic pattern characteristic of the localized scattering target and are most readily detectable when the surface layer (representing a low shear strength surface soil layer) is either absent or when the seismic SH-wave source and detectors are installed in shallow drill holes that allow them to be coupled into competent ground. Conversely, when the detectors are installed at the surface of the soil layer, the absorptive effects of this lossy layer and added SH-wave multiple reflections in the direct source-to-detector waves impose excessive attenuation of the cavity reflections as well as unwanted masking effects. Therefore, a principal conclusion drawn from this analysis is that the SH-wave source and detectors

must be operated in shallow boreholes that provide access to reasonably high-quality ground capable of supporting shear-wave propagation in the desired frequency range.

A field data acquisition system, together with field procedures specialized to SH-wave operation, has been specified for future development and application in Korea. The source transducer recommended for this application is an asymmetrical-force arc discharge device designed for borehole operation and capable of generating repetitive SH-wave pulse signals having spectral frequency content up to about 2,000 Hz. The recommended seismic detectors consist of three-component geophones configured to clamp in shallow boreholes. The source and detectors are designed to be accurately oriented to optimize SH-wave data acquisition. Other components of the SH-wave seismic survey system include a 48-channel digital data recording system and a truck-mountable shallow borehole drill to provide a survey system capable of complete self-contained field operations.

Data processing techniques have been outlined taking into account the results of the analytical studies and derived synthetic seismograms as well as the practical aspects of high-resolution seismic signal analysis in realistic geological formations when the sought-after target is a localized tunnel cavity. The computer models developed as part of this project will be valuable aids in further studies of these specialized data processing techniques. They may also be incorporated into the data reduction process to provide a powerful means for recognizing and extracting predictable tunnel reflection signatures.

The overall results of this study and design of SH-wave seismic reflection exploration techniques are highly encouraging with respect to the successful search and detection of tunnel targets typical of those known to exist in Korea. However, to be successful, the necessary features of: (1) the unprecedented high-resolution SH-wave data acquisition system; (2) the specialized data acquisition field procedures and data quality control; and (3) the tunnel target-specialized data processing and analysis techniques must be recognized and carefully implemented and perfected.

II. THEORETICAL ANALYSIS OF SHEAR-WAVE MODELS

A. Status of Modeling of Seismic Reflections from Tunnel Cavities

Scattering of elastic waves by cylindrical cavities has been the subject of numerous investigations in the last decade. Most of these studies have dealt with the case of an infinite medium and a semi-infinite lossless half-space with regard to applications in the field of earthquake engineering. The main subject of interest has been in the analysis of stress amplitudes along the tunnel circumference rather than to investigate the problem of detectability of deep cavity targets.

The analysis of time harmonic elastic-wave propagation from a line (or point) source in a half-space or from a cavity in an infinite elastic medium are now a well-known part of the literature on elastic-wave propagation. [Miklowitz (1960), Ewing et al. (1957), and Pao (1973) give a good collection of references.] The more difficult problem of propagation of elastic waves in a half-space containing a cylindrical cavity has been developed by Gregory (1967). The application of matched asymptotic expansions to obtain the scattered field when the wavelength is large compared with the linear dimensions of the cavity has been implemented by Datta et al. (1978).

Other references to seismic reflection from tunnel-like cavities that have been helpful and relevant to the present study include Lewis & Kraft (1976), Lewis et al. (1976), White (1965), Onda and Komaki (1968), Sato (1969), Kong (1986), El-Akily and Datta (1980), deHoop (1960), Apsel (1979), Achebach (1975), Aki and Larner (1970), Bouchon and Aki (1977), Garvin (1956), Ichikawa et al. (1975), Lamb (1904), Love (1944), Newlands (1952), and Wong et al. (1974).

The contributions of the present study have focused exclusively on horizontally polarized (SH) shear waves with emphasis on the detection of reflections from a cylindrical cavity in a dissipative medium. The case of a two-layer half-space composed of separately specified dissipative layer materials has provided a simple but realistic model of the typical field conditions to be encountered in Korea. Tunnel detection feasibility and the recommended field data acquisition techniques have been derived from this model as well as from the intermediate model formulations utilizing plane waves and cylindrical waves.

B. Rationale for Horizontally Polarized Shear Waves

Commercial seismic exploration methods rely primarily on the use of compressional waves generated by explosive shots or low-frequency vibrators and are generally directed toward mapping relatively large and deep subsurface geological structures and spatial trends as compared with resolving small localized anomalies. For this reason, conventional seismic methods are seldom required to achieve small target detection or unusually high resolution. However, when seismic detection of small anomalies such as man-made tunnels located at typically 100 diameters below surface is considered, the seismic detection sensitivity and resolution of the method must be increased substantially above that of conventional seismic systems. Further, since natural geologic anomalies comparable in size with the tunnel targets of interest may

be present in most metamorphic geological formations, the data processing requirements for accurate tunnel detection and interpretation are also more demanding than conventional seismic exploration requirements. Nevertheless, conventional reflection seismic methods are especially well developed for their industrial exploration purposes and can serve as the technical point of departure for developing the specialized methods needed for tunnel detection.

Detection of man-made tunnel cavities in the size range of two meters in diameter requires seismic signal wavelengths an order of magnitude shorter than those used in conventional seismic exploration. Thus, the spectral content of the seismic wave source must extend an order of magnitude higher in frequency than that provided by conventional explosive and vibrator sources. The lower velocity of shear waves in comparison with compressional waves offers an inherent advantage in that the high-frequency content of the source signal need be extended only by a factor of about 5 or 6 to provide a resolution limit comparable with that obtained using compressional waves. The polarization characteristics of shear waves offer an additional degree of freedom over compressional waves and, since tunnel targets are elongated and directionally oriented anomalies, this polarization parameter may be used to good advantage in the preferential detection of such targets.

Horizontally polarized shear waves have several distinctive advantages over compressional waves and vertically polarized shear waves with respect to high-resolution seismic reflection exploration for tunnels. These advantages stem from the horizontal orientation of the shear-wave particle motions and their inherently low propagation velocity in comparison with compressional waves. These advantages are summarized as follows:

(1) Horizontal Polarization Orientation

- Polarization alignment with the tunnel axis produces stronger reflections than compressional waves of the same wavelength because the incident compressional-wave energy is partitioned, upon reflection, into components of compressional waves and vertically polarized shear waves, whereas incident SH waves are reflected without a change in wave type.
- Polarization alignment of SH waves with geological layer structures in the tunnel host medium offers similar advantages to alignment with the tunnel axis since SH-wave energy transmitted (or reflected) from a layer interface is not partitioned to other wave types when the particle motions are in the plane of the interface.

(2) Low-Velocity Propagation

- The shorter wavelength of shear waves in comparison with compressional waves provides greater detection sensitivity and spatial resolution of tunnel targets than compressional waves of comparable frequency spectrum. This effective reduction in source signal frequency spectrum for SH waves offers the prospect of less dissipative attenuation along the two-way signal propagation path and places less demand on the source transducer to generate the high-frequency signals necessary for useful target detection.

(3) Reduction of Coherent Noise

- Compressional-wave sources at or near the surface generate Rayleigh waves (surface waves) which often interfere with body waves (compressional or shear waves) reflecting from subsurface anomalies. Since surface waves consist of vertical and radial shear-particle motions, seismic detectors designed to detect compressional waves also respond to surface waves. In contrast, seismic detectors designed to detect SH waves do not respond to surface waves associated with the SH-wave source transducer or other compressional wave-noise sources.
- Shear waves in the frequency range appropriate for tunnel detection experience strong attenuation effects in the near-surface weathered layer. Therefore, direct excitation of the detectors by the SH-wave source transducer will be advantageously reduced.
- The dissipative attenuation of SH waves in unconsolidated weathered materials near the surface imposes the need to drill down through such materials to place the SH source and detectors in competent ground. (Note: This requirement does not necessarily require drilling to bedrock depths.) Although this requirement places extra demands on the field data acquisition process, such drilling and competent transducer placements are also demanded by high-resolution compressional-wave techniques.
- Since the polarization of the SH-wave source may not always be in alignment with the tunnel axis to give the strongest SH-wave reflections, a seismic data collection system which records two orthogonal horizontal components will aid in improving the reflected SH-wave signal-to-noise ratio and may yield useful information on the target alignment direction relative to the seismic survey line. (Note: Misalignments between the SH-wave polarization orientation and the tunnel axis will result in conversion of part of the incident SH-wave energy to compressional and vertically polarized shear waves. Since such wave-type conversion may be unique to tunnel cavity geometries, a seismic data collection system which records three orthogonal components of particle motion is recommended for use in the field.)

C. Organization of Theoretical Model Analyses

The shear-wave model studies presented in this report are organized in three parts. The first part addresses the questions of SH-wave scattering from a cylindrical cavity in an unbounded homogeneous host medium. Ideas and results from this simplified stage of analysis aided in obtaining a useful perspective of the overall analysis problem and were valuable in planning the more extensive parts of the theoretical study. The second part addresses SH-wave scattering from a cylindrical cavity in a homogeneous half-space. Together, the analyses presented in these two parts cover the cases of a plane

wave source, an infinite line source, and a point source with emphasis on polar amplitude scattering patterns, seismic energy reflection cross-section, and reflection responses derived from source and detector geometries associated with reflection seismic surveys for relatively deep tunnel cavities. An extension of this theoretical analysis includes the case of SH-wave scattering from a cylindrical cavity in a lossy unbounded medium.

The third part of this investigation presents the analysis of SH-wave scattering from a cylindrical cavity in a lossy two-layer half-space. This analysis, not reported in the literature yet, covers the cases of an infinite line source in the bedrock with the detector located either in the bedrock or at the top of the surface layer. To reduce the computations necessary to produce synthetic seismograms and as a check of the analysis, the high-frequency approximation for the total SH-wave particle displacement was also derived and evaluated. In addition, the analytical solution of the transient SH-wave displacement in the presence of a two-layer half-space was developed using the Cagniard-deHoop method of inversion. The classical first motion approximation (Helmberger, 1968) for a disturbance in an elastic medium was also implemented in this analytical solution.

Theoretical highlights and graphical displays of computer calculations are presented in each part to describe and illustrate the derived results. The complete theoretical analyses together with supplemental data displays and the documented computer model programs are presented in Volume II - Appendices of this report.

D. SH-Wave Scattering from a Cylindrical Cavity in an Unbounded Homogeneous Medium

The steady-state solution for elastic-wave scattering from an infinitely long cylindrical cavity in an unbounded homogeneous lossless solid medium is developed for incident plane SH waves and for incident spherical SH waves. The spherical SH waves are generated by a point horizontal force within the unbounded medium. Formal analytical expressions are developed for the elastic-wave displacement of scattered waves at any point around the cylindrical cavity for incident plane waves oriented parallel to the axis of the cavity or for point-source SH waves having polarization oriented parallel to the axis of the cavity. In addition, theoretical analysis of the steady-state elastic-wave scattering from an infinitely long cylindrical cavity in a homogeneous lossless solid half-space is developed for an SH-wave point source and for an SH-wave line source at any position within the half-space. Formal analytical expressions are derived for the elastic-wave displacements to investigate the influence of the free-surface interface on the scattering of SH waves from cylindrical tunnel targets.

1. Formulation

For elastic waves in an isotropic solid body, the vector motional displacement, \vec{u} , in the absence of body forces, satisfies the displacement equation of motion:

$$(\lambda + \mu) \nabla \nabla \cdot \vec{u} + \mu \nabla^2 \vec{u} = \rho \frac{d^2 \vec{u}}{dt^2}, \quad (1)$$

where λ and μ are Lamé's elastic moduli and ρ is the mass density of the body. In the most general case, the displacement components in Equation (1) are functions of the time, t , and the three spatial coordinates x , y , and z .

For a tunnel or cylindrical cavity subject to a special distribution of external forces, various approximations can be made regarding the displacement components in order to simplify the equation of motion given by Equation (1). For the long cylindrical tunnel shown in Figure II-1, the motion can be classified as either anti-plane strain or plane strain in accordance with how the external forces are applied. When a distributed force is applied parallel to the cavity length direction z such that the dominant wave displacement is in that direction and has constant magnitude along the z -axis, the motion is in the category of anti-plane strain. If the force is applied perpendicular to the characteristic length of the cavity and is distributed uniformly in the length direction, there is no displacement along the length direction. In this case, the motion is defined as plane strain.

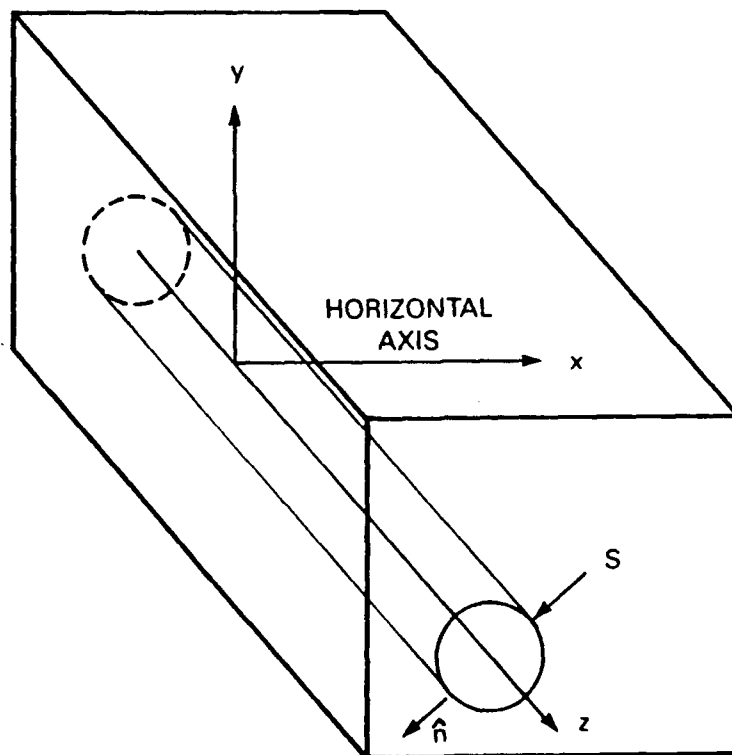


FIGURE II-1. GEOMETRY OF CYLINDRICAL CAVITY AND COORDINATE SYSTEM

For the cylindrical cavity shown in Figure II-1, the anti-plane strain displacement is derived as

$$\begin{aligned}
 u_x &= 0 \\
 u_y &= 0 \\
 u_z &= w(x,y,z) .
 \end{aligned}
 \tag{2}$$

The assumption that the displacement is restricted to the z-axis reduces the equation of motion given in Equation (1) to a single scalar-wave equation

$$\mu \nabla^2 w(x,y,z) = \rho \frac{\partial^2 w}{\partial t^2} , \tag{3}$$

where:

$$\nabla^2 \equiv \frac{\partial^2}{\partial x^2} + \frac{\partial^2}{\partial y^2} .$$

Under the assumption of anti-plane strain, the dilatation $\nabla \cdot \vec{u}$ is zero (Aki and Richards, 1980) and the resulting wave is a rotational shear wave. Because the displacement vector of the wave is always parallel to the z-axis, which for convenience is assumed to be horizontal, the waves are horizontally polarized shear (SH) waves.

2. Scattering of Plane SH Waves by a Cylindrical Cavity

The cylindrical cavity illustrated in Figure II-2 has a radius, a , and is infinite in length in the cylindrical coordinate system (r, ϕ, z) . The lossless elastic medium external to the cylinder has a density, ρ , and a shear

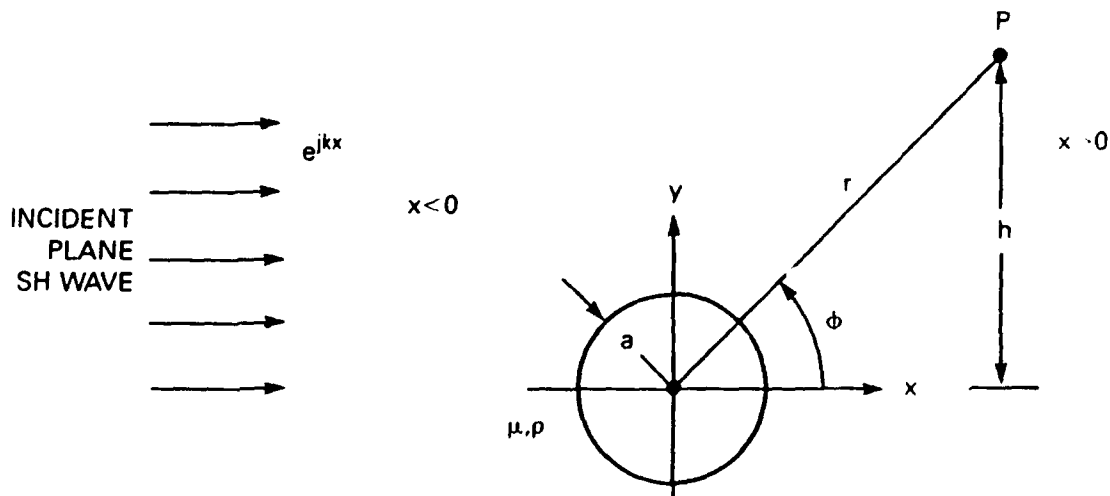


FIGURE II-2. GEOMETRY OF PLANE SH-WAVE INCIDENT ON A CYLINDRICAL CAVITY

modulus, μ . To consider the scattering of shear waves by the cylindrical cavity, an incident plane SH wave, having its particle motion polarized parallel to the axis of the cavity, is defined as

$$u_x = 0, u_y = 0, \text{ and } u_z = w(i) = e^{j(kx - \omega t)}, \quad (4)$$

where:

ω = angular frequency;
 $k = \omega/c_s$ = wave vector amplitude; and
 c_s = SH-wave velocity.

That is, the SH wave propagates in the positive x-direction with constant velocity, c_s , and angular frequency, ω . Upon impinging on the surface of the cavity, the incident wave is scattered. The scattered wave is also of the SH type and is represented by

$$u_x = 0, u_y = 0, \text{ and } u_z = w^{(s)}(x, y, t). \quad (5)$$

Since the geometry of the cavity is expressed in cylindrical coordinates, all field quantities will also be expressed in cylindrical coordinates. The nonvanishing displacement and stress components in cylindrical coordinates are

$$u_z = w(r, \phi, t)$$

$$\sigma_{rz} = \mu \frac{\partial w}{\partial r} \quad (6)$$

$$\sigma_{\phi z} = \mu \frac{1}{r} \frac{\partial w}{\partial \phi}$$

and the wave equation is

$$\frac{1}{r} \frac{\partial}{\partial r} \left(r \frac{\partial w}{\partial r} \right) + \frac{1}{r^2} \frac{\partial^2 w}{\partial \phi^2} = \frac{1}{c_s^2} \frac{\partial^2 w}{\partial t^2}. \quad (7)$$

Since there are no normal stresses on the surface of the cavity, the boundary condition is

$$\sigma_{rz} = \mu \frac{\partial w}{\partial r} = 0, \quad \text{at } r = a. \quad (8)$$

In addition, no disturbance should be present at $r = \infty$ other than the source plane SH wave.

Each particle on the surface of the cylinder acts as a secondary source generating scattered SH waves which are represented by the unknown function $w^{(s)}(x,y,t)$. To determine this secondary displacement, the cylindrical wave functions

$$H_n^{(1),(2)}(kr) \frac{\cos}{\sin}(n\phi), \quad \text{for } n = 0, 1, 2, \dots, \quad (9)$$

must be considered. These functions satisfy the Helmholtz equation in plane polar coordinates obtained by assuming a time dependence $w(x,y,t) = w(x,y,\omega)e^{-j\omega t}$; that is:

$$\left(\frac{\partial}{\partial r^2} + \frac{1}{r} \frac{\partial}{\partial r} + \frac{1}{r^2} \frac{\partial^2}{\partial \phi^2} + k^2 \right) w = 0. \quad (10)$$

The Hankel functions of the first kind, $H_n^{(1)}(kr)$, and of the second kind, $H_n^{(2)}(kr)$, are related to the Bessel functions of the first kind, $J_n(kr)$, and the second kind, $Y_n(kr)$, by the conjugate relationship

$$H_n^{(1),(2)}(kr) = J_n(kr) \pm jY_n(kr). \quad (11)$$

The wave functions given in Equation (9) are obtained by the method of separation of variables. If $w = R(r)\Theta(\phi)$, the Helmholtz condition of Equation (10) can be separated into two ordinary differential equations

$$r^2 \frac{d^2 R}{dr^2} + r \frac{dR}{dr} + (k^2 r^2 - n^2) R = 0, \quad (12)$$

and

$$\frac{d^2 \Theta}{d\phi^2} + n^2 \Theta = 0,$$

where n , an integer in this case, is the separation constant. The Θ equation is harmonic, giving rise to harmonic solutions in $\sin n\phi$ and $\cos n\phi$, and the R equation is Bessel's equation of order n for which $H_n^{(1)}(kr)$ and $H_n^{(2)}(kr)$ are solutions.

When the wave functions given by Equation (9) are combined with the time factor, $e^{-j\omega t}$, they represent cylindrical waves generated by a line source along the z -axis. From the asymptotic behavior of $H_n^{(1),(2)}(kr)$

$$H_n^{(1),(2)}(kr) \rightarrow \left(\frac{2}{\pi kr} \right)^{1/2} e^{\pm j[kr - (1+2n)\pi/4]}, \quad (13)$$

the function $H_n^{(1)}(kr) \cos n\phi e^{-j\omega t}$ represents a diverging or outgoing cylindrical wave; that is, the waves generated by the line source propagate away from the origin. Similarly, the function $H_n^{(2)}(kr) \cos n\phi e^{-j\omega t}$ represents a converging or incoming cylindrical wave. The boundary condition at $r = \infty$ in this problem eliminates the latter from the scattered waves, hence only the function $H_n^{(1)}(kr)$ is valid in the solution for the scattered waves.

Thus, the scattered-wave function, $w(s)$, may be expressed as

$$w(s)(r, \phi, t) = \sum_{n=0}^{\infty} A_n H_n^{(1)}(kr) \cos n\phi e^{-j\omega t} ; \quad (14)$$

where the A_n are the scattered-wave coefficients which represent the axially polarized shear component of the scattered-wave field in the host medium. The total SH-wave displacement at the measurement point, P, is given by the superposition of the incident and scattered functions,

$$u_z = w(r, \phi, t) = w(i) + w(s) . \quad (15)$$

To determine the unknown coefficients, A_n , from the boundary conditions at the surface of the cylindrical tunnel, the incident plane wave function given in Equation (4) is written in polar coordinates as

$$w(i) = e^{jkr} \cos \phi e^{-i\omega t} , \quad (16)$$

which may be expanded in complex Fourier series as

$$e^{jkr} \cos \phi = \sum_{n=-\infty}^{\infty} C_n(r) e^{jn\phi}$$

in which

$$\begin{aligned} C_n(r) &= \frac{1}{2\pi} \int_0^{2\pi} e^{jkr} \cos \phi e^{-jn\phi} d\phi , \\ &= \frac{1}{2\pi} \int_0^{2\pi} e^{jkr} \cos \phi \cos n\phi d\phi . \end{aligned}$$

The integral definition of the Bessel function

$$J_n(kr) = \frac{e^{-\frac{\pi}{2} jn}}{2\pi} \int_0^{2\pi} e^{jkr} \cos \phi \cos n\phi d\phi ,$$

may be compared with $C_n(r)$ to yield

$$C_n(r) = j^n J_n(kr) ,$$

and

$$e^{jkr \cos \phi} = \sum_{n=0}^{\infty} \epsilon_n j^n J_n(kr) \cos n\phi ,$$

where:

$$\epsilon_n = \begin{cases} 1, & \text{for } n = 0 \\ 2, & \text{for } n > 1. \end{cases} \quad (17)$$

Thus, the incident plane SH wave is expressed in polar coordinates as

$$w(i) = \sum_{n=0}^{\infty} \epsilon_n j^n J_n(kr) \cos n\phi e^{-j\omega t} .$$

Equation (17) may be regarded as a superposition of an infinite number of cylindrical shear waves, resulting in a pattern of wave propagation along the x-axis.

Omitting the time factor, $e^{-j\omega t}$, the total wave displacement at P, as given by Equation (15) is, therefore, represented by the infinite series,

$$w = \sum_{n=0}^{\infty} \{ \epsilon_n j^n J_n(kr) + A_n H_n^{(1)}(kr) \} \cos n\phi . \quad (18)$$

At the surface of the cylindrical cavity, the boundary condition given earlier in Equation (8) yields the coefficients, A_n , as

$$A_n = - \epsilon_n j^n \frac{J_n'(ka)}{H_n^{(1)'}(ka)} ; \quad \text{for } n = 0, 1, 2, \dots \pm \infty . \quad (19)$$

Using the Bessel identities

$$ka J_n'(ka) = n J_n(ka) - ka J_{n+1}(ka) ,$$

and

$$ka H_n^{(1)'}(ka) = n H_n^{(1)}(ka) - ka H_{n+1}^{(1)}(ka) ,$$

Equation (19) may be reduced to

$$A_n = -\varepsilon_n j^n \frac{nJ_n(ka) - kaJ_{n+1}(ka)}{nH_n^{(1)}(ka) - kaH_{n+1}^{(1)}(ka)}. \quad (20)$$

Thus, the SH-wave displacement, w , at a measurement point, P , near the cavity as given by the Fourier-Bessel sum as

$$w = \sum_{n=0}^{\infty} [\varepsilon_n j^n J_n(kr) + G_n(k, a, r)] \cos n\phi, \quad (21)$$

where:

$$G_n(k, a, r) = A_n(ka) H_n^{(1)}(kr).$$

To evaluate the amplitude and phase of the normalized SH-wave displacement for the vector-wave amplitude at $k = 0$, it is convenient to express the general solution of the scattered SH-wave displacement in terms of small argument Bessel functions. Thus, the scattered-wave coefficients, A_n , given in Equation (19) for small arguments, (i.e., as $ka \rightarrow 0$), are

$$A_n(ka) = \begin{cases} -j\pi \left(\frac{ka}{2}\right)^2; & \text{for } n = 0, \\ 2\pi j^{n+1} \left(\frac{ka}{2}\right)^{2n} [n!(n-1)!]; & \text{for } n > 1, \end{cases} \quad (22)$$

and for $k = 0$, the function $A_n = 0$ for $n = 0, 1, \dots, \infty$.

A similar analysis may be performed for the function $G_n(k, a, r) = A_n(ka) H_n^{(1)}(kr)$ as $ka \rightarrow 0$. Employing the asymptotic expression for the Hankel function for small arguments, i.e.,

$$H_n(kr) = \begin{cases} j \frac{2}{\pi} \log \frac{Ykr}{2}; & \text{for } n = 0 \\ -j \frac{(n-1)!}{\pi} \frac{1}{(kr/2)^n}; & \text{for } n > 1, \end{cases} \quad (23)$$

yields

$$G_n(k, a, r) = \begin{cases} 2 \left(\frac{ka}{2}\right)^2 \left[\log \left(\frac{Yr}{a}\right) + \log \left(\frac{ka}{2}\right) \right]; & \text{for } n = 0, \\ 2\pi j^n \left(\frac{ka}{2}\right)^n \frac{1}{n! \left(\frac{r}{a}\right)^n}; & \text{for } n > 1, \end{cases} \quad (24)$$

and, for $k = 0$, the function $G_n(k, a, r) = 0$ for $n = 0, 1, \dots, \infty$. The results for $k = 0$ in Equations (22) and (24) indicate that static non-oscillatory source forces do not propagate as elastic waves, a fact that serves as a check on the derived analytical expressions.

The final expression for the SH-wave displacement at any measurement position, P , in the vicinity of the cavity in terms of the function G_n is given by

$$w = e^{jkr} \cos \phi + \sum_{n=0}^{\infty} G_n(k, a, r) \cos n\phi, \quad \text{for } r > a \quad (25)$$

where:

$$G_n(k, a, r) = \begin{cases} 0; & \text{for } k = 0 \\ -\epsilon_n j^n \frac{[nJ_n(ka) - kaJ_{n+1}(ka)]H_n^{(1)}(kr)}{nH_n^{(1)}(ka) - kaH_{n+1}^{(1)}(ka)}; & \text{for } k > 0. \end{cases}$$

The total SH-wave displacement in Equation (25) may be expressed in real and imaginary components as

$$w = g_{SH} + jh_{SH}$$

where:

$$\begin{aligned} g_{SH} &= \text{Real } (w), \\ h_{SH} &= \text{Imag } (w). \end{aligned}$$

Then,

$$w = (g_{SH}^2 + h_{SH}^2)^{1/2} e^{j\phi^*}$$

in which

$$\phi^*(kr) = \tan^{-1}(h_{SH}/g_{SH}).$$

A normalized amplitude, $A_h(kr)$, and relative phase, $\phi_h(kr)$, may be defined by combining Equation (25) and the incident SH-wave displacement given in Equation (16). Thus,

$$A_h(kr) = (h_{SH}^2 + g_{SH}^2)^{1/2}$$

and

(26)

$$\phi_h(kr) = \tan^{-1}(h_{SH}/g_{SH}) - kx$$

where $\phi_h(kr)$ is in radians. Equations (25) and (26) were used to develop the displacement amplitude programs *dispa*, *dispb*, *dispcd*, and *dispe*, as well as the subroutine *plane-scatter* presented in Appendix H.

3. Scattered Energy

The rate of energy flow across a surface, S , having a unit normal vector, \hat{n} , is given as (Pao and Mow, 1973)

$$\dot{E} = -\iint_S \hat{n}_i \sigma_{ij} \dot{u}_j dS \quad (27)$$

in which \dot{E} is the total energy (strain energy and kinetic energy), $\hat{n} \cdot \sigma$ is the stress vector at the surface element, dS , and \dot{u} is the particle velocity. The integrand of Equation (27) is the actual rate of work done by the surface traction per unit area and, by the law of conservation of energy, this rate of work equals the flow of energy across a unit area per unit time.

In the case of steady-state waves, both the stresses and displacements, σ_{ij} and u_j , are harmonic functions of time which can be written as

$$\sigma_{ij}(x_k, t) = \bar{\sigma}_{ij}(x_k) e^{-j\omega t} \quad (28)$$

and

$$u_{ij}(x_k, t) = \bar{u}_j(x_k) e^{-j\omega t}$$

where $\bar{\sigma}_{ij}$ and \bar{u}_j are complex functions. Since $\text{Real}(u) = (u + u^*)/2$ where an asterisk indicates the complex conjugate of the corresponding quantity, then the energy may be expressed as

$$\dot{E} = -1/4 \iint_S \hat{n}_i (\sigma_{ij} \dot{u}_j + \sigma_{ij}^* \dot{u}_j^* + \sigma_{ij}^* \dot{u}_j + \sigma_{ij} \dot{u}_j^*) dS \quad (29)$$

Thus, the time average of energy flow is given by

$$\text{Ave}(\dot{E}) = \frac{1}{T} \int_0^T \dot{E} dt = -\frac{1}{4} j\omega \iint_S \hat{n}_i (\bar{\sigma}_{ij} \bar{u}_j^* - \bar{\sigma}_{ij}^* \bar{u}_j) dS \quad (30)$$

For an incident plane SH wave, the time average energy flux per unit area is

$$\text{Ave}(\dot{e}) = \frac{\text{Ave}(\dot{E})}{S} = -\frac{1}{4} j\omega (\bar{\sigma}_{xz} \bar{w}^* - \bar{\sigma}_{xz}^* \bar{w}) \quad (31)$$

where:

$$\bar{\sigma}_{xz} = \mu k e^{j(k_x x + \pi/2)}$$

$$\bar{\sigma}_{xz}^* = \mu k e^{-j(k_x x + \pi/2)}$$

$$\bar{w} = \mu k e^{jk_x x}$$

$$\bar{w}^* = \mu k e^{-jk_x x} .$$

After substitution, the time average energy carried by the incident wave per unit area is

$$\text{Ave}[\dot{e}(i)] = \frac{1}{2} \mu k \omega . \quad (32)$$

The energy flux across a cylindrical surface $r = R$ (per unit length of the cylinder) is

$$\text{Ave}(\dot{E}) = -\frac{1}{4} j\omega \int_0^{2\pi} [\bar{\sigma}_{rz} \bar{w}^* - \bar{\sigma}_{rz}^* \bar{w}]_{r=R} R d\phi . \quad (33)$$

Substituting the scattered-wave displacement, $w(s)$, and stress, $\sigma_{rz}(s)$, into Equation (33) leads to

$$\text{Ave}(\dot{E}) = -\frac{1}{4} j\pi\mu\omega \sum_{n=0}^{\infty} \left(\frac{2}{\epsilon_n}\right) A_n A_n^* kR [H_n'(kR) H_n^*(kR) - H_n'^*(kR) H_n(kR)] , \quad (34)$$

where use has been made of the orthogonality condition

$$\int_0^{2\pi} \cos m\phi \cos n\phi d\phi = \delta_{nm} ; n \neq m \neq 0 .$$

As $kR \rightarrow \infty$,

$$H_n(kR) \rightarrow \left(\frac{2}{\pi kR}\right)^{1/2} e^{j[kR - (n+1/2)\pi/2]}$$

and, hence, $H_n'(kR) \rightarrow jH_n(kR)$.

Thus, at a large distance, R ,

$$\text{Ave}[\dot{e}(s)] \rightarrow \mu k c_s [2A_0 A_0^* + \sum_{n=1}^{\infty} A_n A_n^*] . \quad (35)$$

A natural reference against which to compare the total scattered energy is the time average of the energy flux per unit area of the incident wave given by Equation (32). Thus, defining the ratio of these two energies by Q yields

$$Q = \frac{\text{Ave}[\dot{E}(s)]}{\text{Ave}[\dot{e}(1)]} = \frac{2}{k} [2A_0A_0^* + \sum_{n=1}^{\infty} A_nA_n^*] . \quad (36)$$

Since Q has the dimensions of area per unit length, the quantity $\text{Ave}[\dot{E}(s)]$ may be referred as the energy scattering cross-section of the cylindrical cavity. Thus, the normalized cross-section (or the dimensionless normalized cross-section) is given by

$$q_s \equiv \frac{Q}{2a} = \frac{2}{ka} \sum_{n=1}^{\infty} \alpha_n |A_n(ka)|^2 , \quad (37)$$

where:

$$\alpha_n = \begin{cases} 1 & ; \text{ for } n = 0 \\ 1/2 & ; \text{ for } n > 1 , \end{cases}$$

and the scattered-wave coefficients which represent the axially polarized shear component of the scattered wave field in the host medium is given by Equation (20).

Equation (37) may be used to calculate the normalized plane SH-wave scattering cross-section as a function of the variable ka to investigate the cavity scattering response at large distance and as a function of frequency. To calculate the angular distribution of the scattered energy at different wavelengths, the energy flux per unit area given by the integrand of Equation (33) may be used. That is,

$$\begin{aligned} \text{Ave}[\dot{e}(s)] = & \frac{-j\omega\mu}{4} \sum_{n=0}^{\infty} \sum_{m=0}^{\infty} [A_nA_m^*kH_n'(kr)H_m^*(kr) \\ & - A_n^*A_mkH_n'^*(kr)H_m(kr)] \times \cos n\phi \cos m\phi . \end{aligned} \quad (38)$$

In this case the dimensionless normalized scattering cross-section is given by

$$\gamma(\phi, r) = \frac{-1}{2k} \sum_{n=0}^{\infty} \sum_{m=0}^{\infty} [A_nA_m^*kH_n'(kr)H_m^*(kr) - A_n^*A_mkH_n'^*(kr)H_m(kr)] , \quad (39)$$

where the scattered-wave coefficients, A_n and A_m , are obtained from Equation (20) and

$$krH'_n(kr) = nH_n(kr) - krH_{n+1}(kr) ,$$

$$krH'^*_n(kr) = nH^*_n(kr) - krH^*_{n+1}(kr) ,$$

in which $H_n(kr) \equiv H^{(1)}_n(kr)$.

Equation (39) may be used to calculate the normalized plane SH-wave scattering cross-section as a function of the variable, ka , to investigate the change of direction of the scattered energy about the cavity.

4. Scattering of Spherical SH Waves by a Cylindrical Cavity

The geometry of the point source SH-wave scattering problem is illustrated in Figure II-3. An infinitely long cylindrical cavity of radius, a , occupies the space $r < a$ and $-\infty < z < \infty$ in the cylindrical coordinate system (r, ϕ, z) . The region $r > a$ external to the cavity has a density, ρ , and a shear modulus, μ . The SH-wave point source in the elastic medium acts along the z -axis (parallel to the cylinder) and consists of a body force, $f(t - R/c_s)$, at the position $S(-x_s, y_s, z_s)$. The axis of the cavity contains the origin of the cartesian coordinate system x, y , and z .

For the conditions stated, the SH-wave displacement, $u^{(1)}$, excited by the point source in a lossless unbounded medium is a solution of the inhomogeneous wave equation and is given by deHoop (1960) and White (1965).

$$u^{(1)} = \frac{f(t-R/c_s)}{4\pi\rho c_s^2 R} , \quad (40)$$

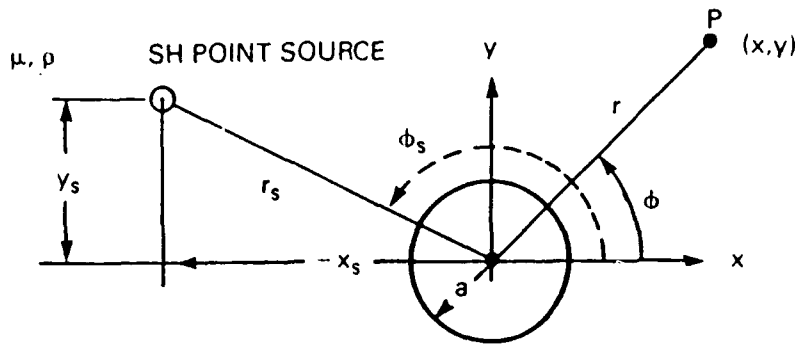
where:

c_s = SH-wave velocity

and

$$R = [(x-x_s)^2 + (y-y_s)^2 + (z-z_s)^2]^{1/2}$$

is the distance from the SH-wave source to the measurement point, P , at coordinates x, y , and z .



$$\phi = \tan^{-1} \frac{y}{x}$$

$$\phi_s = \tan^{-1} \frac{y_s}{-x_s}$$

FIGURE II-3. GEOMETRY OF SPHERICAL SH-WAVE INCIDENT ON A CYLINDRICAL CAVITY

In practical seismic exploration, the source usually generates short pulses and the objective is to obtain the transient solution of SH-wave scattering from buried tunnel targets. Since in most cases such transient solutions are difficult to obtain directly, the steady-state solution of the scattering of transient spherical SH waves may be synthesized by using the Fourier integral theorem. Thus, the incident SH-wave displacement may be expressed as

$$u^{(i)}(R, t) = \frac{1}{2\pi} \int_{-\infty}^{\infty} \bar{u}^{(i)}(R, \omega) e^{-j\omega t} d\omega \quad (41)$$

where:

$$\bar{u}^{(i)}(R, \omega) = \int_{-\infty}^{\infty} u^{(i)}(R, t) e^{+j\omega t} dt \quad (42)$$

provided that $\int_{-\infty}^{\infty} |u^{(i)}(R, t)| dt$ exists.

The quantity $\bar{u}^{(i)}$ is the Fourier transform of $u^{(i)}$. If Equation (40) is substituted into Equation (42), the SH-wave displacement excited by the point source is obtained in the frequency domain as

$$\bar{u}^{(i)} = \frac{F(\omega)}{4\pi\rho c_s^2} \frac{e^{jkR}}{R}, \quad (43)$$

where $F(\omega)$ is the body force in the frequency domain.

Introducing the known integral representation,

$$\frac{e^{jkR}}{R} = \frac{1}{2\pi} \int_{-\infty}^{\infty} [\pi j H_0^{(1)}(k_r |r - r_s|)] e^{j\beta(z - z_s)} d\beta, \quad (44)$$

where:

$$|r-r_s| = [(x-x_s)^2 + (y-y_s)^2]^{1/2},$$

$$k_r = (k^2 - \beta^2)^{1/2}.$$

The Hankel function in Equation (44) may be expanded in terms of cylindrical functions using the addition theorem for Bessel functions,

$$H_0^{(1)}(k_r |r-r_s|) = \begin{cases} \sum_{n=-\infty}^{\infty} H_n^{(1)}(r_s k_r) J_n(r k_r) e^{jn(\phi-\phi_s)}; & \text{for } r < r_s \\ \sum_{n=-\infty}^{\infty} H_n^{(1)}(r k_r) J_n(r_s k_r) e^{jn(\phi-\phi_s)}; & \text{for } r > r_s. \end{cases} \quad (45)$$

Since the point source is outside the cylindrical cavity, then the incident SH-wave displacement is expressed in terms of cylindrical functions as:

$$\begin{aligned} \bar{u}(i) &= \frac{jF(\omega)}{4\rho c_s^2} \frac{1}{2\pi} \int_{-\infty}^{\infty} \sum_{n=-\infty}^{\infty} H_n^{(1)}(r_s k_r) J_n(r k_r) e^{jn(\phi-\phi_s)} d\beta e^{j\beta(z-z_s)}. \\ &= \frac{jF(\omega)}{4\rho\pi c_s^2} \int_0^{\infty} \sum_{n=-\infty}^{\infty} H_n^{(1)}(r_s k_r) J_n(k_r r) e^{jn(\phi-\phi_s)} \cos \beta(z-z_s) d\beta. \end{aligned} \quad (46)$$

Introducing the integral summation operator defined by

$$\Gamma [\dots] = \int_0^{\infty} \sum_{n=-\infty}^{\infty} (\dots) e^{jn(\phi-\phi_s)} \cos \beta(z-z_s) d\beta, \quad (47)$$

the operator Γ is recognized as a Fourier integral in the z -direction along the axis of the cylinder combined with a Fourier series in the ϕ direction. Thus, the incident spherical SH-wave displacement expressed in a cylindrical mode expansion is given by

$$\bar{u}_n^{(i)} = C(\omega) H_n(r_s k_r) J_n(k_r r) , \text{ for } n = 0, \pm 1, \pm 2, \dots, \pm \infty . \quad (48)$$

where $C(\omega) = jF(\omega)/4\pi\rho c_s^2$.

Since the scattered spherical SH-wave displacement is a solution of the Helmholtz equation, this displacement may be expressed in terms of cylindrical wave functions referred to the cylindrical cavity axis as

$$\bar{u}_n^{(s)} = B_n H_n^{(1)}(k_r r) , \text{ for } n = 0, \pm 1, \dots, \pm \infty , \quad (49)$$

to represent outward-traveling waves. Since the total SH-wave displacement is considered as the sum of the incident and scattered waves, then

$$\bar{u}_n^t = C(\omega) H_n(r_s k_r) J_n(k_r r) + B_n H_n^{(1)}(k_r r) . \quad (50)$$

At the surface of the cylindrical cavity, $r = a$, the stress-free boundary condition

$$\sigma_{rz} = \mu \frac{\partial \bar{u}_n^t}{\partial r} = 0$$

leads to

$$B_n = -C(\omega) H_n(r_s k_r) \frac{J_n'(a k_r)}{H_n'(a k_r)} ; \quad \text{for } n = 0, \pm 1, \dots, \pm \infty . \quad (51)$$

Thus, substituting the scattered-wave coefficients given by Equation (49) into Equation (46) and applying the integral-summation operator defined by Equation (47), the steady-state solution for the total SH-wave displacement at the measurement point, P, is

$$\begin{aligned} \bar{u}_t(\omega) = & \frac{jF(\omega)}{4\pi\rho c_s^2} \int_0^\infty \sum_{n=-\infty}^\infty e^{jn(\phi-\phi_s)} \{ H_n(r_s k_r) J_n(k_r r) \\ & + G_n(r, \omega, k_r) H_n(k_r r) \} \cos \beta(z-z_s) d\beta . \end{aligned} \quad (52)$$

where:

$$G_n(r, \omega, k_r) = - \frac{J_n'(k_r a)}{H_n'(k_r a)} H_n(k_r r_s) , \quad (53)$$

and the corresponding transient solution becomes

$$u_t(t, r) = u(i) + \frac{1}{8\pi^2 \rho c_s^2} \int_0^\infty [e^{-j\omega t} F(\omega) \int_{-\infty}^\infty D(\omega, \beta) \cos \beta(z-z_s) d\beta] d\omega, \quad (54)$$

where:

$$D(\omega, \beta) = \sum_{n=-\infty}^{\infty} G_n(r, \omega, k_r) H_n(k_r r) e^{nj(\phi - \phi_s)}.$$

5. Scattering of Cylindrical SH Waves by a Cylindrical Cavity

To solve the steady-state solution for an SH-wave line source, the point source representation given in Equation (40) may be integrated along the z-axis. That is,

$$\bar{u}_l^{(i)} \equiv \frac{F(\omega)}{4\pi c_s^2} \int_{-\infty}^{\infty} \frac{e^{jkR}}{R} dz.$$

Next, using the integral solution

$$\int_{-\infty}^{\infty} \frac{e^{jkR}}{R} dz = \pi j H_0^{(1)}(k|r-r_s|),$$

the incident cylindrical SH-wave displacement becomes

$$\bar{u}_l^{(i)} \equiv \frac{jF(\omega)}{4\rho c_s^2} H_0^{(1)}(k|r-r_s|),$$

which may be expressed in terms of cylindrical functions as

$$\bar{u}_l^{(i)} \equiv \frac{jF(\omega)}{4\rho c_s^2} \sum_{n=-\infty}^{\infty} H_n^{(1)}(r_s k) J_n(r k) e^{jn(\phi - \phi_s)}.$$

As in the SH-wave point source solution previously developed, the scattered cylindrical SH-wave displacement can be expressed in terms of cylindrical-wave functions as

$$\bar{u}_l^s = \sum_{n=-\infty}^{\infty} C_n H_n^{(1)}(rk) e^{jn(\phi - \phi_s)},$$

to represent outward-traveling waves. Thus, the total SH-wave displacement at position, P, is

$$\begin{aligned} \bar{u}_l^t = & \frac{jF(\omega)}{4\rho c_s^2} \sum_{n=-\infty}^{\infty} H_n^{(1)}(r_s k) J_n(rk) e^{jn(\phi - \phi_s)} \\ & + \sum_{n=-\infty}^{\infty} C_n H_n^{(1)}(rk) e^{jn(\phi - \phi_s)}. \end{aligned} \quad (55)$$

Applying the stress-free boundary condition at the surface of the cylindrical cavity leads to the solution of the scattering coefficients for a line source of SH waves

$$C_n = -j \frac{F(\omega)}{4\rho c_s^2} H_n^{(1)}(r_s k) \frac{J_n'(ak)}{H_n'(ak)}.$$

Thus, the steady-state solution for cylindrical SH waves scattered from a cylindrical cavity in an unbounded elastic medium is

$$\bar{u}_l^t = \frac{jF(\omega)}{4\rho c_s^2} \left\{ \sum_{n=-\infty}^{\infty} e^{jn(\phi - \phi_s)} [H_n(r_s k) J_n(rk) + Q_n H_n(rk)] \right\}, \quad (56)$$

where:

$$Q_n = - \frac{J_n'(ka)}{H_n'(ka)} H_n(kr_s),$$

and the corresponding transient solution is

$$u_t(t, r) = \frac{j}{4\pi\rho c_s^2} \int_{-\infty}^{\infty} e^{-j\omega t} F(\omega) N(\omega) d\omega,$$

where:

$$N(\omega) = \sum_{n=-\infty}^{\infty} H_n(kr_s) [J_n(rk) + Q_n H_n(rk)] e^{jn(\phi - \phi_s)} .$$

6. Attenuation and Dispersion Along the Ray Path

The steady-state solution reported for elastic-wave scattering from an infinitely long cylindrical cavity in an unbounded homogeneous solid medium may be extended to include attenuation and dispersion. The total SH-wave displacement expressed in terms of a complex propagation constant, k_s , is given by

$$u^t(\omega) = \frac{F(\omega)}{4\pi\rho c^2} \left\{ j\pi H_0(k_s |r-r_s|) - j\pi \sum_{n=-\infty}^{\infty} \frac{J_n'(k_s a)}{H_n'(k_s a)} \right. \\ \left. \times H_n(r_s k_s) H_n(r k_s) e^{jn(\phi - \phi_s)} \right\} \quad (57)$$

where:

$$k_s = \frac{\omega}{c(\omega)} + j\alpha(\omega) ;$$

$\alpha(\omega)$ = the absorption coefficient; and
 $c(\omega)$ = the phase velocity.

To calculate synthetic seismograms, the attenuation and dispersion model developed by Futterman (1962) was implemented in the general steady-state solution of the total SH-wave displacement stated in Equation (57). The corresponding time derivative for the total SH-wave displacement was obtained by the Fourier transform method. Futterman states that if the medium behaves in a linear manner, then, as a consequence of the principle of causality, the presence of attenuation also requires the presence of dispersion; that is, if the imaginary part, $\alpha(\omega)$, of the complex propagation constant, k_s , is known, then the real part, $\omega/c(\omega)$, can be determined. In particular, if

$$\alpha(\omega) = \frac{\omega}{2Q_0 c_0} [1 - e^{-\omega/\omega_0}] \quad (58a)$$

then,

$$c(\omega) = c_0 \left[1 - \frac{1}{\pi Q_0} \log \left(\frac{\omega}{\omega_0} \right) \right]^{-1} \quad (58b)$$

where:

c_0 = the phase velocity at ω_0 ; and
 Q_0 = value of the quality factor, Q , at ω_0 .

The Futterman model has wide applicability and covers a broad frequency range. It is limited at low frequencies by a finite arbitrarily small but nonzero cut-off frequency, ω_0 , below which there is assumed to be no attenuation. That is,

$$k_s = \begin{cases} \omega/c_0 & ; \text{ for } \omega < \omega_0 \\ \frac{\omega}{c(\omega)} + j\alpha(\omega) & ; \text{ for } \omega > \omega_0 \end{cases} \quad (59a)$$

(59b)

Substituting Equations (58a) and (58b) into Equations (59a) and (59b), respectively, the parameter, ak_s , for the Futterman model is

$$ak_s = \begin{cases} ka & ; \text{ for } ka < k_0a \\ ka \left[1 - \frac{1}{\pi Q_0} \log \left(\frac{ka}{k_0a} \right) \right] + \frac{jka}{2Q_0} \left[1 - e^{-\frac{ka}{k_0a}} \right] & ; \text{ for } ka > k_0a \end{cases} \quad (60)$$

The numerical solution of Equation (60) is computed by the complex function zk program presented in Appendix H.

Figure II-3 shows the geometry used in analyzing SH-wave scattering from a cylindrical cavity in an unbounded lossy medium for incident cylindrical SH waves. The total SH-wave displacement at measurement point, $P(x,y)$, consists of the sum of the incident wave and the wave scattered from the cylindrical cavity. The total SH-wave displacement is expressed by Equation (57) presented earlier, and its corresponding time derivative is

$$u'(t) = \frac{1}{2\pi} \int_{-\infty}^{\infty} F(\omega) T(\omega) \omega e^{-j\omega t} d\omega, \quad (61)$$

where:

$$T(\omega) = \frac{1}{4\pi\rho c^2} \left\{ j\pi H_0(k_s |r-r_s|) - j\pi \sum_{n=-\infty}^{\infty} \frac{J_n'(k_s a)}{H_n'(k_s a)} \right. \\ \left. \times H_n(k_s r_s) H_n(k_s r) e^{jn(\phi - \phi_s)} \right\};$$

$$k_s = \frac{\omega}{c(\omega)} + j\alpha(\omega); \text{ and}$$

$F(\omega)$ = a body force acting parallel to the z-axis at the position (x_s, y_s) .

The body force, $F(\omega)$, is obtained from the frequency transform

$$F(\omega) = \int_0^{\infty} f(t) e^{j\omega t} dt \quad (62)$$

in which $f(t)$ is the applied SH-wave pulse signal defined, for the present analysis, by

$$f(t) = \beta t e^{-\beta t} \sin \omega_0 t U(t) , \quad (63)$$

where $U(t)$ is the unit step function. The frequency spectrum of $f(t)$ is given by

$$F(\omega) = \frac{2\beta\omega_0(\beta - j\omega)}{[(\beta - j\omega)^2 + \omega_0^2]^2} \quad (64)$$

where:

$\beta = 0.9 \omega_0/\pi$; and

ω_0 = the peak frequency in the pulse spectrum.

Equation (63) was used to compute the real function pulse (t) program presented in Appendix H.

E. SH-Wave Scattering from a Cylindrical Cavity in a Homogeneous Half-Space

1. Scattering of Spherical SH Waves by a Cylindrical Cavity

Figure II-4 illustrates a semi-infinite homogeneous isotropic elastic half-space having a shear modulus, μ , and a density, ρ . A cylindrical cavity of radius, a , is located in the lossless half-space at a depth, h , from the free surface. An SH-wave point force in the elastic medium acts along the z-axis (shear polarization parallel to the cylinder) and represents a body force, $f(t - R/c_s)$, at the position $S(-x_s, y_s, z_s)$. The axis of the cylindrical cavity contains the origin of the x, y, z cartesian coordinate system.

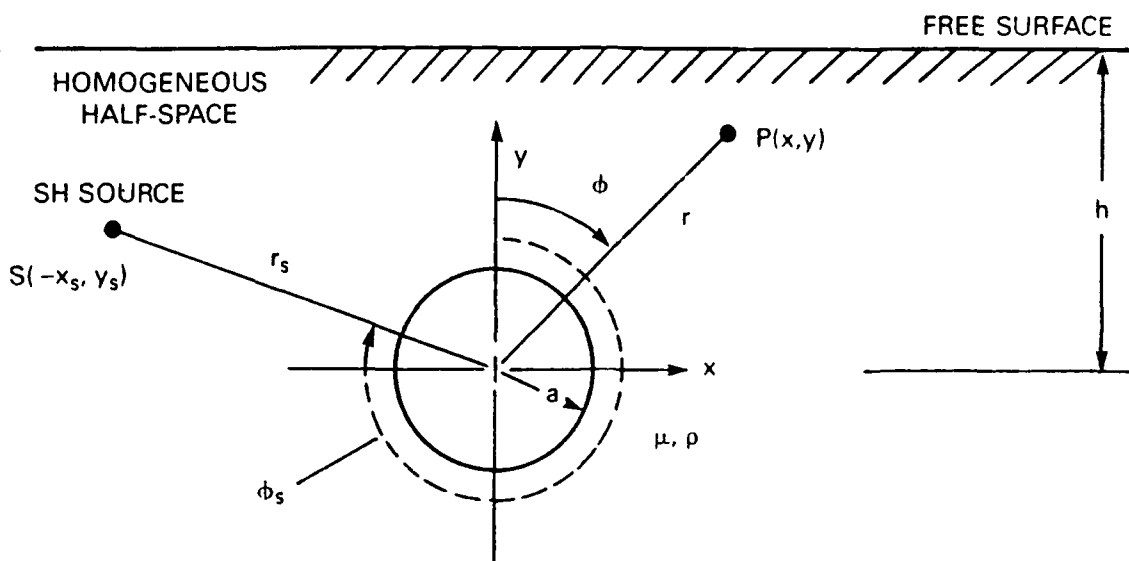


FIGURE II-4. CROSS-SECTION OF A CYLINDRICAL CAVITY IN A HOMOGENEOUS HALF-SPACE

The displacement field of the SH-wave point force satisfies the inhomogeneous wave equation and, in the frequency domain, is represented in terms of cylindrical functions. For the region $y < h$:

$$\bar{u}(i) = \frac{jF(\omega)}{4\pi\rho c_s^2} \int_0^\infty \sum_{n=-\infty}^{\infty} H_n^{(1)}(r_s k_r) J_n(r k_r) \times e^{jn(\phi - \phi_s)} \cos \beta(z - z_0) d\beta \quad (65)$$

where:

$$r_s = (x_s^2 + y_s^2)^{1/2};$$

$$r = (x^2 + y^2)^{1/2};$$

$$\phi = \tan^{-1}(x/y);$$

$$\phi_s = \tan^{-1}(-x_s/y_s); \text{ and}$$

$$k_r = (k^2 - \beta^2)^{1/2}.$$

The analysis of scattering of spherical SH waves by a cylindrical cavity in a homogeneous half-space may be deduced in terms of the

corresponding whole-space solution by using image theory. In fact, one of the boundary conditions for this half-space problem states that the traction is zero at the surface interface. This effect may be achieved in a whole space by matching each source in the lower half-space plane ($y < h$) with a source of equal magnitude and opposite polarity placed at the source image position in the upper half-space ($y > h$). The SH-wave displacement distribution in each half of this composite whole-space arrangement will then be the same as the sought-after displacement distribution in the half-space problem.

From a physical point of view, the spherical SH waves produced by the point source in the lossless half-space medium are reflected from the plane-surface ($y = h$), and scattered and diffracted by the surface of the cylindrical cavity, $r = a$. Therefore, the resultant total SH-wave displacement, \bar{u}^t , is a superposition of the incident, reflected, scattered, and diffracted waves and must satisfy the traction-free boundary conditions:

At the surface of the earth ($y = h$):

$$\sigma_{yz} = \mu \frac{\partial \bar{u}^t}{\partial y} = 0 .$$

At the surface of the cavity ($r = a$):

$$\sigma_{rz} = \mu \frac{\partial \bar{u}^t}{\partial r} = 0 . \quad (66)$$

To obtain the solution for the scattered SH waves by the cylindrical cavity, two cylindrical cavities are considered to exist in the image-based whole-space geometry shown in Figure 11-5. The cavity of radius, a , in the lower half-space ($y < h$) with axis at $(0,0)$ occupies the space $r < a$ and $-\infty < z < \infty$ in the cylindrical coordinate system (r, ϕ, z) . The cylindrical cavity of radius, a , in the upper half-space ($y > h$) with axis at $(0, 2h)$ occupies the space $r_h < a$ and $-\infty < z_h < \infty$ in the cylindrical coordinate system (r_h, ϕ_h, z_h) .

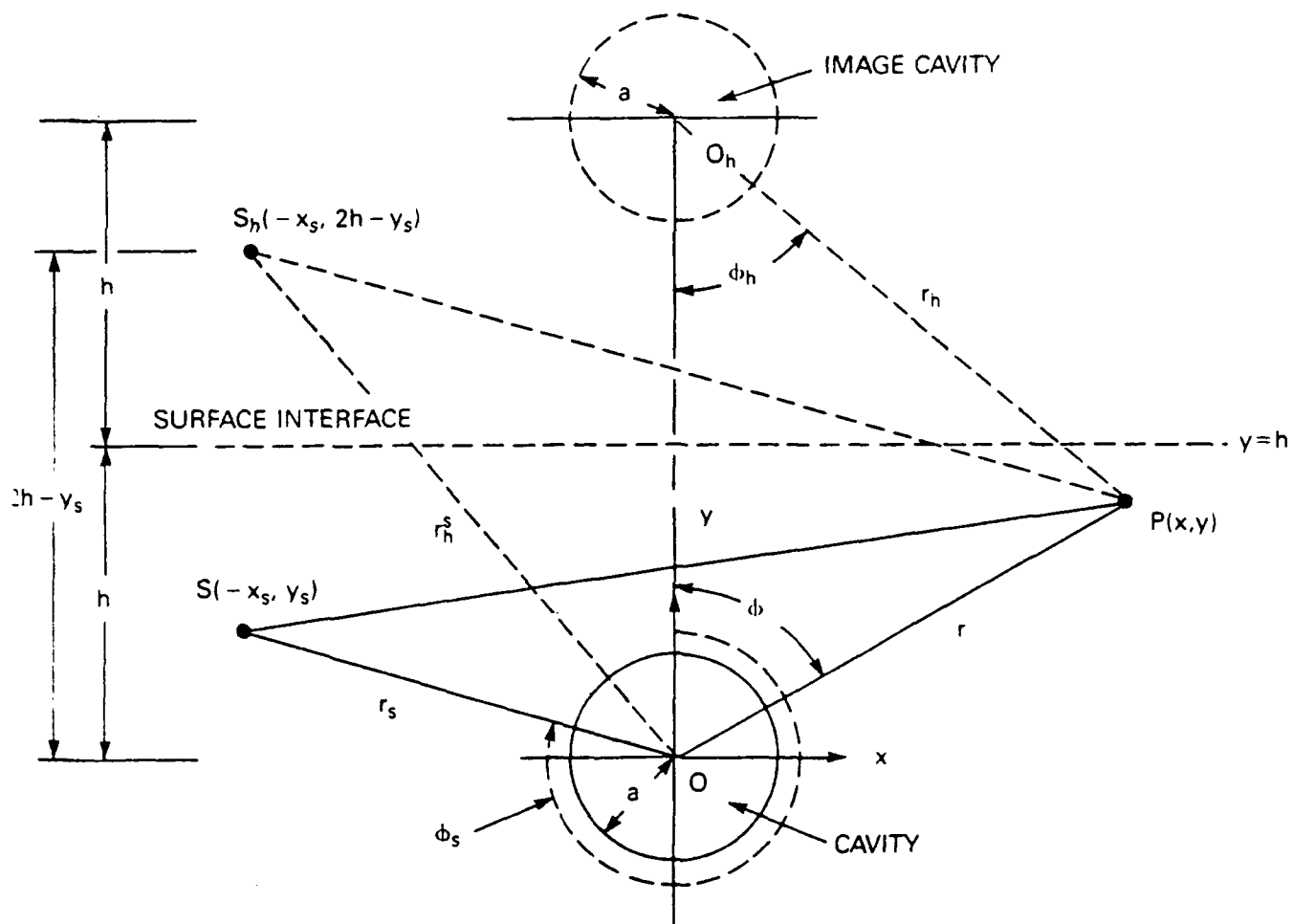


FIGURE II-5. WHOLE-SPACE CONTAINING REAL AND IMAGE CAVITIES AND REAL AND IMAGE SOURCES SYMMETRICALLY PLACED WITH RESPECT TO THE $y = h$ PLANE

To satisfy the boundary conditions at the free surface, the image of the incident SH-wave displacement is expressed as

$$\bar{u}_h^{(1)} = \frac{jF(\omega)}{4\pi\rho c_s^2} \int_0^\infty \sum_{n=-\infty}^\infty H_n^{(1)}(r_h^s k_r) J_n(r k_r) e^{jn(\phi - \phi_h^s)} \cos \beta(z - z_0) d\beta, \quad (67)$$

where:

$$r_h^s = [(2h - y_s)^2 + x_s^2]^{1/2};$$

$$\phi_h^s = \tan^{-1} \left[\frac{-x_s}{2h - y_s} \right].$$

To represent outward-traveling waves, the scattered SH-wave displacements $\bar{u}_h(s)$ and $u(s)$ must be of the form

$$\bar{u}(s) = \int_0^\infty \sum_{n=-\infty}^{\infty} A_n H_n^{(1)}(rk_r) e^{jn\phi} \cos \beta(z-z_0) d\beta \quad (68)$$

and

$$\bar{u}_h(s) = \int_0^\infty \sum_{n=-\infty}^{\infty} A_n H_n^{(1)}(r_h k_r) e^{jn\phi} \cos \beta(z-z_0) d\beta \quad (69)$$

in which

$$r_h = [4h^2 + r^2 - 4rh \cos \phi]^{1/2}.$$

In the whole space, the derivatives with respect to y of the $\bar{u}(i) + \bar{u}_h(i)$ and $\bar{u}(s) + \bar{u}_h(s)$ must vanish at $y = h$ because of the symmetry of their representation. Thus, in the half-space, $y < h$, the sum of the incident SH-wave displacements, $u(i) + u_h(i)$, and the scattered SH-wave displacements, $\bar{u}(s) + \bar{u}_h(s)$, satisfies the traction-free condition at $y = h$. The resulting total SH-wave displacement in the elastic half-space, \bar{u}^t , is

$$\bar{u}^t = \bar{u}(i) + \bar{u}_h(i) + \bar{u}(s) + \bar{u}_h(s) \quad (70)$$

and must satisfy the traction-free condition at the surface of the cavity, $r = a$.

Using the addition theorem for the Hankel function

$$H_n^{(1)}(r_h k_r) e^{jn\phi} = \sum_{m=-\infty}^{\infty} J_m(k_r r) H_{n+m}^{(1)}(2k_r h) e^{jm\phi}, \quad (71)$$

the total SH-wave displacement in the wave number domain may be written as

$$\begin{aligned} \bar{u}_\beta^t = & \frac{jF(\omega)}{4\pi\rho c_s^2} \sum_{n=-\infty}^{\infty} \{ H_n(r_s k_r) e^{-jn\phi_s} + H_n(r_h^s k_r) e^{-jn\phi_h^s} \} J_n(rk_r) e^{jn\phi} \\ & + \sum_{n=-\infty}^{\infty} A_n H_n(rk_r) e^{jn\phi} + \sum_{n=-\infty}^{\infty} \sum_{m=-\infty}^{\infty} A_n J_m(k_r r) H_{n+m}(2k_r h) e^{jm\phi}. \end{aligned} \quad (72)$$

The use of the traction-free boundary condition

$$\left[\frac{\partial \bar{u}_P^t}{\partial r} \right]_{r=a} = 0 \quad (73)$$

leads to an infinite set of algebraic linear equations for the determination of the unknown wave coefficients, A_n . Upon normalizing Equation (72) by the factor $\frac{jF(\omega)}{4\pi\rho c_s^2}$, this linear system of equations is given by

$$\sum_{m=-\infty}^{\infty} a_m \left\{ \delta_{nm} + \frac{J'_n(k_r a)}{H'_n(k_r a)} H_{n+m}(2k_r h) \right\} = \frac{J'_n(k_r a)}{H'_n(k_r a)} \{ H_n(k_r r_h^s) e^{-jn\phi_h^s} + H_n(k_r r_s) e^{-jn\phi_s} \};$$

for $n = 0, \pm 1, \pm 2, \dots \pm \infty$, (74)

where:

$$a_m = \frac{A_m}{\frac{jF(\omega)}{4\pi\rho c_s^2}};$$

and

$$\delta_{nm} = \begin{cases} 1; & \text{for } n = m \\ 0; & \text{for } n \neq m. \end{cases}$$

Finally, the steady-state solution for the total spherical SH-wave displacement at the measurement point, P, expressed in terms of the scattered-wave coefficients, a_m , is given by

$$\begin{aligned} \bar{u}^t(\omega) = & \frac{F(\omega)}{4\pi\rho c_s^2} \left\{ \frac{e^{jkR^s}}{R^s} + \frac{e^{jkR_h^s}}{R_h^s} \right\} \\ & - \frac{F(\omega)}{4\pi\rho c_s^2} \left(\frac{1}{2\pi} \right) \int_{-\infty}^{\infty} \sum_{m=-\infty}^{\infty} a_m \pi j [H_m(r k_r) e^{jm\phi} + H_m(r_h k_r) e^{jm\phi_h}] \\ & \times \cos \beta(z-z_0) d\beta, \end{aligned} \quad (75)$$

where:

$$R_s = [(x-x_s)^2 + (y-y_s)^2 + (z-z_s)^2]^{1/2};$$

$$R_h^s = [(x-x_s)^2 + (y+y_s-2h)^2 + (z-z_s)^2]^{1/2};$$

$$r = (x^2+y^2)^{1/2};$$

$$r_h = (4h^2+r^2-4rh \cos \phi)^{1/2};$$

$$\phi_h = \sin^{-1} \left(\frac{r}{r_h} \sin \phi \right); \text{ and}$$

$$\phi = \tan^{-1} (x/y).$$

The corresponding transient shear-wave displacement, $u^t(r,t)$, may be represented as the sum of the incident field displacement, $u^{(i)}(r,t)$, and the scattered field displacement as follows

$$u^t(r,t) = u^{(i)}(r,t) + u^{(s)}(r,t) .$$

The incident field is given by

$$u^{(i)} = \frac{1}{4\pi\rho c_s^2} \left\{ \frac{f(t-R_s/c_s)}{R_s} + \frac{f(t-R_h^s/c_s)}{R_h^s} \right\} . \quad (76)$$

The scattered field can be expressed in the form of a two-dimensional Fourier transform over frequency and axial wave number as

$$u^t(r,t) = \frac{1}{(2\pi)^2} \int_{-\infty}^{\infty} \int_{-\infty}^{\infty} [F(\omega)T(\omega,\beta)] e^{j\beta(z-z_0)} e^{-j\omega t} d\beta d\omega \quad (77)$$

where $F(\omega)$ is the Fourier transform of $f(t)$ and $T(\omega,\beta)$ is given by

$$T(\omega,\beta) = - \frac{1}{4\pi\rho c_s^2} \sum_{m=-\infty}^{\infty} a_m \pi j [H_m(rk_r) e^{jm\phi} + H_m(r_h k_r) e^{jm\phi_h}] . \quad (78)$$

The integral representation for the scattered field in Equation (77) may be evaluated numerically and the result added to the incident field given by Equation (76) to obtain the total field. A numerical method of integration used by Tsang and Rader (1979) may be implemented to evaluate the integral in Equation (77). This integration method is referred to as real-axis integration because a Laplace contour is used in the frequency integration, while a path along the real axis is used in the wave number integration. Using this method, singularities in $T(\omega, \beta)$ are located away from the integration path and aliasing problems are reduced.

In this method, the integral over frequency is performed first for each complex-valued frequency. The β integration is given by

$$b(\omega, z) = \frac{1}{2\pi} \int_{-\infty}^{\infty} T(\omega, \beta) e^{j\beta z} d\beta .$$

The result is then Laplace transformed over frequency by evaluating the integral,

$$u(s)(r, t) = \frac{1}{2\pi} \int_{-\infty + j\omega_I}^{\infty + j\omega_I} F(\omega) b(\omega, z) e^{-j\omega t} d\omega ,$$

where $\omega_I > 0$.

2. Scattering of Cylindrical SH Waves by a Cylindrical Cavity

The steady-state solution for elastic-wave scattering from an infinitely long cylindrical cavity in a homogeneous lossless half-space for incident cylindrical SH waves proceeds in a manner similar to that derived for incident spherical SH waves.

The incident cylindrical SH-wave displacement is expressed in terms of cylindrical functions as

$$\bar{u}(i) = \frac{jF(\omega)}{4\rho c_s^2} \sum_{n=-\infty}^{\infty} H_n(r_s k) J_n(kr) e^{jn(\phi - \phi_s)} \quad (79)$$

and its associated image incident displacement function is

$$\bar{u}_h(i) = \frac{jF(\omega)}{4\rho c_s^2} \sum_{n=-\infty}^{\infty} H_n(r_h^s k) J_n(kr) e^{jn(\phi - \phi_h^s)} , \quad (80)$$

where the radial distances r_s and r_h^s and the angles ϕ and ϕ_h^s have been defined in Figure II-5. Alternatively, the scattered cylindrical SH-wave displacements $\bar{u}(s)$ and $\bar{u}_h(s)$ are represented, respectively, by

$$\bar{u}(s) = \sum_{n=-\infty}^{\infty} A_n H_n(rk) e^{jn\phi}$$

and

(81)

$$\bar{u}_h(s) = \sum_{n=-\infty}^{\infty} A_n H_n(r_h k) e^{jn\phi_h}$$

in which $r_h = (4h^2 + r^2 - 4rh \cos \phi)^{1/2}$.

Using the addition theorem given in Equation (71), the resulting total SH-wave displacement may be written as

$$\begin{aligned} \bar{u}^t = & \frac{F(\omega)}{4\pi\rho c_s^2} \sum_{n=-\infty}^{\infty} \pi j [H_n(r_s k) e^{-jn\phi_s} + H_n(r_h^s k) e^{-jn\phi_h^s} J_n(kr) e^{jn\phi}] \\ & + \sum_{n=-\infty}^{\infty} A_n H_n(rk) e^{jn\phi} + \sum_{n=-\infty}^{\infty} \sum_{m=-\infty}^{\infty} A_n J_m(kr) H_{n+m}(2kh) e^{jm\phi} . \end{aligned} \quad (82)$$

After applying the traction-free boundary condition at the surface of the air-filled cavity, the following infinite set of linear equations is obtained:

$$\sum_{m=-\infty}^{\infty} a_m \left[\delta_{nm} + \frac{J'_n(ka)}{H'_n(ka)} H_{n+m}(2kh) \right] = \frac{J'_n(ka)}{H'_n(ka)} [H_n(kr_h^s) e^{-jn\phi_h^s} + H_n(kr_s) e^{-jn\phi_s}];$$

$$\text{for } n = 0, \pm 1, \pm 2, \dots, \pm \infty, \quad (83)$$

where:

$$a_m = \frac{A_m}{-\frac{F(\omega)}{4\pi\rho c_s^2} (\pi j)} ; \quad \text{for } k \neq 0$$

$$a_m = 0 ; \quad \text{for } k = 0$$

and

$$\delta_{nm} = \begin{cases} 1; & \text{for } n = m \\ 0; & \text{for } n \neq m. \end{cases}$$

Finally, the steady-state solution for the total cylindrical SH-wave displacement at the measurement point, P, expressed in terms of the scattered-wave coefficients, a_m , is given by

$$\begin{aligned} \bar{u}(t)(\omega) = & \frac{F(\omega)}{4\pi\rho c_s^2} [\pi j H_0(kr_1) + \pi j H_0(kr_2)] \\ & - \frac{F(\omega)}{4\pi\rho c_s^2} \sum_{m=-\infty}^{\infty} a_m \pi j [H_m(kr)e^{jm\phi} + H_m(kr_h)e^{jm\phi_h}] \end{aligned} \quad (84)$$

where:

$$r_1 = [(x-x_s)^2 + (y-y_s)^2]^{1/2};$$

$$r_2 = [(x-x_s)^2 + (y+y_s-2h)^2]^{1/2};$$

$$r = (x^2+y^2)^{1/2};$$

$$r_h = (4h^2 + r^2 - 4rh \cos \phi)^{1/2};$$

$$\phi_h = \sin^{-1} \left(\frac{r}{r_h} \sin \phi \right); \text{ and}$$

$$\phi = \tan^{-1} (x/y).$$

The corresponding transient shear-wave displacement becomes

$$u(t)(r,t) = u^{(1)}(r_1,t) + u^{(1)}(r_2,t) + u^{(s)}(r,t). \quad (85)$$

The scattered field displacement, $u^{(s)}(r, t)$, can be expressed in the form of a one-dimensional Fourier transform over frequency as

$$u^{(s)}(r, t) = \frac{1}{2\pi} \int_{-\infty}^{\infty} e^{-j\omega t} F(\omega) \bar{T}_\lambda(\omega) d\omega = f(t) * T_\lambda(t) \quad (86)$$

where:

$$\bar{T}_\lambda(\omega) = -\frac{1}{4\pi\rho c_s^2} \sum_{m=-\infty}^{\infty} a_m \pi j [H_m(rk) e^{jm\phi} + H_m(kr_h) e^{jm\phi h}] \quad (87)$$

and

$$T_\lambda(t) = \frac{1}{2\pi} \int_{-\infty}^{\infty} \bar{T}_\lambda(\omega) e^{-j\omega t} d\omega. \quad (88)$$

The incident field displacements, $u^{(1)}(r_1, t)$ and $u^{(1)}(r_2, t)$, can be deduced by applying the Cagniard-deHoop method (deHoop, 1960) for solving seismic pulse problems. Each of the incident SH-wave displacements given in Equation (85) can be obtained from the function represented by

$$u^{(1)}(r, t) = \int_0^t f(t-\tau) g(r, \tau) d\tau, \quad (89)$$

where:

$$g(r, \tau) = \begin{cases} 0; & \text{for } (0 < \tau < \frac{r}{c_s}) \\ \frac{1}{2\pi\rho c_s^2} (\tau^2 - \frac{r^2}{c_s^2})^{-1/2}; & \text{for } (\frac{r}{c_s} < \tau < \infty) \end{cases} \quad (90)$$

is regarded as the wave function corresponding to the delta function time dependence of the SH-line source.

F. SH-Wave Scattering from a Cylindrical Cavity in a Two-Layer Half-Space

The steady-state and transient solutions for elastic-wave scattering from an infinitely long cylindrical cavity in a two-layer homogeneous lossless solid medium is developed for incident cylindrical SH waves. The cylindrical SH waves are generated by a line source within the two-layer half-space medium. Formal analytic expressions are developed for the particle displacement of scattered waves at any detector position in the host medium for an SH-wave line source oriented parallel to the axis of the cavity. Analytical expressions are derived for SH-wave displacements to investigate the effect of the surface layer on the detection of SH waves scattered by the cylindrical cavity. In addition, to compute particle velocity seismograms, an expression for the time derivative of the total SH-wave displacement is presented and the corresponding transfer function is included as part of the computed sythetic seismograms.

1. Formulation

The derived theoretical solution is in the form of an integral equation, the unknown being the total SH-wave displacement on the surface of the cylindrical cavity. The integral equation requires the two-layer half-space Green's function and the incident SH-wave displacement for a line source to be evaluated at the surface of the scattering target. Then, the integral equation is reduced to a matrix equation, which can be solved numerically by a direct method. Thus, the SH-wave displacements outside of the cylindrical cavity are found by integrating the two-layer half-space Green's function on the surface of the cavity. Summed with the incident SH-wave displacement, the combined results represent the total SH-wave displacement at any detector position in the two-layer medium.

2. The Two-Layer Half-Space Green's Function

A stratified earth representative of a weathered surface layer and a bedrock semi-infinite half-space may be simulated by a two-layer model. This model consists of a bedrock cavity host medium of density, ρ_2 , shear modulus, μ_2 , and shear-wave velocity, c_2 , overlain by a surface layer of thickness, h , density, ρ_1 , shear modulus, μ_1 , and shear-wave velocity, c_1 , in which c_1 is less than c_2 .

An SH-wave line source is located at the position $P'(x',y')$, and the radiated SH-wave particle displacement is detected at the position $P(x,y)$. Both the line source and the measurement point are located in the bedrock layer as shown in Figure II-6.

The steady-state Green's function for SH-wave particle motions satisfies the wave equations

$$(\nabla^2 + k_1^2)G_1(x,y;x',y') = 0 ; \quad \text{for } 0 \leq x \leq h ,$$

and

$$(\nabla^2 + k_2^2)G_2(x,y;x',y') = -\delta(x-x')\delta(y-y') ; \quad \text{for } x > h , \quad (91)$$

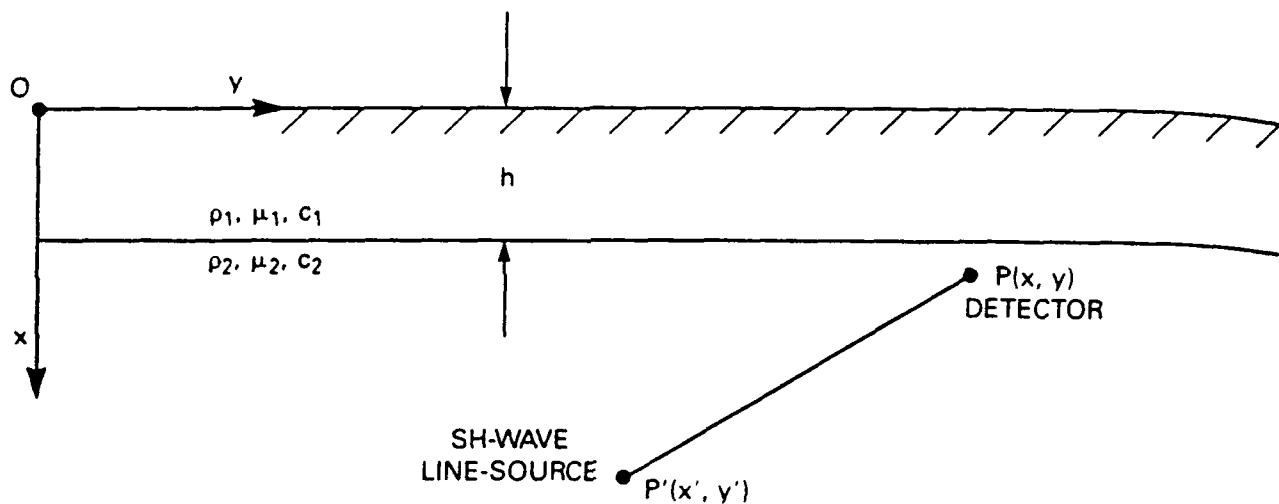


FIGURE II-6. TWO-LAYER HALF-SPACE HAVING AN SH-WAVE LINE SOURCE AND A DETECTOR LOCATED IN THE BEDROCK

where:

$$\nabla^2 = \left(\frac{\partial^2}{\partial x^2} + \frac{\partial^2}{\partial y^2} \right) ; \text{ and } k_1 = \frac{\omega}{c_1} ; k_2 = \frac{\omega}{c_2} \text{ in which } c_1 < c_2 .$$

The Green's functions for cylindrical SH-wave motions may be developed using the spectral representation of the free-space Green's function developed in Appendix A. Thus, the Green's functions for the regions of different elastic properties are:

For the region $0 < x < h$:

$$G_1 = \frac{1}{4\pi} \int_{-\infty}^{\infty} [f_1(\lambda) e^{-\gamma_1 x} + g_1(\lambda) e^{\gamma_1 x}] \frac{e^{j\lambda(y-y')}}{\gamma_1} d\lambda . \quad (92)$$

For the region $x > h$:

$$G_2 = \frac{1}{4\pi} \int_{-\infty}^{\infty} [e^{-\gamma_2 |x-x'|} + f_2(\lambda) e^{-\gamma_2 x}] \frac{e^{j\lambda(y-y')}}{\gamma_2} d\lambda , \quad (93)$$

where:

$$\gamma_1 = (\lambda^2 - k_1^2)^{1/2} ;$$

and

$$\gamma_2 = (\lambda^2 - k_2^2)^{1/2} .$$

The determination of the square roots is such that $\text{Real}\{\gamma_1, \gamma_2\} > 0$ over the entire path of integration, $-\infty < \lambda < \infty$. The factors $f_1(\lambda)$, $g_1(\lambda)$, and $f_2(\lambda)$ are arbitrary functions of λ which render the integrals convergent and satisfy the following boundary conditions:

At the surface of the earth:

$$\left[\mu_1 \frac{\partial G_1}{\partial x} \right]_{x=0} = 0 . \quad (94)$$

At the layer interface (continuity of stress and displacement are required):

$$\left[\mu_1 \frac{\partial G_1}{\partial x} \right]_{x=h} = \left[\mu_2 \frac{\partial G_2}{\partial x} \right]_{x=h}$$

and

$$[G_1]_{x=h} = [G_2]_{x=h} . \quad (95)$$

These relationships lead to three linear algebraic equations to be solved for the unknown coefficients $f_1(\lambda)$, $g_1(\lambda)$, and $f_2(\lambda)$. Solutions of the Green's functions for the surface layer and the bottom semi-infinite region are:

For the region $0 \leq x \leq h$:

$$G_1(x, y; x', y') = \frac{1}{4\pi} \int_{-\infty}^{\infty} \epsilon_1(\lambda) \frac{e^{-\gamma_2(x'-h)}}{\gamma_2} \{ e^{-\gamma_1(x+h)} + e^{-\gamma_1(h-x)} \} \\ \times e^{j\lambda(y-y')} d\lambda . \quad (96)$$

For the region $x > h$:

$$G_2(x, y; x', y') = \frac{1}{4\pi} \int_{-\infty}^{\infty} \{ e^{-\gamma_2|x-x'|} + \epsilon_2(\lambda) e^{-\gamma_2(x+x'-2h)} \} \\ \times \frac{e^{j\lambda(y-y')}}{\gamma_2} d\lambda , \quad (97)$$

where:

$$\epsilon_1(\lambda) = \frac{T(\lambda)}{1 - R(\lambda)e^{-2\gamma_1 h}} ; \quad (98)$$

and

$$\epsilon_2(\lambda) = \frac{-R(\lambda) + e^{-2\gamma_1 h}}{1 - R(\lambda)e^{-2\gamma_1 h}} ; \quad (99)$$

in which

$$T(\lambda) = \frac{2\mu_2\gamma_2}{\mu_1\gamma_1 + \mu_2\gamma_2} \quad (100)$$

and

$$R(\lambda) = \frac{\mu_1\gamma_1 - \mu_2\gamma_2}{\mu_1\gamma_1 + \mu_2\gamma_2} . \quad (101)$$

To represent cylindrical SH-wave particle motion in terms of outgoing waves at infinity, the Green's functions given in Equations (96) and (97) are expressed in polar coordinates (r, ϕ) . For convenience, γ_1 and γ_2 are replaced in Equation (97) by $-j\alpha_1$ and $-j\alpha_2$, respectively. Thus, the bedrock Green's function, G_2 , may be rewritten as

$$G_2(x, y; x', y') = \frac{j}{4\pi} \int_{-\infty}^{\infty} \{ e^{j\alpha_2(x-x')} + \epsilon_2(\lambda) e^{j\alpha_2(x+x'-2h)} \} \frac{e^{j\lambda(y-y')}}{\alpha_2} d\lambda , \quad (102)$$

where:

$$\alpha_1 = (k_1^2 - \lambda^2)^{1/2} ;$$

$$\alpha_2 = (k_2^2 - \lambda^2)^{1/2} .$$

Figure II-7 shows the appropriate geometry for developing a solution for cylindrical SH-wave motions. This solution may be expressed in terms of a cylindrical wave function having its origin at the position (H, d) . Making the substitution $\lambda = k_2 \sin \theta$ in the second term of Equation (102) leads to the Green's function in polar coordinates.

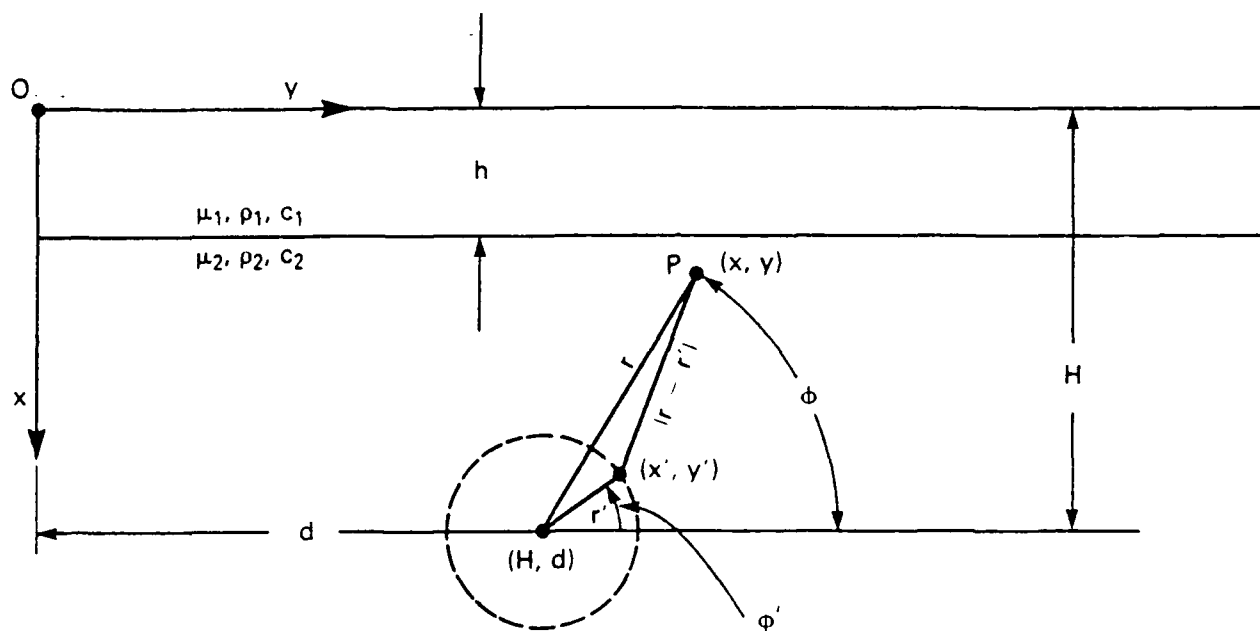


FIGURE II-7. GEOMETRY FOR THE GREEN'S FUNCTION IN POLAR COORDINATES

$$G_2(x, y; x', y') = \frac{1}{4} H_0(k_2 |r - r'|) + \frac{1}{4} \frac{1}{\pi} \int_{-\infty}^{\infty} \epsilon_2(\lambda) \frac{e^{2j\alpha_2(H-h)}}{\alpha_2} e^{-jk_2 r \cos(\phi + \theta)} \\ \times e^{-jk_2 r' \cos(\phi' - \theta)} d\lambda. \quad (103)$$

Next, substituting the identities

$$e^{-jk_2 r \cos(\phi + \theta)} = \sum_{m=-\infty}^{\infty} (-j)^m e^{j(\theta + \phi)m} J_m(rk_2)$$

and

$$e^{-jk_2 r' \cos(\phi' - \theta)} = \sum_{n=-\infty}^{\infty} (-j)^n e^{j(\theta - \phi')n} J_n(r'k_2) \quad (104)$$

and the addition theorem for the Hankel function as given by Harrington (1961)

$$H_0(k_2 |r - r'|) = \sum_{n=-\infty}^{\infty} H_n(k_2 r) J_n(k_2 r') e^{jn(\theta - \phi')} \quad (105)$$

into Equation (103) yields the cylindrical mode expansion for the Green's function in the cavity host medium. That is,

$$G_2(x, y, x', y') = \frac{1}{4\pi} \sum_{n=-\infty}^{\infty} J_n(k_2 r') e^{-jn\phi'} \{ j\pi H_n(rk_2) e^{jn\phi} + j\pi \sum_{m=-\infty}^{\infty} e^{jm\phi} J_m(rk_2) P_{nm} \} \quad (106)$$

where:

$$P_{nm} = (-j)^{n+m} \frac{1}{\pi} \int_{-\infty}^{\infty} \epsilon_2(\lambda) \frac{e^{2j\alpha_2(H-h) + j\theta(m+n)}}{\alpha_2} d\lambda \quad (107a)$$

in which

$$\theta = \tan^{-1}(\lambda/\alpha_2)$$

or where:

$$P_{nm} = (-j)^{n+m} \frac{1}{\pi} \int_{\Gamma} \epsilon_2(\theta) e^{2jk_2(H-h) + j\theta(n+m)} d\theta, \quad (107b)$$

where the integration path, Γ , is described in Appendix D.

Following the procedure used in deriving the bedrock Green's function, the surface-layer Green's function, G_1 , in terms of α_1 and α_2 may be written as

$$G_1(x, y; x', y') = \frac{1}{4\pi} \int_{-\infty}^{\infty} \epsilon_1(\lambda) \frac{e^{j\alpha_2(x'-h)}}{\alpha_2} [e^{j\alpha_1(x+h)} + e^{j\alpha_1(h-x)}] \times e^{j\lambda(y-y')} d\lambda. \quad (108)$$

Making the appropriate substitutions to convert Equation (108) to polar coordinates, the surface layer Green's function, G_1 , becomes

$$G_1(x, y; x', y') = \frac{1}{4\pi} \sum_{m=-\infty}^{\infty} j\pi J_m(r'k_2) e^{-jm\phi'} \sum_{n=-\infty}^{\infty} e^{jn\phi} J_n(rk_2) Q_{nm} \quad (109)$$

where:

$$Q_{nm} = (-j)^{n+m} \frac{1}{\pi} \int_{-\infty}^{\infty} \epsilon_1(\lambda) e^{j\alpha_2(2H-h)+j\theta(n+m)} [e^{j\alpha_1(x+h)} + e^{j\alpha_1(h-x)}] d\lambda$$

in which

$$\theta = \tan^{-1} (\lambda/\alpha_2) \quad (110a)$$

or where:

$$Q_{nm} = (-j)^{n+m} \frac{1}{\pi} \int_{\Gamma} d\theta \epsilon_1(\theta) e^{jk_2(2H-h-x) \cos \theta + j\theta(n+m)} \\ \times [e^{jk_2\alpha(\theta)(x+h)} + e^{jk_2\alpha(\theta)(h-x)}] \quad (110b)$$

in which:

$$\alpha(\theta) = (k_1^2/k_2^2 - \sin^2\theta)^{1/2}.$$

3. Incident SH-Wave Displacement for a Line Source in a Two-Layer Half-Space

The incident SH-wave displacements for a line source located at (x_s, y_s) in the semi-infinite bottom layer satisfies the wave equations

$$(\nabla^2 + k_1^2) u_1(1) = 0; \text{ for } 0 < x < h \\ (\nabla^2 + k_2^2) u_2(1) = \frac{-F(\omega)}{\rho_2 c_2^2} \delta(x-x_s) \delta(y-y_s); \text{ for } x > h, \quad (111)$$

where k_1 and k_2 are defined in Equation (91). The function $F(\omega)$ is a body force acting parallel to the z -axis at the position (x_s, y_s) . Since the wave equations given in Equations (111) and (91), respectively, have the same forms and they are subject to the same boundary conditions, the incident SH-wave displacements may be deduced directly from Equations (96) and (97).

For the region $0 < x < h$:

$$u_1(1) = \frac{jF(\omega)}{4\rho_2 c_2^2} \frac{1}{\pi} \int_{-\infty}^{\infty} \epsilon_1(\lambda) \frac{e^{+j\alpha_2(x_s-h)}}{\alpha_1} [e^{j\alpha_1(x+h)} + e^{j\alpha_1(h-x)}] \\ \times e^{i\lambda(y-y_s)} d\lambda. \quad (112)$$

45/46/47

4. Integral Equation Solution for SH-Wave Scattering from a Cylindrical Cavity in a Two-Layer Half-Space for a Detector in the Bedrock

The total SH-wave displacement, u^t , in a medium is composed of two parts: the incident wave, $u^{(i)}$, and the scattered waves, $u^{(s)}$. That is,

$$u^t = u^{(i)} + u^{(s)} \quad (118)$$

Each of these wave functions satisfies the first (interior) and second (exterior) Helmholtz equations as given in Appendix B. For a cylindrical air-filled cavity, the normal derivative of the total SH-wave displacement vanishes at the cavity surface, S (i.e., the stress-free surface boundary condition is satisfied). Under this condition, the total SH-wave displacement, u^t , at the surface, S , may be obtained from Equation (B-7) and it satisfies the integral equation

$$-\frac{\partial u^{(i)}(r)}{\partial \hat{r}} = \frac{\partial}{\partial \hat{r}} \int_S u^t(r') \frac{\partial G(r, r')}{\partial \hat{r}'} dS ; \text{ for } r \text{ on } S \quad (119)$$

Next, the Green's function given by Equation (106) and the incident-wave displacement as given by Equation (115) together with the total SH-wave displacement on the boundary $S(r' = a)$, assumed to be of the form

$$u^t = \sum_{l=-\infty}^{\infty} B_l e^{jl\phi'} , \quad (120)$$

are substituted into the integral equation given by Equation (119). With $dS = a d\phi'$, where a is the radius of the cavity, the integral equation takes the form

$$-\frac{\partial u_2^{(i)}}{\partial r} \Big|_{r=a} = \frac{1}{4\pi} \frac{\partial}{\partial \hat{r}} \int_0^{2\pi} \left(\sum_{l=-\infty}^{\infty} B_l e^{jl\phi'} \right) a d\phi' \\ \times \left\{ j\pi \sum_{n=-\infty}^{\infty} J_n'(k_2 a) e^{-jn\phi'} [H_n(rk_2) e^{jn\phi} + \sum_{m=-\infty}^{\infty} J_m(rk_2) e^{jm\phi} p_{nm}] \right\} . \quad (121)$$

Utilizing the properties

$$\frac{1}{2\pi} \int_0^{2\pi} e^{j\phi'(\ell-n)} d\phi' = \begin{cases} 0; & \text{for } \ell \neq n \\ 1; & \text{for } \ell = n, \end{cases}$$

Equation (121) (at $r = a$) is reduced to

$$-\frac{\partial u_2(i)}{\partial r} \bigg|_{r=a} = \frac{a}{2} \sum_{\lambda=-\infty}^{\infty} j\pi B_{\lambda} J_{\lambda}'(k_2 a) \{ H_{\lambda}'(ak_2) e^{j\lambda\phi} + \sum_{m=-\infty}^{\infty} J_m'(ak_2) e^{jm\phi} P_{\lambda m} \} . \quad (122)$$

Substituting the incident wave of Equation (115) into Equation (122) yields

$$\begin{aligned} & -\frac{F(\omega)}{4\pi\rho_2 c_2^2} \left\{ \pi j \sum_{n=-\infty}^{\infty} J_n'(k_2 a) e^{jn\phi} [H_n(r_s k_2) e^{-jn\phi_s} + S_n] \right\} \\ & = \frac{a}{2} \sum_{\lambda=-\infty}^{\infty} j\pi (B_{\lambda} J_{\lambda}'(k_2 a)) [H_{\lambda}'(ak_2) e^{j\lambda\phi} + \sum_{m=-\infty}^{\infty} J_m'(ak_2) e^{jm\phi} P_{\lambda m}] . \end{aligned} \quad (123)$$

After some algebraical manipulations, Equation (123) may be reduced to

$$\begin{aligned} & \sum_{m=-\infty}^{\infty} \left[\frac{a}{2} B_m J_m'(ak_2) \right] \left\{ \delta_{nm} + \frac{J_n'(ak_2)}{H_n'(ak_2)} P_{nm} \right\} \\ & = -\frac{F(\omega)}{4\pi\rho_2 c_2^2} \frac{J_n'(ak_2)}{H_n'(ak_2)} [H_n(r_s k_2) e^{-jn\phi_s} + S_n] , \end{aligned} \quad (124)$$

where:

$$S_n = \sum_{\lambda=-\infty}^{\infty} e^{-j\lambda\phi_s} J_{\lambda}(r_s k_2) P_{\lambda n} .$$

Then, making the substitution of

$$B_m = \frac{b_m}{\frac{a}{2} J_m'(ak_2)}$$

in Equation (124), the linear system of equations for the b_m unknowns may be expressed as

$$\sum_{m=-\infty}^{\infty} b_m \left[\delta_{nm} + \frac{J_n'(ak_2)}{H_n'(ak_2)} P_{nm} \right] = - \frac{F(\omega)}{4\pi\rho_2 c_2^2} \frac{J_n'(k_2 a)}{H_n'(k_2 a)} [H_n(r_s k_2) e^{-j m \phi_s} + S_n] \quad (125)$$

$$\text{for } n = 0, \pm 1, \pm 2, \dots \pm \infty.$$

After the value for the total SH-wave displacement, u^t , at the surface, $S(r=a)$, is known, the scattered waves in the field, $r > a$, may be derived from the second term of Equation (II-9) as

$$u(s) = \int_S u^t(r') \frac{\partial G_2(r, r')}{\partial \hat{r}'} dS; \text{ for } r \text{ in } V. \quad (126)$$

The integration of Equation (126) can be carried out in the same manner as before with the result

$$u(s) = \frac{a}{4\pi} \int_0^{2\pi} \left(\sum_{l=-\infty}^{\infty} B_l e^{j l \phi'} \right) \left(\sum_{n=-\infty}^{\infty} j\pi J_n'(k_2 a) e^{-j n \phi'} \right) d\phi' \\ \times [H_n(r k_2) e^{j n \phi} + \sum_{m=-\infty}^{\infty} J_m'(r k_2) e^{j m \phi} P_{nm}]$$

or

$$u(s) = j\pi \sum_{n=-\infty}^{\infty} \left[\frac{a}{2} B_n J_n'(k_2 a) \right] [H_n(r k_2) e^{j n \phi} + \sum_{m=-\infty}^{\infty} J_m(r k_2) e^{j m \phi} P_{nm}]. \quad (127)$$

In terms of the wave coefficients, b_n , Equation (33) is expressed as

$$u(s) = \sum_{n=-\infty}^{\infty} (j\pi b_n) [H_n(r k_2) e^{j n \phi} + \sum_{m=-\infty}^{\infty} J_m(r k_2) e^{j m \phi} P_{nm}]. \quad (128)$$

a. Steady-State and Transient Solutions for the SH-Wave Particle Motion

Superposition of the incident and scattered SH-wave displacements, $u_2^{(i)}$ and $u_2^{(s)}$, given by Equations (113) and (128), respectively, leads to the steady-state solution for the total SH-wave displacement for the case where the line source and the detection point are both located in the bedrock. That is,

$$u_2^t(\omega) = \frac{F(\omega)}{4\pi\rho_2c_2^2} \left\{ \pi j H_0(k_2 r_1) + j \int_{-\infty}^{\infty} \epsilon_2(\lambda) \frac{e^{j\alpha_2(x+x_s-2h)}}{\alpha_2} e^{j\lambda(y-y_s)} d\lambda \right\} \\ + \sum_{n=-\infty}^{\infty} (j\pi b_n) [H_n(rk_2) e^{jn\phi} + \sum_{m=-\infty}^{\infty} J_m(rk_2) e^{jm\phi} P_{nm}] \quad (129)$$

where:

$$r_1 = [r^2 + r_s^2 - 2rr_s \cos(\phi - \phi_s)]^{1/2};$$

$$r = [(x-H)^2 + (y-d)^2]^{1/2};$$

$$r_s = [(x_s-H)^2 + (y_s-d)^2]^{1/2};$$

$$\phi = \tan^{-1} \frac{(y-d)}{(x-H)};$$

$$\phi_s = \tan^{-1} \frac{(y_s-d)}{(x_s-H)};$$

$$\alpha_1 = (k_1^2 - \lambda^2)^{1/2}; \text{ and}$$

$$\alpha_1 = (k_2^2 - \lambda^2)^{1/2}.$$

To include attenuation and dispersion in Equation (129), the complex propagation constants for the surface layer and bedrock are

$$k_1 = \frac{\omega}{c_1(\omega)} + j\alpha_1(\omega)$$

and

$$k_2 = \frac{\omega}{c_2(\omega)} + j\alpha_2(\omega) ,$$

in which the absorption coefficients and the phase velocities are

$$\alpha_j(\omega) = \frac{\omega}{2Q_j c_j} (1 - e^{-\omega/\omega_0})$$

and

$$c_j(\omega) = c_j \left[1 - \frac{1}{\pi Q_j} \log \left(\frac{\omega}{\omega_0} \right) \right]^{-1}$$

for $j = 1, 2$.

To evaluate the integral P_{nm} in Equations (124) and (129), a numerical technique is developed in Appendix C. In addition, for the case of scattering from deep cavities, an approximate solution of the integral P_{nm} using the saddle-point method is derived in Appendix D.

The transient SH-wave displacement, $\hat{u}^t(t)$, corresponding to the steady-state solution given in Equation (35), may be represented as the sum of the incident time-dependent displacement, $\hat{u}_2^{(i)}(t)$, and the scattered displacement, $\hat{u}_2^{(s)}(t)$. That is,

$$\hat{u}_2^t(t) = \hat{u}_2^{(i)}(t) + \hat{u}_2^{(s)}(t) \quad (130)$$

The solution of the incident transient SH-wave displacement, $\hat{u}_2^{(i)}(t)$, for a line source located in the bedrock at (x_s, y_s) is derived in Appendix E. Thus, for a transient SH-wave pulse acting along the z -axis parallel to the cylindrical cavity and consisting of a body force, $f(t)$, the incident transient SH-wave displacement is expressed as

$$\hat{u}_2^{(i)}(t) = \frac{f(t)}{2\pi\rho_2 c_2^2} * \hat{T}^{(i)}(t) , \quad (131)$$

and its time derivative is

$$\frac{d\hat{u}_2^{(i)}(t)}{dt} = \frac{d}{dt} \left(\frac{f(t)}{2\pi\rho_2 c_2^2} * \hat{T}^{(i)}(t) \right) , \quad (132)$$

where:

$$\begin{aligned} \hat{T}^{(i)}(t) = & \frac{H(t-t_s)}{(t^2-t_s^2)^{1/2}} + \sum_{l=0}^{\infty} \operatorname{Im} \left[\frac{R^l(p)}{\alpha^2} \frac{dp}{dt} \right]_{p=p_{l+1}(t)} H(t-t_{l+1}) \\ & - \sum_{l=0}^{\infty} \operatorname{Im} \left[\frac{R^{l+1}(p)}{\alpha^2} \frac{dp}{dt} \right]_{p=p_l(t)} H(t-t_l) \end{aligned} \quad (133)$$

The first term of the transfer function, $\hat{T}^{(i)}(t)$, represents an incident SH wave traveling directly from the source to detector with a time of arrival given by

$$t_s = [(x-x_s)^2 + (y-y_s)^2]^{1/2} / c_2 \quad (134)$$

The last two terms of Equation (133) represent reflections in the bedrock and trapped reflections within the surface layer. Both terms are characterized by the reflection coefficient $R(p)$ and the arrival times t_l and t_{l+1} (for $l = 0, 1, 2, \dots, N$). These arrival times are given by

$$t_l = \frac{(x+x_s-2h)}{c_2 \cos \theta_2(l)} + \frac{2hl}{c_1 \cos \theta_1(l)} \quad (135)$$

and

$$t_{l+1} = \frac{(x+x_s-2h)}{c_2 \cos \theta_2(l+1)} + \frac{2h(l+1)}{c_2 \cos \theta_1(l+1)} \quad (136)$$

where $\theta_1(l)$, $\theta_1(l+1)$, $\theta_2(l)$, $\theta_2(l+1)$ are the angles of the ray trajectories in the surface layer and in the bedrock.

The scattered field displacement, $\hat{u}_2^{(s)}(t)$, can be expressed in the form of a one-dimensional Fourier transform over frequency as

$$\hat{u}_2^{(s)}(t) = \frac{1}{2\pi} \int_{-\infty}^{\infty} e^{-j\omega t} F(\omega) T^{(s)}(\omega) d\omega = f(t) * \hat{T}^{(s)}(t) \quad (137)$$

where:

$$T(s)(\omega) = -\frac{1}{4\pi\rho 2c_2^2} \sum_{n=-\infty}^{\infty} (j\pi b_n) [H_n(rk_2)e^{jn\phi} + \sum_{m=-\infty}^{\infty} J_m(rk_2)e^{jm\phi} P_{nm}] \quad (138)$$

and

$$\hat{T}(s)(t) = \frac{1}{2\pi} \int_{-\infty}^{\infty} T(s)(\omega) e^{-j\omega t} d\omega . \quad (139)$$

The corresponding time derivative for the scattered field displacement, $\hat{u}_2^{(s)}(t)$, is given by

$$\frac{d\hat{u}_2^{(s)}(t)}{dt} = \frac{d}{dt} (f(t) * \hat{T}(s)(t)) . \quad (140)$$

b. Check of the Steady-State Solution

In order to check the general SH-wave displacement solution given by Equation (129), the half-space solution for scattering SH waves from a cylindrical cavity may be derived directly from Equation (129) by letting $h \rightarrow 0$. In fact, in that case the function $\varepsilon_2(\lambda) \rightarrow 1$ and the second term of the incident SH-wave displacement becomes:

$$(\pi j) \frac{1}{\pi} \int_{-\infty}^{\infty} \frac{e^{j\alpha_2(x+x_s)}}{\alpha_2} e^{j\lambda(y-y_s)} d\lambda = \pi j H_0(k_2 r_2) \quad (141a)$$

where:

$$r_2 = [(y-y_s)^2 + (x+x_s)^2]^{1/2} .$$

In addition, the integral, P_{nm} , in the scattered SH-wave displacement term of Equation (129) and in the linear system of equations given by Equation (124) as $h \rightarrow 0$ are reduced to the Hankel function. That is, for $h \rightarrow 0$ and $\varepsilon(\lambda) \rightarrow 1$,

$$P_{nm} = (-j)^{n+m} \frac{1}{\pi} \int_{\Gamma} e^{2jk_2 H \cos \theta + j\theta(n+m)} d\theta = H_{n+m}(2k_2 H) . \quad (141b)$$

Using the addition theorem for the Hankel function,

$$H_n(Rk_2) e^{\pm jn\psi} = \sum_{m=-\infty}^{\infty} J_m(rk_2) H_{n+m}(2k_2 H) e^{\pm jm\phi} ,$$

the function, S_n , in Equation (124) becomes

$$S_n = \sum_{\lambda=-\infty}^{\infty} e^{-j\lambda\phi_s} J_{\lambda}(r_s k_2) H_{n+m}(2k_2 H) = H_n(r_s^H k_2) e^{-jn\phi_s^H} \quad (142)$$

where:

$$r_s^H = [r_s^2 + 4H^2 - 4Hr_s \cos \phi_s]^{1/2} ;$$

$$r_s = [(y_s - d)^2 + (x_s - H)^2]^{1/2} ;$$

$$\phi_s^H = \sin^{-1}(\sin \phi_s \frac{r_s}{r_s^H}) ; \text{ and}$$

$$\phi_s = \tan^{-1}(\frac{y_s - d}{x_s - H}) .$$

In the same manner, the second term of Equation (129) is reduced to

$$D_n = \sum_{m=-\infty}^{\infty} e^{jm\phi} J_m(r k_2) H_{n+m}(2k_2 H) = H_n(r_H k_2) e^{jn\phi_H} \quad (143)$$

where:

$$r_H = [r^2 + 4H^2 - 4rH \cos \phi]^{1/2} ;$$

$$r = [(y - d)^2 + (x - H)^2]^{1/2} ;$$

$$\phi = \tan^{-1} \frac{y - d}{x - H} ; \text{ and}$$

$$\phi_H = \sin^{-1}[\frac{r}{r_H} \sin \phi] .$$

Thus, the final solution for scattering of cylindrical SH waves by a cylindrical cavity in a half-space is

$$\sum_{m=-\infty}^{\infty} b_m [\delta_{nm} + \frac{J_n'(ka)}{H_n'(ka)} H_{n+m}(2kH)] = - \frac{F(\omega)}{4\pi\rho c^2} [H_n(kr_s^H) e^{-jn\phi_s^H} + H_n(kr_s) e^{-jn\phi_s}] ;$$

$$\text{for } n = 0, \pm 1, 2, \dots \pm \infty \quad (144)$$

and

$$u(\omega) = \frac{F(\omega)}{4\pi\rho c^2} [\pi j H_0(kr_1) + \pi j H_0(kr_2)] + \sum_{m=-\infty}^{\infty} (\pi j b_m) [H_m(kr) e^{jm\phi} + H_m(kr_H) e^{jm\phi_H}] . \quad (145)$$

This result is consistent with that derived using the image theory developed earlier for a cylindrical cavity in a homogeneous half-space.

c. The Steady-State Approximate Solution

For small air-filled cavities located at large distances from the layer-bedrock interface, the steady-state SH-wave solution given by Equation (129) can be simplified. In fact, when the total SH-wave displacement satisfies the stress-free boundary condition at the surface of the cavity, the effect of the surface layer may be neglected for a detector at the position $r = a$. In this case, the effect of the second term in the scattered SH-wave displacement is much smaller than that of the first term. Thus, under this condition the scattered SH-wave coefficients at the surface of the cavity may be determined using the following expression

$$b_n = - \frac{F(\omega)}{4\pi\rho c^2} \left\{ \frac{J_n'(k_2 a)}{H_n'(k_2 a)} [H_n(r_s k_2) e^{-jn\phi_s} + \sum_{\lambda=-\infty}^{\infty} e^{-j\lambda\phi_s} J_\lambda(r_s k_2) P_{\lambda n}] \right\} . \quad (146)$$

To obtain the scattered SH-wave displacement at the detector location, the coefficients, b_n , given by Equation (146) are substituted in Equation (128) to obtain the steady-state scattered SH-wave displacement

$$u(s) = - \frac{F(\omega)}{4\pi\rho c^2} \sum_{n=-\infty}^{\infty} \frac{J_n'(k_2 a)}{H_n'(k_2 a)} [H_n(r_s k_2) e^{-jn\phi_s} + S_n] [H_n(r k_2) e^{jn\phi} + D_n] \quad (147)$$

where:

$$S_n = \sum_{\lambda=-\infty}^{\infty} e^{-j\lambda\phi_s} J_\lambda(r_s k_2) P_{\lambda n} ;$$

$$D_n = \sum_{m=-\infty}^{\infty} e^{-jm\phi} J_m(r k_2) P_{nm} ;$$

$$r = [(x-H)^2 + (y-d)^2]^{1/2} ;$$

$$r_s = [(x_s-H)^2 + (y_s-d)^2]^{1/2} ;$$

$$\phi = \tan^{-1}\left(\frac{y-d}{x-H}\right) ; \text{ and}$$

$$\phi_s = \tan^{-1}\left(\frac{y_s-d}{x_s-H}\right) .$$

d. The High-Frequency Limit Approximation

To reduce the computations necessary to produce synthetic seismograms and as a check on the theoretical analysis, a high-frequency limit approximation for the scattered SH-wave particle displacement is derived. This solution may be obtained by substituting the function P_{nm} given by Equation (D-17) into Equation (128) to yield

$$\begin{aligned} u(s) = & \sum_{n=-\infty}^{\infty} (j\pi b_n) [H_n(rk_2)e^{jn\phi} - R_0 H_n(k_2 r_a)e^{jn\phi_a} \\ & + \sum_{\ell=1}^N a_{\ell} R_0^{\ell} (R_0^{-1} - R_0) H_n[k_2 r_a(\ell)] e^{jn\phi_a(\ell)}] \end{aligned} \quad (148a)$$

where:

$$R_0 = \frac{\xi^2 v - 1}{\xi^2 v + 1} ;$$

$$r_a = [r^2 + 4(H-h)^2 - 4r(H-h) \cos \phi]^{1/2} ;$$

$$\phi = \tan^{-1} \frac{y-d}{x-h} ;$$

$$a_{\ell} = \left(\frac{1 + h\ell v / (H-h)}{1 + h\ell / v(H-h)} \right)^{1/2} ;$$

$$\phi_a = \sin^{-1} \left(\frac{r}{r_a} \sin \phi \right) ;$$

$$r_a(\ell) = [r^2 + s_\ell^2 - 2s_\ell r \cos \phi]^{1/2};$$

and

$$\phi_a(\ell) = \sin^{-1} \left(\frac{r}{r_a(\ell)} \sin \phi \right);$$

in which

$$s_\ell = 2(H - h + h\ell v);$$

$$\xi^2 = \mu_1/\mu_2;$$

and

$$v = k_1/k_2.$$

The numerical solution of Equation (148a) for the scattered SH-wave particle displacement is produced by the computer program scat_pulse in Appendix H.

The scattered-wave coefficients, b_n , may be obtained from Equation (146). Here, the source function, S_n , in the high-frequency limit approximation is given by

$$S_n \equiv -R_0 e^{-jn\psi_s^{(0)}} H_n[k_2 r_s^{(0)}] + \sum_{\ell=1}^{\infty} a_\ell F_0^\ell e^{-jn\psi_s^{(\ell)}} H_n[k_2 r_s^{(\ell)}] \quad (148b)$$

where:

$$F_0^\ell = (R_0^{-1} - R_0) R_0^\ell$$

$$r_s^{(0)} = [r_s^2 + 4(H-h)^2 - 4(H-h)r_s \cos \phi_s]^{1/2}$$

$$r_s(\ell) = [r_s^2 + s_\ell^2 - 4(H-h)s_\ell \cos \phi_s]^{1/2}$$

$$\psi_s^{(0)} = \sin^{-1} \left(\frac{r_s}{r_s^{(0)}} \sin \phi_s \right)$$

$$\psi_s(\ell) = \sin^{-1} \left(\frac{r_s}{r_s(\ell)} \sin \phi_s \right).$$

In a similar manner, the high-frequency limit approximation for the incident SH-wave displacement may be derived by substituting the function P_{nm} in Equation (VI-17) into Equation (115) to obtain

$$\begin{aligned}
 u_2(i) = & \frac{F(\omega)}{4\pi\rho 2c_2^2} (\pi j) \left\{ H_0(k_2|r-r_s|) + \sum_{m=-\infty}^{\infty} e^{-jm\phi} J_m(k_2r_s) \right. \\
 & \times \sum_{n=-\infty}^{\infty} e^{jn\phi} J_n(rk_2) \{ -R_0 H_{n+m}(2k_2(H-h)) \} \\
 & \left. + \sum_{\ell=1}^{\infty} a_{\ell} (R_0^{-1} - R_0^{\ell}) R_0 H_{n+m}(k_2s_{\ell}) \right\} \quad (149)
 \end{aligned}$$

or

$$\begin{aligned}
 u_2(i) = & \frac{F(\omega)}{4\pi\rho 2c_2^2} (\pi j) \left\{ H_0(k_2|r-r_s|) - R_0 \sum_{m=-\infty}^{\infty} e^{jn(\psi_b - \phi_s)} J_m(k_2r_s) H_n(k_2r_b) \right. \\
 & \left. + \sum_{\ell=1}^{\infty} a_{\ell} (R_0^{-1} - R_0) R_0^{\ell} \sum_{n=-\infty}^{\infty} e^{jn(\psi_b^{(\ell)} - \phi_s)} J_n(k_2r_s) H_n(k_2r_b^{(\ell)}) \right\} . \quad (150)
 \end{aligned}$$

Finally, Equation (150) is further reduced to yield the SH-wave particle displacement

$$\begin{aligned}
 u_2(i) = & \frac{F(\omega)}{4\pi\rho 2c_2^2} (\pi j) \left\{ H_0(k_2|r-r_s|) - R_0 H_0(k_2r_t) \right. \\
 & \left. + \sum_{\ell=1}^N a_{\ell} (R_0^{-1} - R_0) R_0^{\ell} H_0(k_2r_t^{(\ell)}) \right\} . \quad (151)
 \end{aligned}$$

where:

$$r_b = [r^2 + 4(H-h)^2 - 4r(H-h) \cos \phi]^{1/2}$$

$$\phi_b = \sin^{-1} \left(\frac{r_s}{r_b} \sin \phi \right)$$

$$r_b(\ell) = [r^2 + s_\ell^2 - 2s_\ell r \cos \phi]^{1/2}$$

$$\phi_b(\ell) = \sin^{-1} \left(\frac{r_s}{r_b(\ell)} \sin \phi \right)$$

$$r_t = [r_s^2 + r_b^2 - 2r_s r_b \cos (\phi_b - \phi_s)]^{1/2}$$

and

$$r_t(\ell) = \{r_s^2 + [r_b(\ell)]^2 + 2r_s r_b(\ell) \cos [\phi_b(\ell) - \phi_s]\}^{1/2}.$$

The numerical solution of Equation (151) is produced by the computer program `inc_pulse` in Appendix H. To simplify the calculations, the geometric relationships given in Equations (148) and (151) may be deduced directly from Figure 11-9. In terms of the detector and its image coordinates, the distances and angles included in the SH-wave scattering equation are given by

$$r(o) \equiv r_a = [(y-d)^2 + (x+H-2h)^2]^{1/2}$$

$$\phi(o) \equiv \phi_a = \tan^{-1} \left(\frac{y-d}{x+H-2h} \right)$$

$$r(\ell) \equiv r_a(\ell) = \{(y-d)^2 + [x+H+2(\ell v-1)h]^2\}^{1/2}$$

and

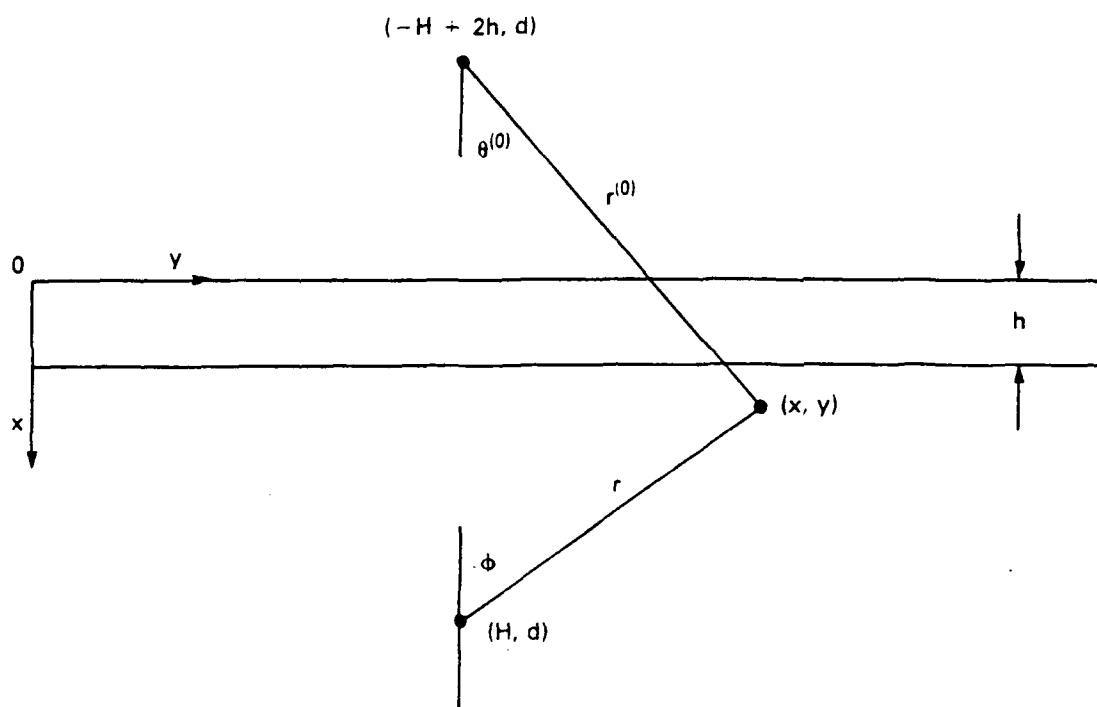
$$\phi(\ell) \equiv \phi_a(\ell) = \tan^{-1} \left(\frac{y-d}{x+H+2(\ell v-1)h} \right).$$

For the incident SH-wave displacement, the new distances are

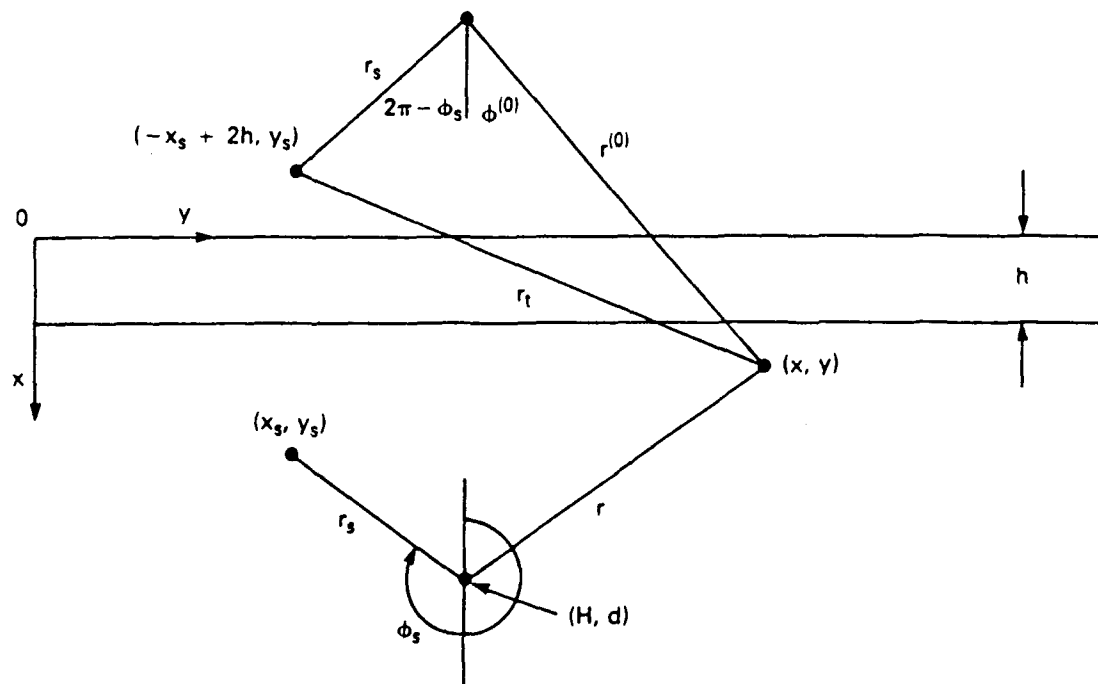
$$r_s(o) \equiv r_t = [(y-y_s)^2 + (x+x_s-2h)^2]^{1/2}$$

and

$$r_s(\ell) \equiv r_t(\ell) = \{(y-y_s)^2 + [x+x_s+2(\ell v-1)h]^2\}^{1/2}.$$



(a)



(b)

FIGURE II-9. GEOMETRY OF THE ZERO ORDER TERM DISTANCES AND ANGLES
FOR SH-WAVE DISPLACEMENTS

(a) Scattered Waves (b) Direct Waves

5. Integral Equation Solution for SH-Wave Scattering from a Cylindrical Cavity in a Two-Layer Half-Space for the Detector in the Surface Layer

After the value for the total SH-wave displacement, u^t , at the surface of the cavity ($r = a$) is known, the scattered wave in the field $0 < x < h$ may be derived from the second term of Equation (B-9) for the surface layer Green's functions, G_1 , as

$$u_1(s) = \int_S u^t(r') \frac{\partial G_1(r, r')}{\partial \hat{r}'} dS; \quad \text{for } r \text{ in } V.$$

where $u^t(r')$ is given by Equation (120). The integration of Equation (152) is carried out in the same manner as was done for the case of a detector in the bedrock. That is,

$$u_1(s) = \frac{a}{4\pi} \int_0^{2\pi} \sum_{\lambda=-\infty}^{\infty} B_{\lambda} e^{j\lambda\phi'} \sum_{m=-\infty}^{\infty} j\pi J_m'(ak_2) e^{-jm\phi'} d\phi' \times \sum_{n=-\infty}^{\infty} e^{jn\phi} J_n(rk_2) Q_{nm} \quad (153)$$

or

$$u_1(s) = \pi j \sum_{m=-\infty}^{\infty} \frac{a}{2} B_m J_m'(ak_2) \sum_{n=-\infty}^{\infty} e^{jn\phi} J_n(rk_2) Q_{nm}. \quad (154)$$

In terms of the wave coefficients, b_m , Equation (154) is expressed as

$$u_1(s) = \sum_{m=-\infty}^{\infty} (j\pi b_m) \sum_{n=-\infty}^{\infty} e^{jn\phi} J_n(rk_2) Q_{nm}, \quad (155)$$

where Q_{nm} is given by Equation (110).

a. Steady-State and Transient Solutions

Superposition of the incident and scattered SH-wave displacements, $u_1(i)$ and $u_1(s)$, given by Equations (117) and (155), respectively, leads to the steady-state solution for the total SH-wave particle displacement for the line source in the bedrock and the detection point in the surface layer as

$$\begin{aligned}
u_1^t(\omega) = & \frac{F(\omega)}{4\pi\rho_2c_2^2} \sum_{m=-\infty}^{\infty} j\pi J_m(r_s k_2) e^{-jm\phi_s} \sum_{n=-\infty}^{\infty} e^{jn\phi} J_n(rk_2) Q_{nm} \\
& + \sum_{m=-\infty}^{\infty} (j\pi b_m) \sum_{n=-\infty}^{\infty} e^{jn\phi} J_n(rk_2) Q_{nm} . \quad (156)
\end{aligned}$$

where:

$$r = [(x-H)^2 + (y-d)^2]^{1/2} ;$$

$$r_s = [(x_s-H)^2 + (y_s-d)^2]^{1/2} ;$$

$$\phi = \tan^{-1} \frac{(y-d)}{(x-H)} ;$$

and

$$\phi_s = \tan^{-1} \frac{(y_s-d)}{(x_s-H)} .$$

To include attenuation and dispersion in Equation (156), the complex propagation constants for the surface layer and bedrock are given by

$$k_1 = \frac{\omega}{c_1(\omega)} + j\alpha_1(\omega)$$

and

$$k_2 = \frac{\omega}{c_2(\omega)} + j\alpha_2(\omega)$$

in which the absorption coefficients and the phase velocities are

$$\alpha_j(\omega) = \frac{\omega}{2Q_j c_j} (1 - e^{-\omega/\omega_0})$$

and

$$c_j(\omega) = c_j \left[1 - \frac{1}{\pi Q_j} \log \left(\frac{\omega}{\omega_j} \right) \right]^{-1}$$

for $j = 1, 2$.

For the use of scattering from deep cavities, an approximate solution of the integral, Q_{nm} , using the saddle-point method is derived in Appendix F.

The transient SH-wave displacement, $\hat{u}_1^t(t)$, corresponding to the steady-state solution given in Equation (156), may be represented as the sum of the incident time-dependent displacement, $u_1^{(i)}(t)$, and the scattered displacement, $u_1^{(s)}(t)$. That is,

$$\hat{u}_1^t(t) = \hat{u}_1^{(i)}(t) + \hat{u}_1^{(s)}(t) . \quad (157)$$

The solution of the incident transient SH-wave displacement, $u_1^{(i)}(t)$, for the line source in the bedrock at (x_s, y_s) and the detector in the surface layer is derived in Appendix F. Thus, for a transient SH-wave pulse acting along the z-axis parallel to the cylindrical cavity and consisting of a body force, $f(t)$, the incident transient SH-wave displacement is expressed as

$$\hat{u}_1^{(i)} = \frac{f(t)}{2\pi\rho_2 c_2^2} * \hat{T}^{(i)}(t) , \quad (158)$$

and its time derivative is

$$\frac{d\hat{u}_1^{(i)}}{dt}(t) = \frac{1}{2\pi\rho_2 c_2^2} \frac{d}{dt} [f(t) * \hat{T}_1^{(i)}(t)] , \quad (159)$$

where:

$$\hat{T}_1^{(i)} = 2 \sum_{\ell=0}^N \text{Im} \left[\frac{T(p) R^\ell(p)}{\alpha_2(p)} \frac{dp}{dt} \right]_{p=p_\ell(t)} H(t-t_\ell) ,$$

in which $p_\ell(t)$ is a solution of the nonlinear equation given by

$$t = p(y-y_s) + \left(\frac{1}{c_2^2} - p^2 \right)^{1/2} (x_s - h) + \left(\frac{1}{c_1^2} - p^2 \right)^{1/2} h(2\ell+1) .$$

Each term of Equation (159) represents reflections within the surface layer. These terms are characterized by the reflection coefficient $R(p)$ and the arrival times t_ℓ (for $\ell = 0, 1, 2, \dots, N$). The equation to determine the arrival times for the detector at the surface is

$$t_\ell = \frac{x_s - h}{c_2 \cos \theta_2(\ell)} + \frac{h(2\ell+1)}{c_1 \cos \theta_1(\ell)} \quad (160)$$

where the angles θ_1 and θ_2 are the angles of the ray trajectories in the surface layer and in the semi-infinite half-space, respectively.

The scattered field displacement, $\hat{u}_1(s)(t)$, can be expressed in the form of one-dimensional Fourier transform over frequency as

$$\hat{u}_1(s)(t) = \frac{1}{2\pi} \int_{-\infty}^{\infty} e^{-j\omega t} F(\omega) T_1(s)(\omega) d\omega = f(t) * \hat{T}_1(s)(t) \quad (161)$$

where:

$$T_1(s)(\omega) = - \frac{1}{4\pi\rho_2 c_2^2} \sum_{n=-\infty}^{\infty} (j\pi b_n) \sum_{m=-\infty}^{\infty} e^{jm\phi} J_m(rk_2) Q_{nm}$$

and

$$\hat{T}_1(s)(t) = \frac{1}{2\pi} \int_{-\infty}^{\infty} T_1(s)(\omega) e^{-j\omega t} d\omega .$$

The corresponding time derivative for the scattered field displacement, $\hat{u}_1(s)(t)$, is given by

$$\frac{d\hat{u}_1(t)}{dt} = \frac{d}{dt} [f(t) * \hat{T}_1(s)(t)] . \quad (162)$$

b. The High-Frequency Limit Approximation

The high-frequency limit approximation of the scattered SH-wave displacement for a detector at the surface of the earth is obtained by replacing the approximate solution of Q_{nm} as given by Equation (F-15) into Equation (155). The resulting particle displacement is

$$u_1(s) \cong 2 \sum_{l=0}^{\infty} b_l T_0 R_0^l \sum_{m=-\infty}^{\infty} (j\pi b_m) \sum_{n=-\infty}^{\infty} e^{jn\phi} J_n(rk_2) H_{n+m}(k_2 r_l) \quad (163)$$

where:

$$r_l = (2H-h) + (2l+1)hv$$

$$T_0 = \frac{2}{\xi^2 v + 1}$$

$$R_0 = \frac{\xi^2 v - 1}{\xi^2 v + 1}$$

$$b_l = \frac{\left[1 + \frac{(2l+1)vh}{2H-h} \right]^{1/2}}{1 + \frac{(2l+1)h/v}{2H-h}}$$

and

$$v = k_1/k_2 .$$

The solution given by Equation (163) can be further reduced by introducing the identity

$$H_m(k_2 R_l) e^{jm\psi_l} = \sum_{n=-\infty}^{\infty} e^{jn\phi} J_n(rk_2) H_{n+m}(k_2 r_l) . \quad (164)$$

Therefore, by substituting Equation (164) into Equation (163), the SH-wave displacement becomes

$$u_1(s) \cong 2 \sum_{l=0}^{\infty} a_l T_0 R_0^l \sum_{m=-\infty}^{\infty} (j\pi b_m) H_m(k_2 \bar{r}_l) e^{jm\psi_l} \quad (165)$$

where:

$$\bar{r}_l = [r^2 + r_l^2 - 2rr_l \cos \phi]^{1/2} ;$$

$$r = [H^2 + (y-d)^2]^{1/2} ;$$

$$\psi_l = \sin^{-1} \left(\frac{r}{\bar{r}_l} \sin \phi \right) ;$$

$$\xi^2 = \mu_1/\mu_2$$

and

$$v = k_1/k_2 .$$

The numerical solution of Equation (165) for the scattered SH-wave displacement is calculated by the computer program scat_pulse2 in Appendix H. In a

similar manner, the high-frequency limit solution for the incident SH-wave displacement may be obtained by substituting the approximation of Q_{nm} into Equation (117). That is,

$$u_1(i) \equiv \frac{F(\omega)}{4\pi\rho 2c_2^2} \sum_{\ell=0}^{\infty} 2b_{\ell} T_0 R_0^{\ell} \sum_{m=-\infty}^{\infty} j\pi J_m(r_s k_2) e^{-jm\phi_s} \times \sum_{n=-\infty}^{\infty} e^{jn\phi} J_n(rk_2) H_{n+m}(k_2 r_{\ell}) . \quad (166)$$

The substitution of the identity given by Equation (164) into Equation (166) leads to a reduced form of the high-frequency limit solution for the direct SH-wave displacement. That is,

$$u_1(i) \equiv \frac{F(\omega)}{4\pi\rho 2c_2^2} \sum_{\ell=0}^N 2b_{\ell} T_0 R_0^{\ell} H_0[k_2 \bar{r}_s(\ell)] \quad (167)$$

where:

N = the number of reflections ;

$$\bar{r}_s(\ell) = [r_s^2 + \bar{r}_{\ell}^2 - 2r_s \bar{r}_{\ell} \cos(\phi_{\ell} - \phi_s)]^{1/2} ;$$

$$r_s = [(x_s - H)^2 + (y_s - d)^2]^{1/2} ;$$

$$\bar{r}_{\ell} = [r^2 + r_{\ell}^2 - 2rr_{\ell} \cos \phi]^{1/2} ;$$

and

$$\phi_{\ell} = \sin^{-1} \left(\frac{r}{\bar{r}_{\ell}} \sin \phi \right) .$$

The numerical solution of Equation (167) for the direct SH-wave displacement is calculated by the computer program `inc_pulse2` in Appendix H.

Finally, the high-frequency limit approximation of the total SH-wave displacement as measured for a detector at the surface of the earth is given by

$$u_1 t \cong \frac{F(\omega)}{4\pi\rho_2 c_2^2} \sum_{\ell=0}^N 2b_\ell T_O R_O^\ell j\pi H_O[k_2 \bar{r}_s(\ell)] \\ + \sum_{\ell=0}^N 2b_\ell T_O R_O^\ell \sum_{m=-\infty}^{\infty} (j\pi b_m) H_m(k_2 \bar{r}_\ell) e^{jm\psi_\ell}, \quad (168)$$

where the scattered-wave coefficients, b_m , are obtained from Equation (146). In this equation, the optical limit approximation of the function, S_n , is given by Equation (148b).

In order to simplify calculations, more appropriate expressions for the distance, \bar{r}_ℓ and $\bar{r}_s(\ell)$, and the angle, ψ_ℓ , may be deduced directly from Figure II-10. These are

$$\bar{r}_O = \{[y-d]^2 + [H-h(1-\nu)]^2\}^{1/2};$$

$$\bar{r}_\ell = \{[y-d]^2 + [H-h+\nu h(1+2\ell)]^2\}^{1/2};$$

$$\psi_O = \tan^{-1} \left(\frac{y-d}{H-h+\nu h} \right)$$

$$\psi_\ell = \tan^{-1} \left[\frac{y-d}{H-h+\nu h(1+2\ell)} \right]$$

$$\bar{r}_s(o) = \{(y-y_s)^2 + (x_s-h+\nu h)^2\}^{1/2};$$

and

$$\bar{r}_s(\ell) = \{(y-y_s)^2 + (x_s-h+\nu h(1+2\ell))^2\}^{1/2}.$$

6. Numerical Applications using the Transient Analytical Solutions

To demonstrate the applicability of the Cagniard-deHoop technique and as a check on the numerical evaluations, SH-wave pulses associated with a line source in the bedrock are presented for the surface layer models

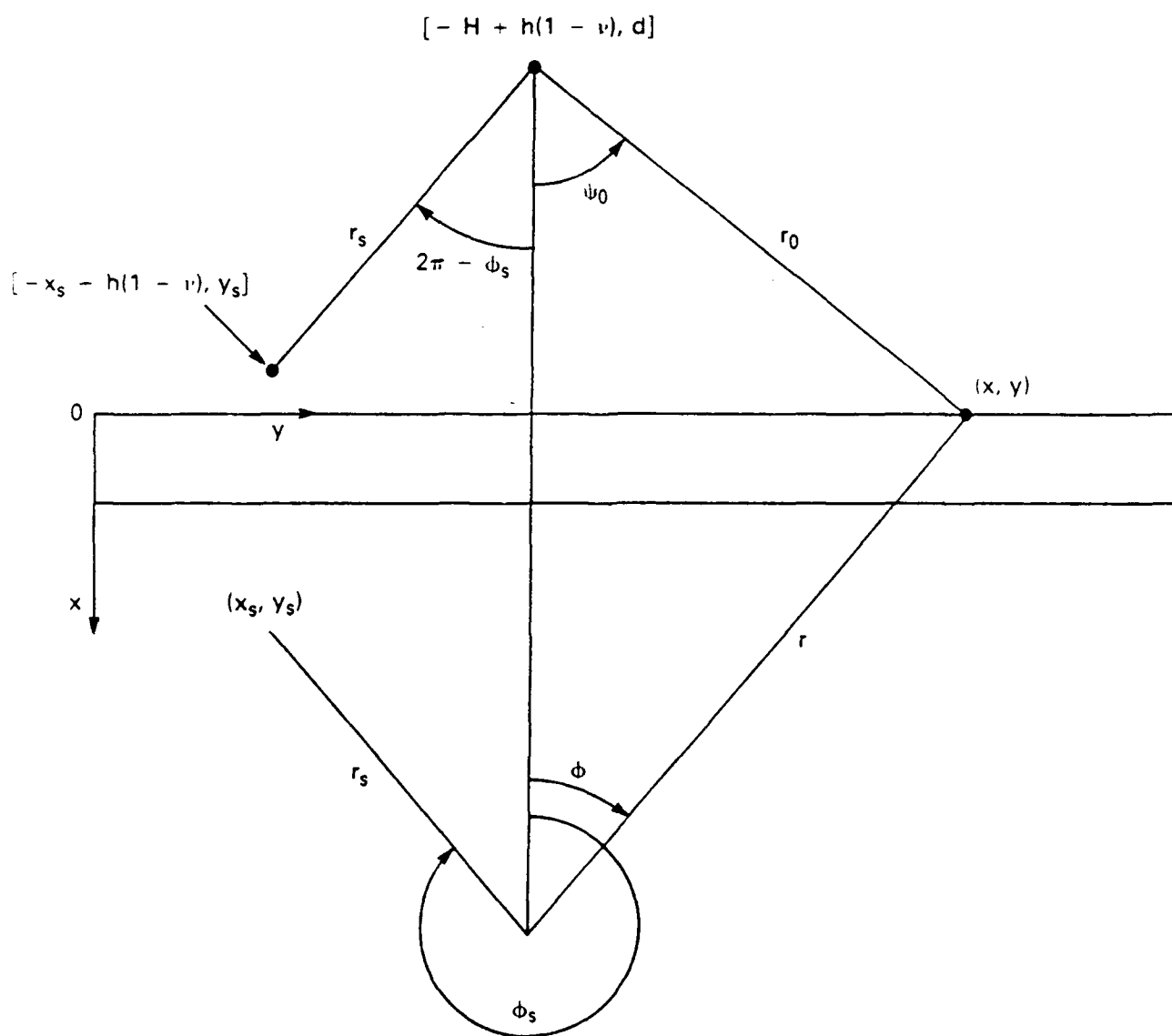


FIGURE II-10. GEOMETRY OF THE ZERO ORDER TERM DISTANCE AND ANGLE FOR THE SCATTERED AND INCIDENT SH-WAVE DISPLACEMENTS

shown in Figure II-11. The source depth is 15 m, the horizontal source-detector distance is 20 m, the surface-layer thickness is $h = 10$ m, and the constitutive parameters in the sediment and the bedrock are $c_1 = 500$ m/sec, $\rho_1 = 1.5$ gr/cm³, $c_2 = 2,500$ m/sec, and $\rho_2 = 2.5$ gr/cm³. The SH-wave pulse signal transmitted by the line-source is defined by

$$f(t) = \beta t e^{-\beta t} \sin(2\pi f_0) u(t),$$

where:

$$\beta = 1.8 f_0$$

and

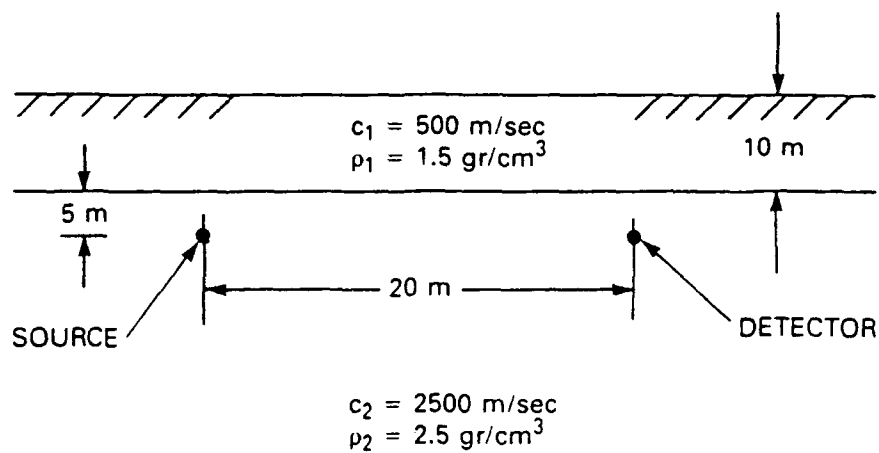
$$f_0 = 1,000 \text{ Hz.}$$

Figure II-12 shows SH-wave pulse responses computed for the two-layer earth model illustrated in Figure II-11(a). The detector is in the bedrock close to the surface layer interface at a depth of 15 m. The total seismic signal shown in Figure II-12 was computed by the superposition of the effects of the direct SH-wave pulse having an arrival time of $t_s = 8$ msec and three reflected SH-wave pulses having arrival times of $t_0 = 8.9$ msec, $t_1 = 48$ msec, and $t_2 = 88$ msec, respectively.

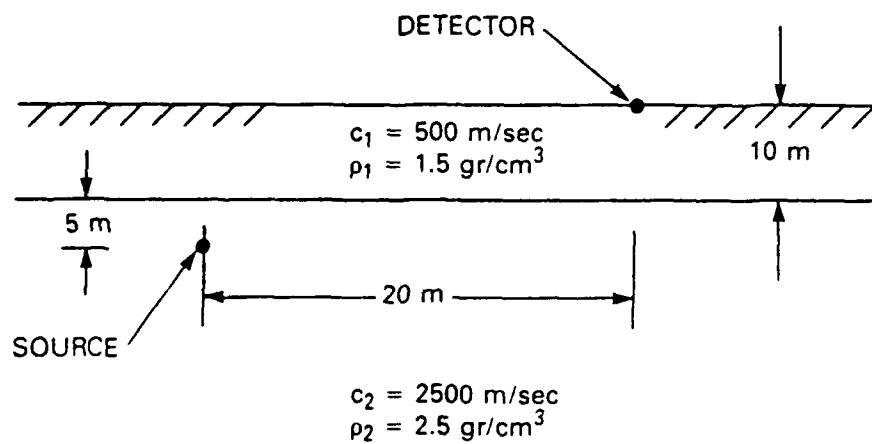
Because of the small arrival time difference, $\Delta t = 0.9$ msec, between the direct pulse and the first reflection, these two waveforms appear in Figure II-12 as a single pulse having an arrival time of 8 msec. As expected, when the effective source-detector separation becomes larger, the number of multiples in the surface layer will increase.

In order to investigate the individual reflected waveforms, the total SH-wave pulse without the masking effect of the direct SH-wave pulse is illustrated in Figure II-13. Here, the first and second reflected pulses exhibit the same polarity because of their similar geometrical ray path. In fact, the first SH-wave pulse is reflected back to the detector at the boundary between the surface layer and the lower half-space, while the second pulse is reflected back to the detector at the air-earth interface. Alternatively, the third SH-wave pulse is reflected once in the surface layer where it changes polarity and then it follows a trajectory similar to that of the previous pulses.

Figure II-14 shows computed SH-wave pulses for a detector at the surface as shown in Figure II-11(b). In this case, the total field was obtained by the superposition of pulses having arrival times of $t_1 = 27$ msec, $t_2 = 67$ msec, and $t_3 = 108$ msec, respectively. These waveforms exhibit alternating polarities. For example, the first pulse follows a positive trajectory, the second pulse changes polarity by reflecting once at the bottom of the surface layer, and the third pulse exhibits positive polarity by reflecting twice the surface.



(a)



(b)

FIGURE II-11. TWO-LAYER EARTH MODEL AND LINE SOURCE IN THE BEDROCK
 (a) Detector in the bedrock (b) Detector on the surface of the earth

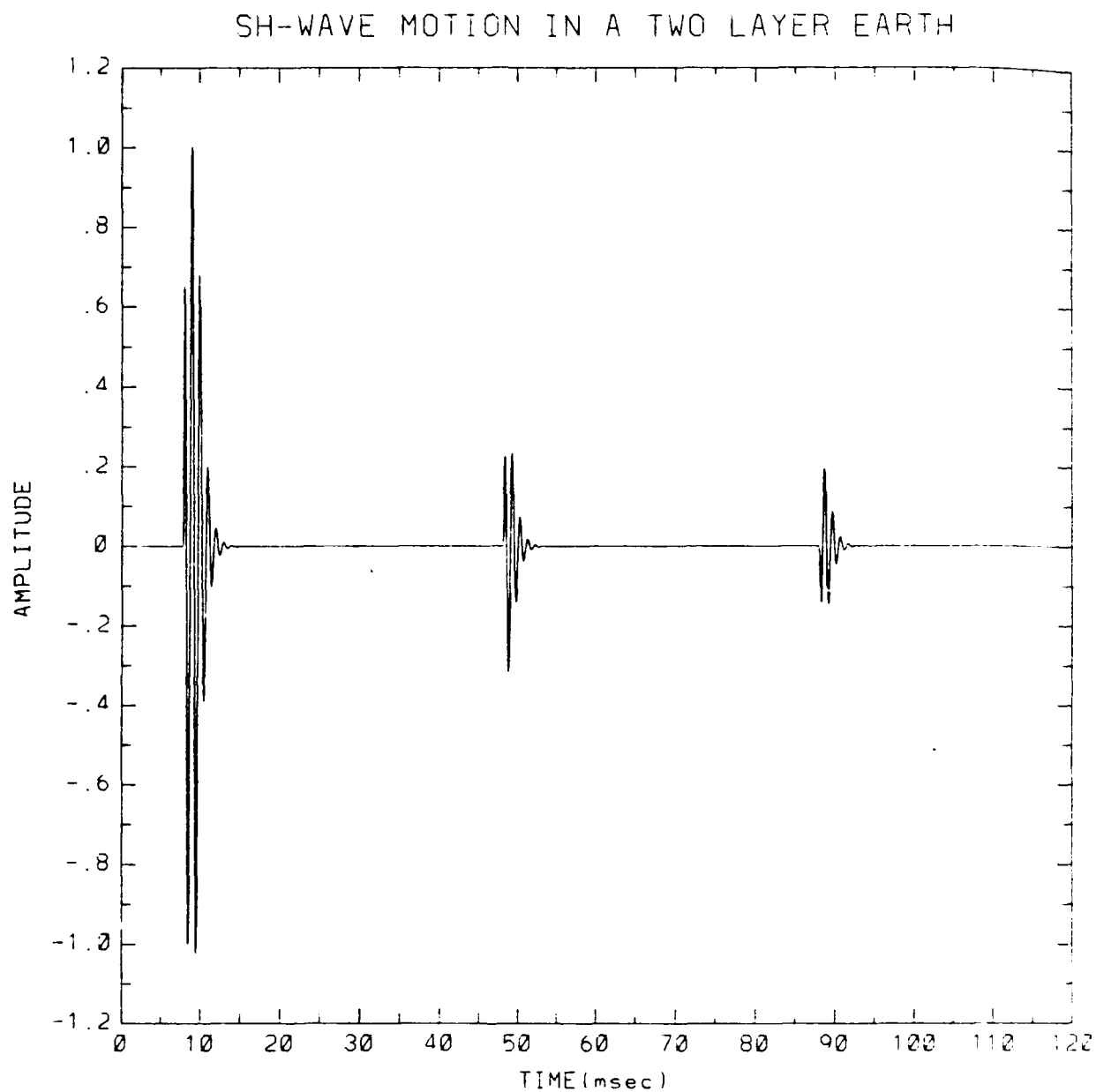


FIGURE II-12. THE TOTAL SH-WAVE TRANSIENT RESPONSE FOR THE SH-LINE SOURCE AND THE DETECTOR IN THE BEDROCK

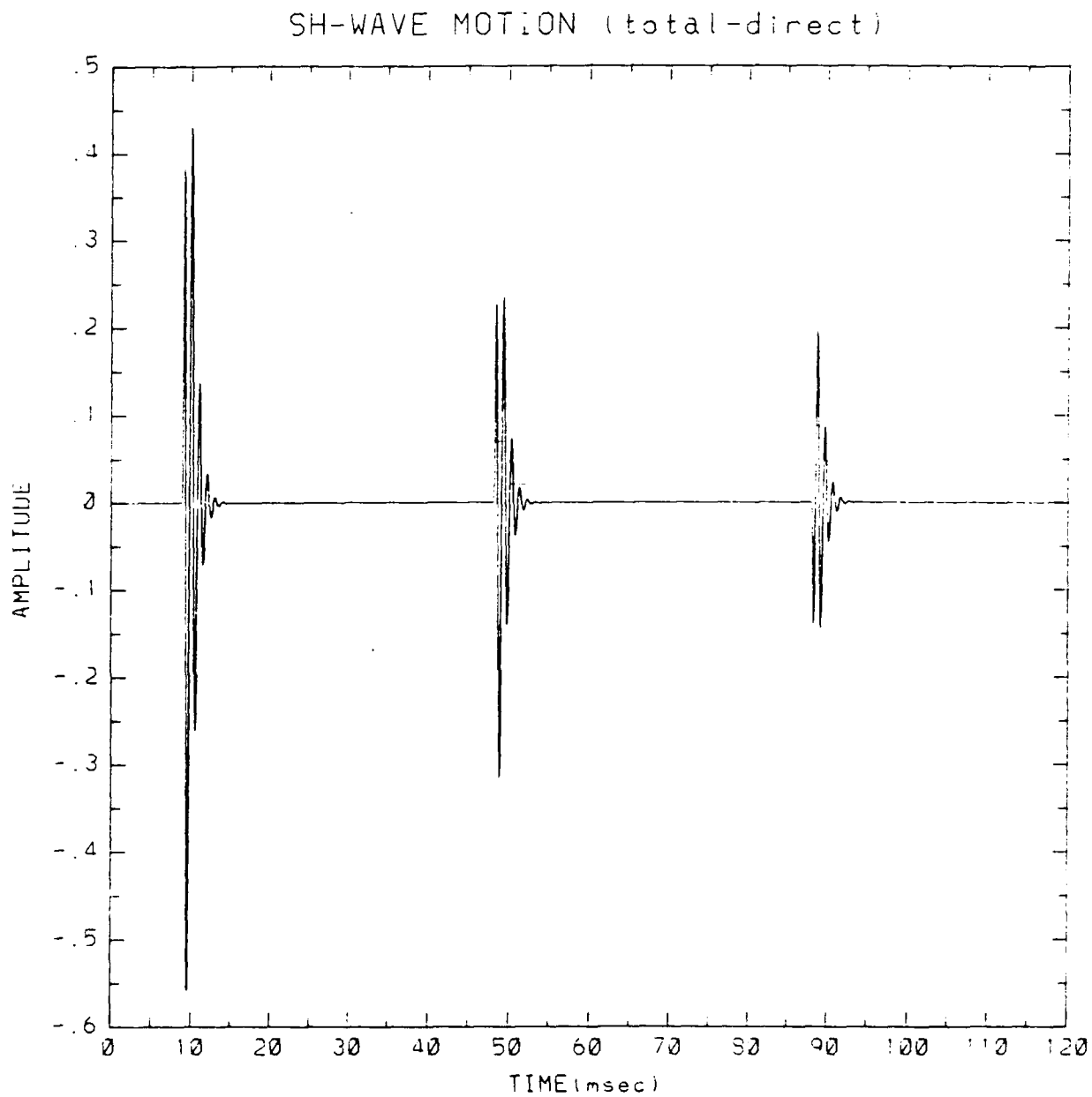


FIGURE II-13. THE TOTAL SH-WAVE TRANSIENT RESPONSE WITHOUT THE DIRECT PULSE FOR THE SH-LINE SOURCE AND THE DETECTOR IN THE BEDROCK

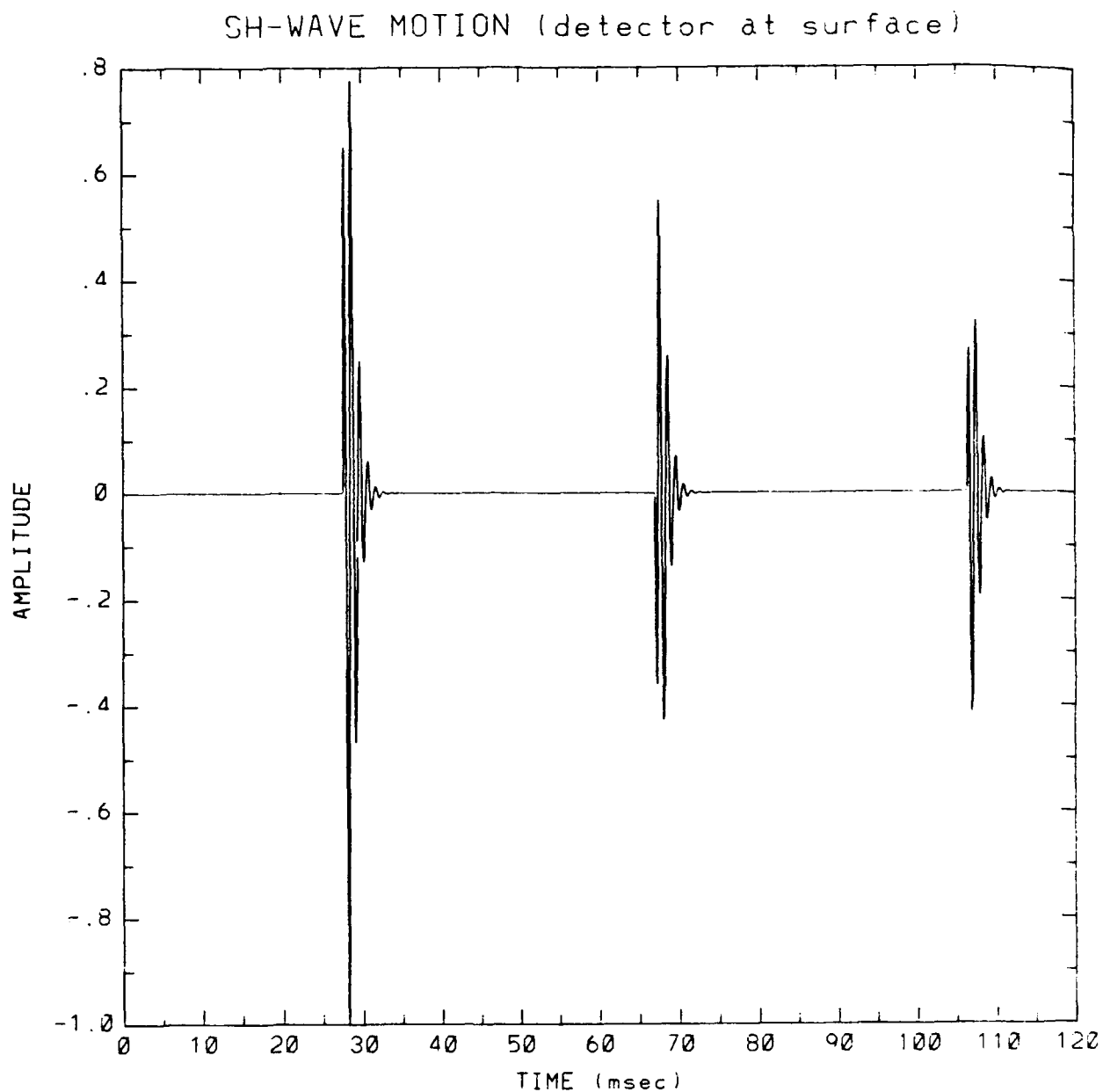


FIGURE II-14. SYNTHETIC SEISMIC PULSES ASSOCIATED WITH THE SH-LINE SOURCE FOR THE BEDROCK AND THE DETECTOR AT THE SURFACE OF A TWO-LAYER LOSSLESS HALF-SPACE

III. NUMERICAL EVALUATION OF MODELS

The progressive theoretical analyses presented in Section II address SH-wave scattering from a cylindrical cavity in the simple case of plane waves in an unbounded medium to the more representative cases of cylindrical and spherical SH-wave scattering in a half-space. The effects of dissipative absorption in the two-layer medium were introduced to yield practical information on the scattered seismic signal amplitudes required to be detected and the various masking effects imposed by the low-quality weathered layer at the surface. The special considerations for performing the numerical evaluations in each case are discussed below.

A. Plane Wave Source in a Lossless Unbounded Medium

The numerical solution for plane wave scattering from a cylindrical cavity in a lossless unbounded medium was developed using Equation (26) presented earlier. The plane wave case allows an arbitrary unit amplitude to be assigned to the incident wave so that the scattered wave values can be scaled as fractions of the incident wave. By formulating the frequency dependent terms in units of wavenumber multiplied by the cavity radius, the calculations were generalized to any frequency range or cavity size by specifying the frequency, the velocity, and the cavity radius in proper combinations. Programs were written to calculate the energy-scattering cross-section and the SH-wave displacement as functions of frequency, source and detector geometry, and cavity target distance from the detector while holding other parameters such as the SH-wave velocity and mass density of the medium constant.

1. Overview of the Plane Wave Analysis Computer Programs

Several computer programs were developed to provide plane wave scattering results for horizontally polarized shear waves in several informative formats. First, the total energy-scattering cross-section of the cylindrical cavity target is computed as a function of frequency to illustrate the effects on scattering efficiency as governed by the incident wavelength and the cavity diameter. Next, the scattered SH-wave displacement amplitude at the surface of the cavity is computed as a function of angle about the cavity axis relative to the incident wave direction and for several frequencies to fundamentally characterize the angular scattering signature of such targets. This same form of calculation is next carried out for several detector distances away from the cavity axis to illustrate the geometrical spreading losses and the far-field angular scattering signatures of the cavity target. Finally, the plane-wave analysis program is adapted to simulate a plane-wave source and a line of detectors positioned within the whole-space medium to represent a seismic survey traverse. SH-wave displacement amplitudes as might be detected at points along this survey line are calculated as functions of the cavity depth below the traverse line and for several source signal frequencies. All of these plane-wave computations are for steady-state source signals whose wavelengths are significantly larger than, about equal to, and significantly smaller than the cylindrical cavity diameter.

In each program, the numerical calculations consist of summations of terms involving Bessel and Hankel functions representing the scattered wave fields as functions of the geometrical and frequency parameters. These

summations are performed over at least 15 iterations and up to a maximum of 50 iterations until the difference in computed values between two successive iterations is less than 0.01 percent of the calculated value. In all of the computer programs except that for the total energy scattering cross-section, this summation is performed by the subroutine called `plane_scatter`. The computer codes for the plane-wave analysis programs and subroutines are written in FORTRAN 77 language and are presented in Appendix H, Section H.1.

a. Energy Scattering Cross-Section Calculation

The program called `csect` computes the total energy scattering cross-section of a cylindrical cavity when illuminated broadside by a plane SH-wave. This cross-section, discussed earlier in Section II.B.3, is calculated for values of wavenumber times cavity radius (i.e., ka) ranging from 0.05 to 2.0 in increments of 0.05.

b. SH-Wave Displacement Amplitude

Four programs are used to calculate the displacement amplitudes of plane SH-waves scattered from a cylindrical cavity in a homogeneous whole-space.

The first program, `dispa`, calculates the amplitude of the total displacement field as a function of frequency at three different positions on the surface of the cavity. The frequency is contained in the factor, ka , for values ranging from 0 to 2 in steps of 0.05 and from 2.1 to 10 in steps of 0.1. The locations at the surface of the cavity at which the calculations are evaluated are on radii at 45, 90, and 135 degrees relative to the incident wave vector. The displacement amplitude is a complex quantity expressed in terms of amplitude and phase, which is unwrapped.

The second program, `dispb`, calculates the total displacement amplitude as a function of distance from the cavity, along three different radial lines and at three different frequencies. The distance is expressed in terms of the radial distance divided by the cavity radius (i.e., r/a) calculated from values of 1 to 10 in steps of 0.5. The angles of the radial lines along which the displacements are calculated are 45, 90, and 135 degrees with respect to the incident wave vector. The frequencies at which the results are obtained are expressed in terms of the factor, ka , and are 0.5, 1, and 2. The displacement amplitude is a complex quantity, but only the magnitude of this quantity is used as output.

The third program, `dispcd`, calculates the amplitude of the scattered SH-wave displacement field as functions of angle, detector distance from the cavity, and frequency. Depending upon whether a certain section of code noted in the program listing is commented out or not, the program will provide either the scattered amplitude only or the combined direct and scattered amplitude. The scattered amplitude is calculated at angles from 0 to 180 degrees in steps of 1 degree. The frequencies are expressed in terms of the factor, ka , for values of 0.5, 1, and 2. The radial distances from the cavity axis, in units of r/a , are: 1, 2, 5, 10, 20, 50, and 100. The displacement amplitude is a complex quantity, but only the magnitude of this quantity is used as output.

The fourth program, dispe, calculates the amplitude of the displacement field at a number of detector locations on the x-axis for a cavity located on the y-axis at several distances below the x-axis. The incident wave propagation vector may be directed at an angle with respect to the y-axis (i.e., vertical), and may vary from 0 to 180 degrees. The frequencies at which the displacement is calculated are expressed in terms of the factor, ka , and are 0.5, 1, and 2. The distances of the tunnel origin from the x- and y-axis origin are entered in terms of r/a and are 20, 40, 60, 80, and 100. The positions on the x-axis at which the displacement are calculated range from -50 to +50 meters in steps of 0.5 meters. The angle between the incident propagation vector and the y-axis may be either preset or calculated, according to which segments of the program code are commented out or not. If the preset version is chosen, then either backscatter or through transmission results may be produced. If the calculated version is chosen, the propagation vector is specified to lie on a line with a y-axis intercept of the cavity position and an x-axis intercept of -54 meters. This orientation of the incident wave relative to the cavity and the x-axis is similar to actual practice in seismic exploration where the location of the source point is at the end of the detector line. The displacement amplitude is a complex quantity, but only the magnitude of this quantity is used as output.

B. Line Source in a Half-Space

The numerical evaluation of the case of a line source in a half-space was incrementally developed beginning with the lossless unbounded medium case, followed by the addition of a half-space boundary, a surface layer, lossy media factors, and finally in a form capable of providing calculated results for any combination of these conditions. For example, by properly selecting the input parameters, the program can be made to provide results for, say, an unbounded lossy medium or a two-layered lossy medium, to cite two cases. The cases of a lossless and a lossy simple half-space and the case of a two-layered lossy half-space where the source is located in the lower layer and the detector is located either in the lower layer or at the upper boundary of the surface layer are considered in detail.

1. Overview of the Program

The program, synseis, presented in Appendix H, Section H.2.1, is the realization of the numerical solution of the equations for scattering of a cylindrical SH seismic wave from a cylindrical cavity derived in Section II. Since the direct and scattered signals received at the detector are decoupled in the approximate solution developed for deep cavities, the program solves for each signal component separately.

The basic solution method used for each signal component is the same. The time independent complex amplitude of the wave is found as a function of frequency and then inverse Fourier transformed into the time domain, where it represents the response generated by a delta function pulse emanating from the line source. This response contains time delay information related to the propagation of the wave from the source along the various propagation paths to the detector. This delta function response is then convolved with the source pulse waveform to obtain the composite signal at a given detector position. The same general method is applied for both the direct wave and the

scattered wave at each detector position, and the results are written out to a file.

Sample input and output files for program, synseis, are presented in Appendix H, Section H.2.1.

a. Direct Wave Calculation

The direct wave signal is calculated by the subroutines called `inc_pulse` and `inc_pulse2`. These two subroutines are essentially identical. The `inc_pulse` subroutine is written to provide a solution for the case for the source and detector located in the lower layer, and the `inc_pulse2` subroutine is written to solve the case for the source in the lower layer and the detector at the top of the surface layer. As a result, the description that follows is applicable to both subroutines.

The subroutine is given the source and detector positions as well as the values of the other parameters to be used in the calculation. For zero to n reflections from any layer interfaces that might be present, the time-independent direct wave amplitude along a given propagation path is calculated at 128 wavenumber values from 0 to 12.7 m^{-1} in steps of 0.1 m^{-1} . The time delay for the arrival of the wave is calculated from the geometry and the velocity in the medium and subtracted from the frequency domain signal by constant phase subtraction to prevent aliasing of the phase. A cosine window function is then applied to the frequency domain signal for a wavenumber range of 7.8 to 12.8 m^{-1} to prevent spurious ringing in the time domain signal. The frequency domain signal is then inverse Fourier transformed to obtain a 256-point time domain waveform. This waveform is then convolved in the time domain with the 256-point source pulse waveform to produce the signal present at the detection point. This signal is then added, often being offset by the initial time delay with respect to the total waveform, and the process is repeated for all reflections that are to be included in the calculation.

b. Scattered Wave Calculation

The scattered wave signal is calculated in the subroutines called `scat_pulse` and `scat_pulse2`. These two subroutines are essentially identical. The `scat_pulse` subroutine is written to provide a solution for the case for the source and detector located in the lower layer, and the `scat_pulse2` subroutine is written to solve the case for the source in the lower layer and the detector located at the top of the surface layer. As a result, the description that follows is applicable to both subroutines.

The subroutine is provided with the source, detector, and cavity locations as well as other relevant parameters. The algorithm makes repeated use of a number of Hankel function values, so these are precomputed. The routine then begins an iteration over the number of direct and reflected terms that are selected for the calculation. For a given propagation path, the time-independent scattered wave signal as a function of frequency is calculated at 128 points at wavenumber values from 0 to 12.7 m^{-1} . At each of these frequencies, a summation is performed to obtain the complex amplitude. A minimum of ten terms of summation are calculated, with up to fifty terms possible, until the accuracy of the sum in two consecutive terms is better

than the accuracy limit specified in the program, which is 1×10^{-4} . After the signal at all 128 frequencies have been calculated, the time delay is subtracted and the cosine window is applied as in the direct wave case. The frequency domain signal is then inverse Fourier transformed and convolved with the source pulse waveform. This result is then added, with its adjusted time offset, to the total waveform, and the process is repeated for all selected propagation paths.

2. Line Source in a Homogeneous Half-Space

For the case of a homogeneous half-space, the program is given an input file in which the density of layer 1 (the surface layer) is 0 and the number of reflections allowed is 1. The depths of the line source, the cylindrical cavity, and the detectors specified in the input file are referenced to the depth of the second layer. If desired, the depth of the first layer may be set to zero to simplify the task of depth calculation. If the surface layer depth is set to zero, care must be taken not to set the detector depth to exact zero as well, since this may cause the program to produce erroneous results.

a. Lossless Medium

To generate a solution for a lossless half-space medium, the attenuation cutoff frequency for the second layer should be set to a very large value, say 1.0×10^{30} . This will prevent onset of attenuation and dispersive effects in the practical range of seismic range frequency. The quality factor for the second layer may also be set to a high value, if desired, to suppress any dispersive effects in case the cutoff frequency was not set high enough.

b. Lossy Medium

To obtain a solution for a lossy homogeneous half-space, the cutoff frequency and quality factor should be set so as to simulate the ground conditions desired. It should be kept in mind that the cutoff frequency is given in terms of angular frequency, ω . To simulate a lossy medium over all frequencies of interest, set the cutoff frequency to a value less than the lowest frequency of interest. When the cutoff frequency is set to be smaller than the value of the frequency step, the attenuation condition defined by the Q factor applies to all frequencies. The quality factor should be set to larger values for less lossy media and to smaller values for more lossy media.

3. Line Source in a Two-Layer Lossy Half-Space

To simulate a line source in a two-layer lossy half-space, non-trivial values should be given to all parameters in the input file. If only one layer is to be lossy, the other layer may be given a large cutoff frequency or quality factor, as discussed earlier. The layer depth parameter should be non-zero in any case.

a. Source and Detector in Lower Layer

For the case in which the source and detectors are both located in the lower layer, it is only necessary to set the detector array

y-origin to a negative value greater than the layer depth. If the y-origin is less than the layer depth, unpredictable results will occur.

b. Source in Lower Layer and Detector in Surface Layer

For the case in which the detectors are located at the top of the surface layer, the y-origin should be set to zero. The present version of the program will not properly treat cases in which the detectors are located at other depths in the surface layer.

C. Graphing Programs

The graphics programs to produce output plots of the results from the above programs are presented in Appendix H, Sections H.3.1 and H.3.2. These programs are written in C language for ease of interfacing with the graphics package, Starbase, on the Hewlett-Packard 9000 model 520 computer equipped with the HP-UX operating system.

The graphics program for the display of synthetic seismograms, called vuseis, utilizes an input file to specify the presentation of the data. A sample input file is included in Appendix H, Section H.3.3, with a short explanation of the options available.

IV. MODEL CALCULATIONS AND RESULTS

A. Plane SH Waves Scattered from a Cylindrical Cavity in a Lossless Unbounded Medium

The theoretical analysis of plane SH-wave scattering from a cylindrical cavity representative of a horizontally oriented tunnel developed in Section II.B is used to provide preliminary insights into the problem of reflection seismic detection of such tunnel targets at depths of about 100 meters or more. In the results to follow, simple but useful and informative measures of the SH-wave scattering target strength and directional scattering signature of cylindrical cavities are presented for the conditions of geological host medium and tunnel size of primary interest. The numerical model is then used to simulate the steady-state detection responses that would be observed along a surface seismic reflection traverse and in a hole-to-hole seismic scan.

1. Energy Scattering Cross-Section

Figure IV-1 shows the geometry used to analyze the scattering of a plane SH wave incident on a cylindrical cavity in an unbounded medium. The total SH-wave displacement at measurement point, (x, y) , consists of the sum of the incident wave and the wave scattered from the cylindrical target.

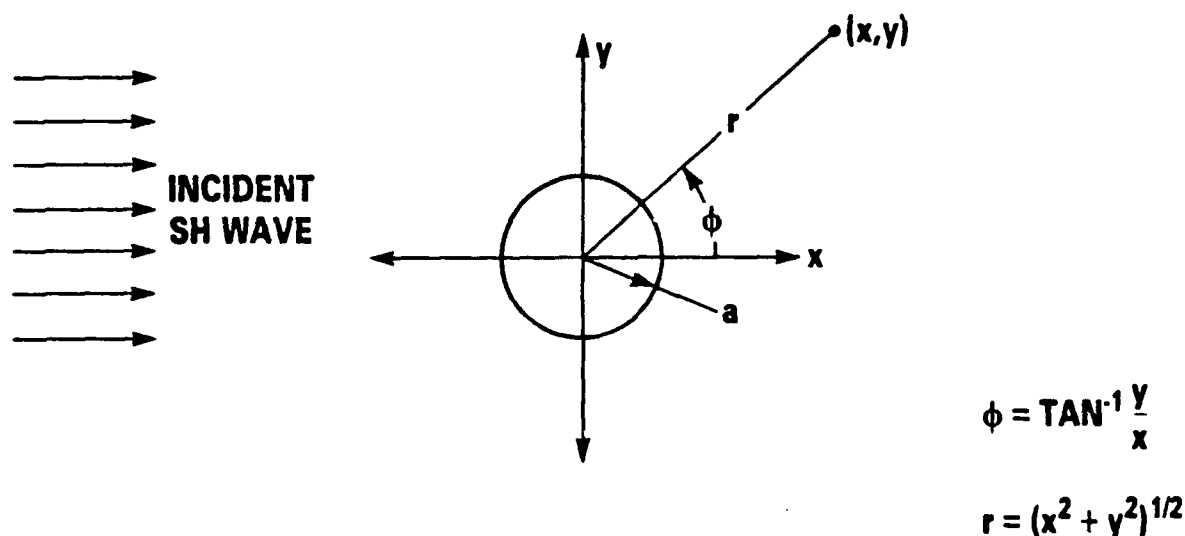


FIGURE IV-1. GEOMETRY OF PLANE SH-WAVE INCIDENT ON A CYLINDRICAL CAVITY IN AN UNBOUNDED MEDIUM

This total displacement is expressed by

$$u^t = e^{jkx} + \sum_{n=0}^{\infty} \left[\epsilon_n j^n \frac{J_n'(ka)}{H_n'(ka)} \right] H_n(kr) \cos(n\phi) \quad (IV-1)$$

The total elastic wave energy scattered by the cylindrical cavity can be computed from the second term of Equation (IV-1) by summing the products of each complex displacement term times its complex conjugate. This scattered SH-wave energy computed for $r=a$ may be divided by the physical (broadside) cross-sectional area of one unit length of the cavity to yield the normalized SH-wave energy scattering cross section for an incident plane SH wave. Thus, the SH-wave scattering efficiency may be expressed by the apparent energy scattering cross section of the cylinder target as

$$q_s = \frac{2}{ka} \left[A_0 A_0' + \frac{1}{2} \sum_{n=1}^{\infty} A_n A_n' \right] \quad (\text{IV-2})$$

where:

$$\epsilon_n = \begin{cases} 1; & \text{for } n = 1 \\ 2; & \text{for } n > 1 \end{cases}$$

$$k = \frac{\omega}{v_s}; \text{ and}$$

$$ka = \frac{2\pi a}{\lambda} = \frac{\pi D}{\lambda}; \text{ } D = \text{cavity diameter.}$$

Figure IV-2 shows the normalized SH wave energy scattering cross section for a 2-meter diameter cylindrical cavity in a medium having a shear-wave velocity of $v_s = 2,500$ m/s.

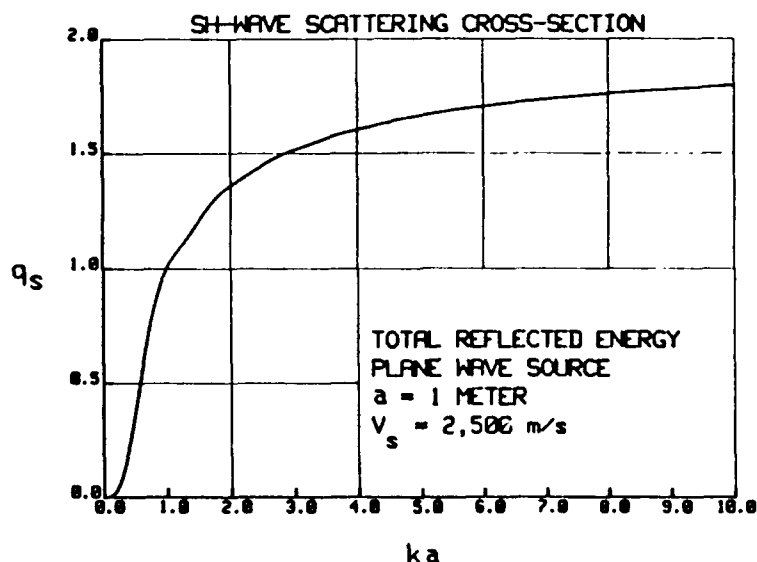


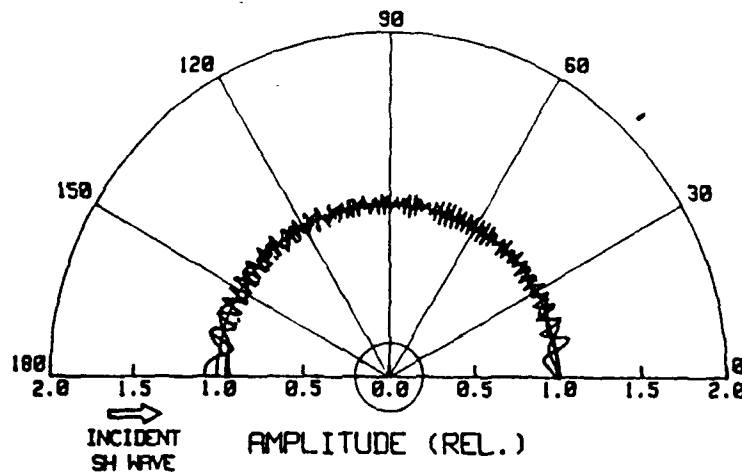
FIGURE IV-2. NORMALIZED ENERGY SCATTERING CROSS-SECTION OF A CYLINDRICAL CAVITY FOR AN INCIDENT PLANE SH WAVE

In Figure IV-1, the parameter ka is proportional to frequency and, for the value of $ka = \tau$, the frequency is 1,250 Hz and the shear wavelength is equal to the diameter of the cylindrical cavity. The normalized cross section in this case is approximately 1.55, a value which is about 55 percent larger than the area, D , corresponding to the per unit length cross-sectional area of the tunnel.

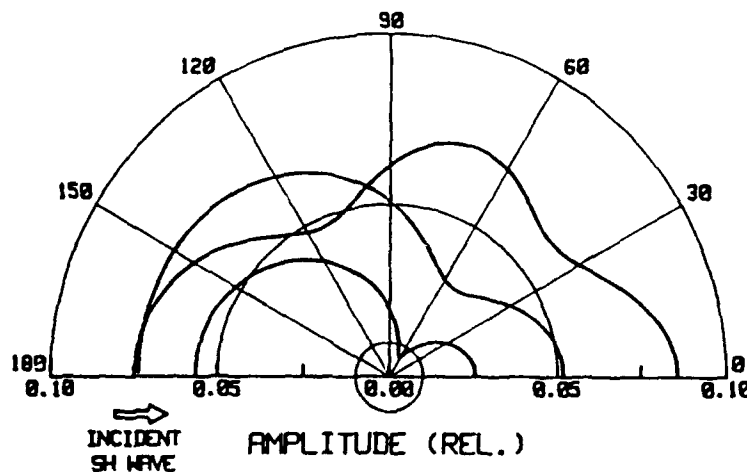
2. Polar Amplitude Scattering Patterns

Figure IV-3 shows the SH-wave amplitude scattered from a 2-meter diameter cylindrical cavity when the detector point, (x, y) is at a radius of 100 meters away from the cavity axis.

$r/a = 100.$	$ka = .5$ ———
$a = 1 \text{ METER}$	$ka = 1.0$ ———
$V_s = 2,500 \text{ m/s}$	$ka = 2.0$ ———



(a) Total SH-Wave Polar Amplitude



(b) SH-Wave Reflected Polar Amplitude Component

FIGURE IV-3. PLANE SH-WAVE POLAR AMPLITUDE SCATTERING FROM A CYLINDRICAL CAVITY

Figure IV-3(a) shows the total detected amplitude consisting of the combined incident and scattered waves as observed at a distance of 100 meters away from the tunnel. Figure IV-3(b) shows the scattered component only, illustrating the directional SH-wave scattering pattern of the cylindrical cavity and the fact that the scattered amplitude is in the range of 5-7.5 percent of the incident plane wave amplitude at point (x, y) for angular directions of $\phi = 180 \pm 30$ degrees. The values of ka illustrated in these figures correspond to frequencies of approximately 200 Hz, 400 Hz, and 800 Hz for the condition where $v_s = 2,500$ m/sec. Frequencies above 800 Hz will exhibit backscatter amplitudes up to about 10 percent of the incident wave amplitude.

3. Seismic Survey Traverse Simulations

Figure IV-4 illustrates the amplitude profile of the total plane wave scattered signal projected onto a representative seismic detector line traverse for several cavity depths. For the three SH-wave frequencies used in the analysis, the interference between the source wave and scattered wave component is apparent, with more spatial fluctuations in the near-source half of the detector spread. The directional scattering aspects of the cylindrical target are only slightly noticeable in the shallowest target depth case but can be anticipated to be more prevalent at higher frequencies.

These preliminary theoretical results show that the scattered amplitude of SH waves at distances up to 100 meters away from the cylindrical cavity have practical detection amplitudes. The magnitude of the scattered waves diminish as the inverse square root of the distance. For the typical shear wave velocity of $v_s = 2,500$ m/s, spectral components above about 400 Hz are strongly reflected. The polar amplitude scattering patterns indicate that the cylindrical cavity has a directivity which may serve as a useful means for identifying such scattering targets.

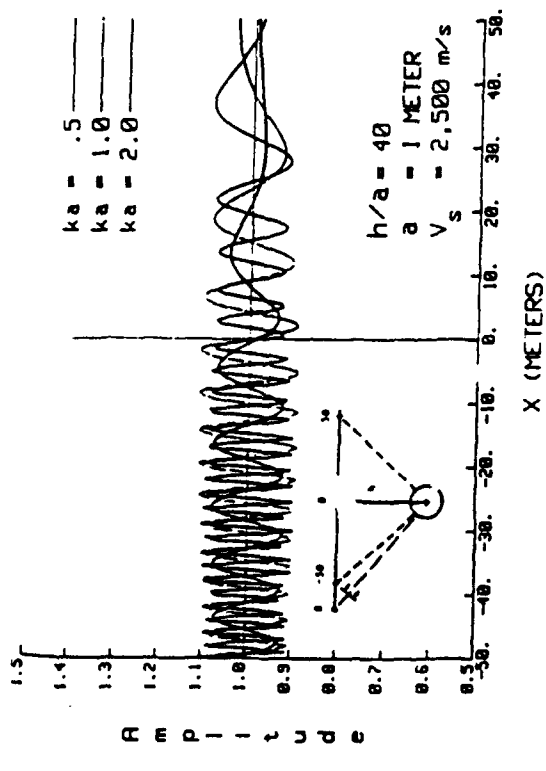
4. Hole-to-Hole SH-Wave Scattering Simulations

By using a different choice of the detector locations used in the seismic traverse simulations, the plane-wave analysis program may be used to simulate the steady-state response that would be observed in seismic scanning with the tunnel cavity oriented transversely between the boreholes. Figure IV-5 shows model calculations for horizontal ray path hole-to-hole SH-wave scattering from a 2-meter diameter tunnel as observed when the cavity is located 5, 10, 15, and 25 meters away (toward the source) from the borehole containing the detector.

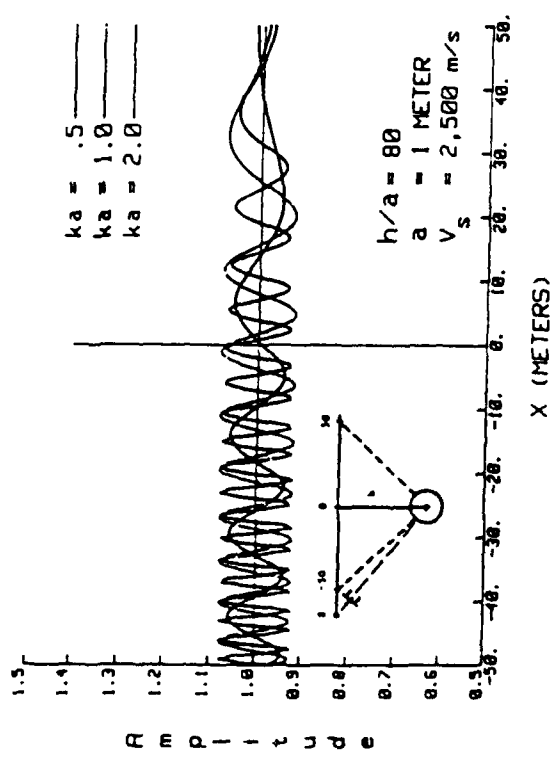
The scattered SH-wave displacement amplitude is symmetrical about the horizontal ray which passes through the center of the cylindrical cavity, and the scattered signal profile has the characteristic "W" shape which corresponds to the diffraction interference of waves scattered by a symmetrical obstacle. The frequency dependence of the forward-scattered SH waves for values of ka of 0.5, 1.0, and 2.0 are only very slightly stronger IV-4 for the reflection simulation case.

B. Synthetic Seismograms of SH Waves Scattered from a Cylindrical Tunnel in a Lossy Unbounded Medium

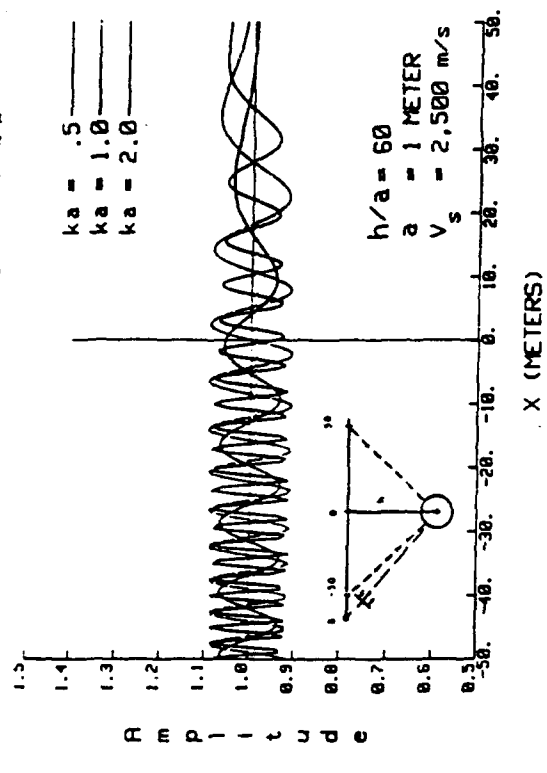
The numerical method developed in Section II.D has been implemented to compute synthetic seismograms of SH-wave scattering from a cylindrical



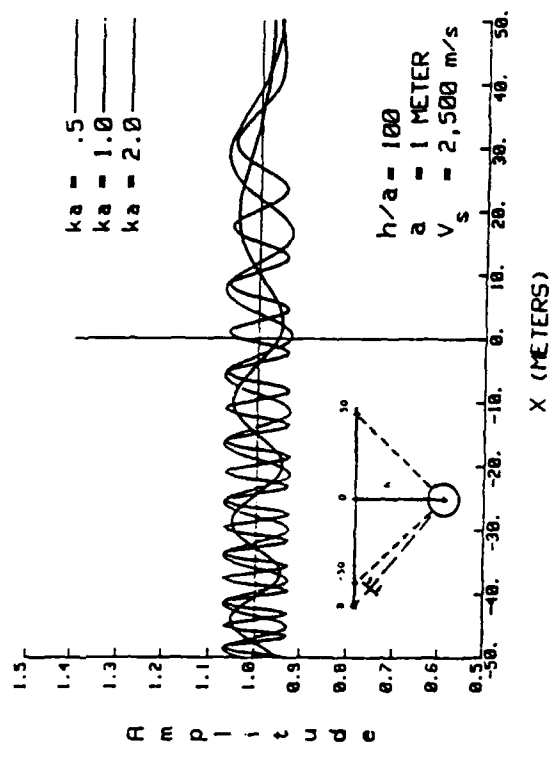
(a) Cavity Depth: 40 meters



(c) Cavity Depth: 80 meters

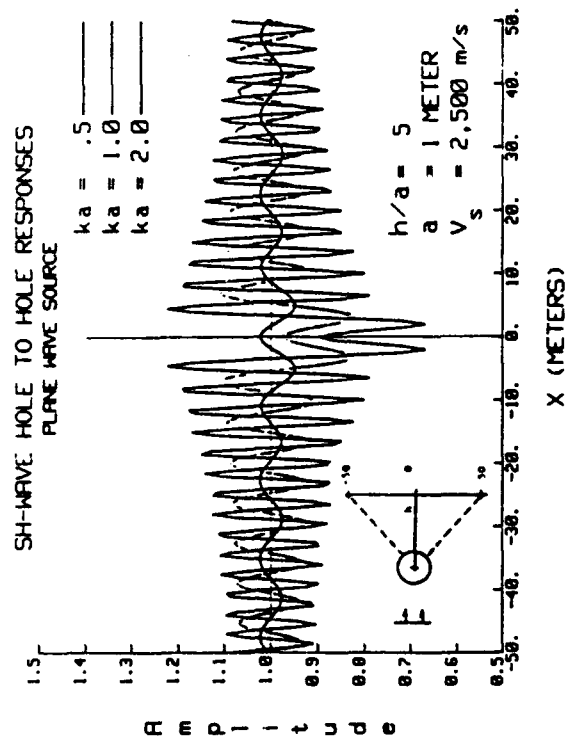


(b) Cavity Depth: 60 meters

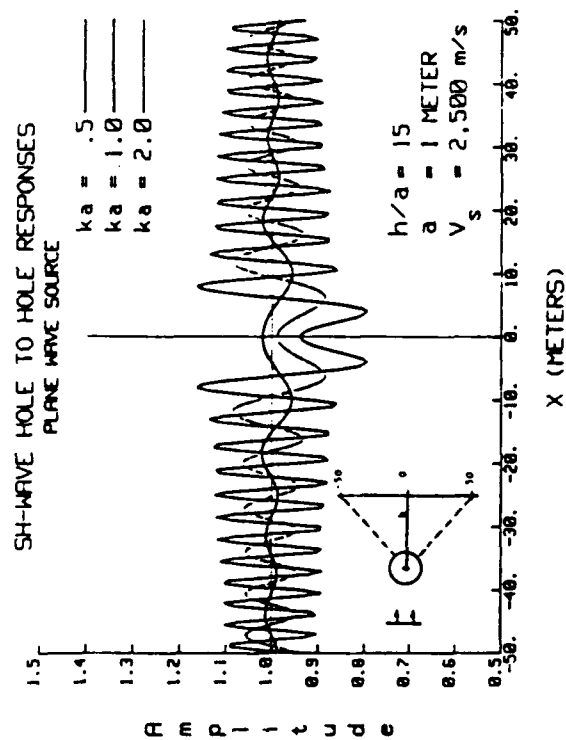


(d) Cavity Depth: 100 meters

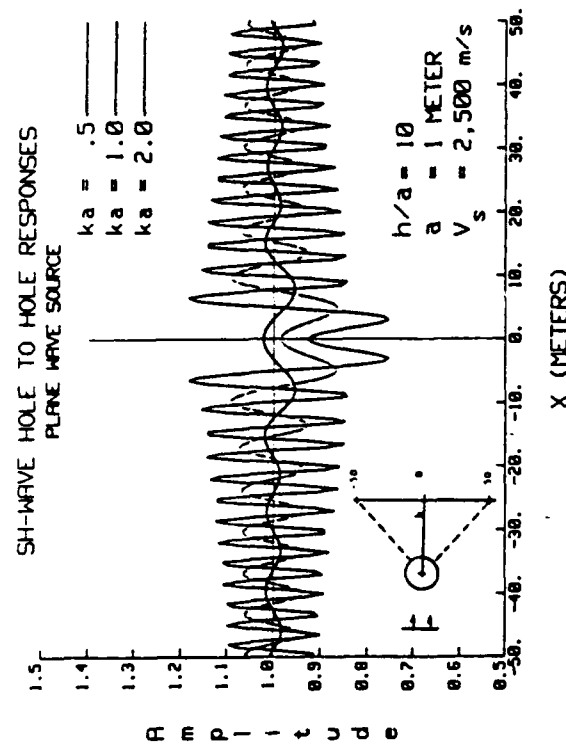
FIGURE IV-4. TOTAL PLANE SH-WAVE AMPLITUDE PROFILES ALONG A SIMULATED REFLECTION SEISMIC DETECTOR LINE



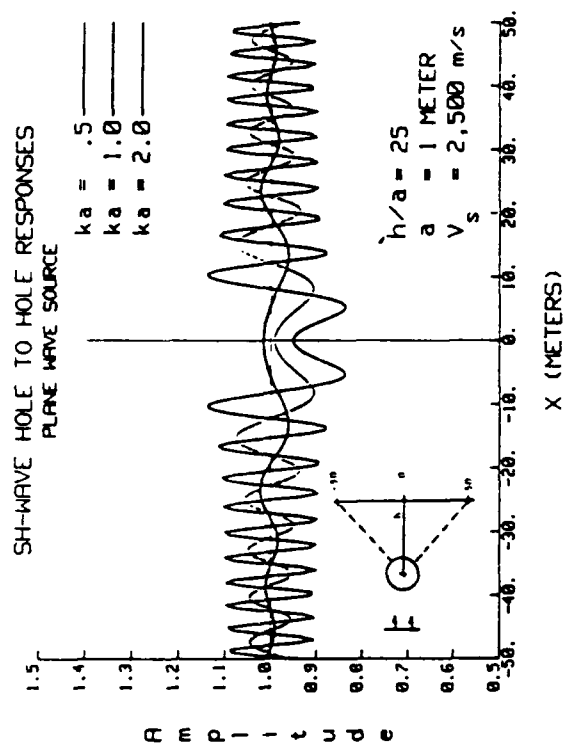
(a) Cavity Distance: 5 meters



(c) Cavity Distance: 15 meters



(b) Cavity Distance: 10 meters



(d) Cavity Distance: 25 meters

FIGURE IV-5. TOTAL PLANE SH-WAVE AMPLITUDE PROFILES BETWEEN BOREHOLES

cavity in a lossless medium and in a lossy medium for incident cylindrical SH-waves. The model geometry and the parameters of the medium are given in Figure IV-6. The characteristics of the SH-wave pulse signal transmitted by the line source are presented in Sections II.D.6 and II.F.6.

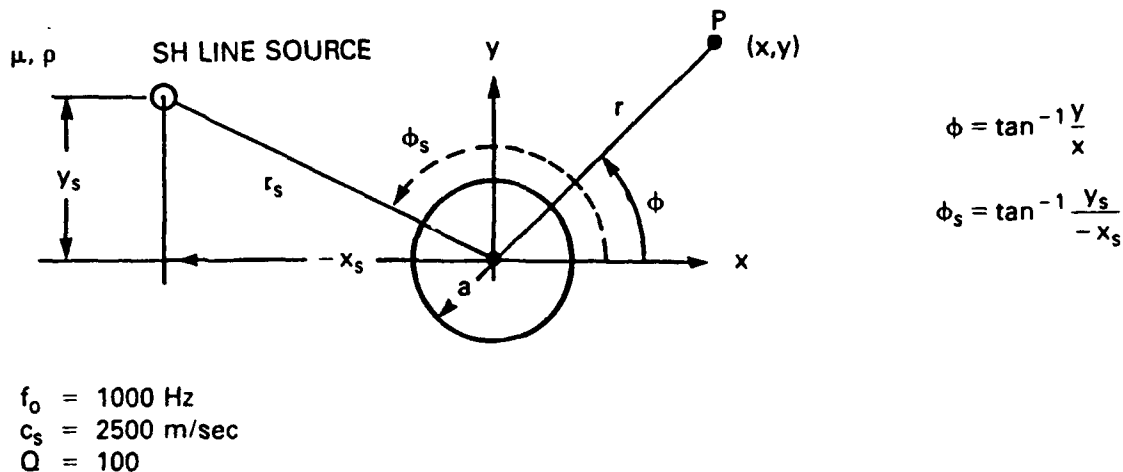


FIGURE IV-6. GEOMETRY OF CYLINDRICAL WAVE LINE SOURCE AND CYLINDRICAL CAVITY IN AN UNBOUNDED MEDIUM

Figures IV-7 through IV-13 illustrate synthetic seismograms calculated for the SH-wave source and a 2-meter diameter cylindrical cavity in a medium having a shear-wave velocity of $c_s = 2500 \text{ m/s}$. The SH-line source is specified to produce a pulse having a peak frequency $f_0 = 1000 \text{ Hz}$ and is located at the source position $(-52\text{m}, 0)$. The applied SH-wave pulse signal given by Equation (63) and its frequency spectrum given by Equation (64) are illustrated in Figure IV-14 (a) and (b), respectively. The seismic detector line, having detector spacings of 2 m, is transverse to the axis of the cylindrical cavity. The synthetic seismograms were calculated for both a perfectly elastic medium and a lossy medium. The seismograms associated with the lossy medium were computed for a shear-wave quality factor of $Q = 100$, which corresponds to a spatial attenuation rate of 0.25 dB/wavelength.

Figure IV-7 shows a synthetic seismogram containing the direct SH wave and the scattered SH wave from a tunnel target located at a depth of 50 m in a lossless medium. As expected, the time of arrivals and waveforms associated with the direct-traveling SH wave are detected first, and the scattered SH waves are detected later in the time section. The tunnel target reflections form a pattern having a hyperbolic shape which is characteristic of reflections from the localized air-filled tunnel target.

Figures IV-8 and IV-9 show only the direct-traveling SH-wave seismic pulses radiated by the SH-line source in a lossless and in a lossy medium, respectively. These results indicate the degree to which the amplitudes of the SH-wave pulses are reduced by a medium having an attenuation rate of 0.25 dB per wavelength.

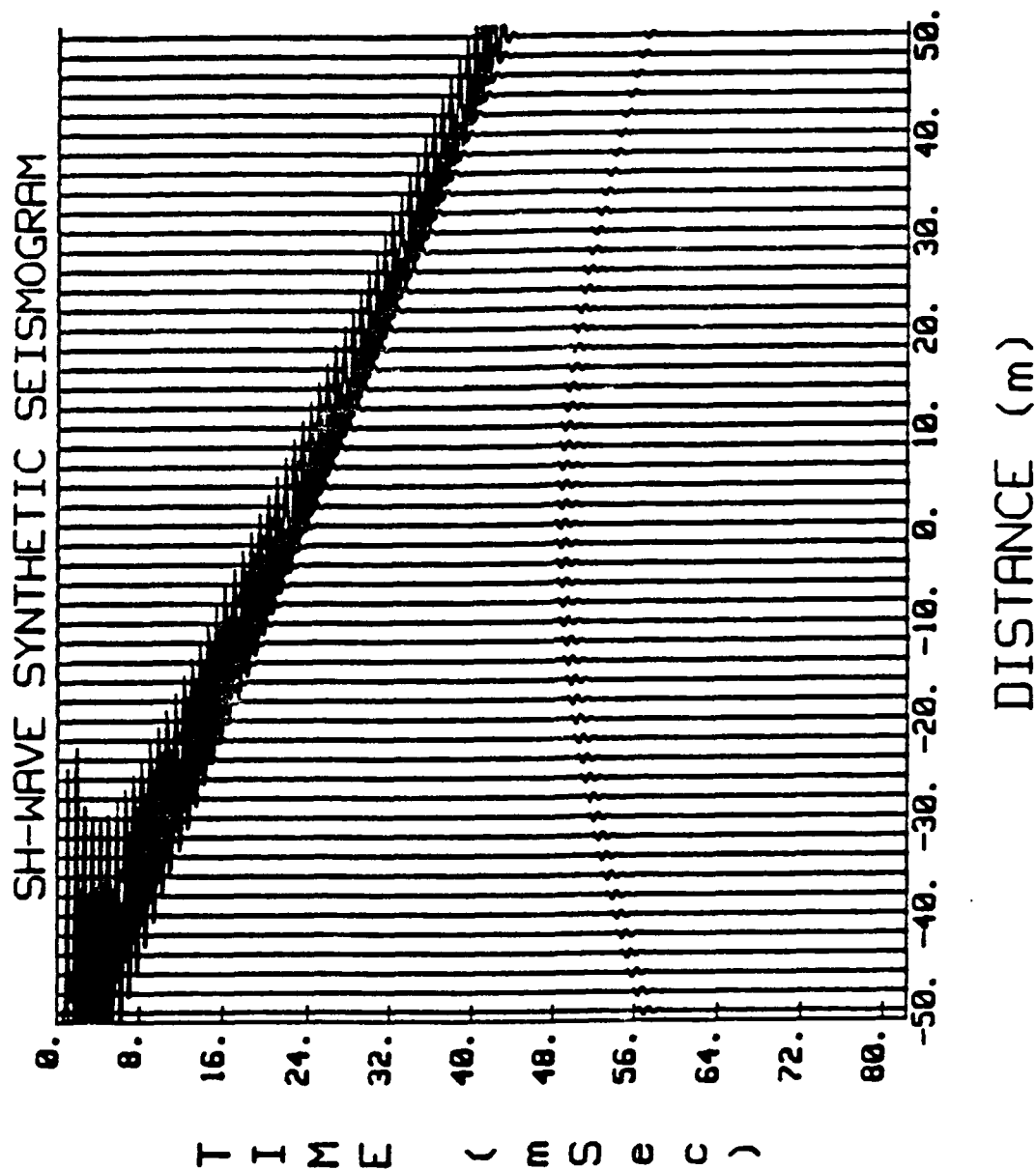


FIGURE IV-7. SYNTHETIC SEISMOGRAM OF THE COMBINED DIRECT AND REFLECTED SH-WAVE PARTICLE DISPLACEMENT FOR A 2-m DIAMETER CYLINDRICAL CAVITY AND AN SH-LINE SOURCE IN A LOSSLESS MEDIUM HAVING AN SH VELOCITY OF 2,500 m/s. THE CAVITY IS LOCATED AT A DEPTH OF 50 m BELOW THE SURFACE, AND THE SH-LINE SOURCE IS LOCATED AT THE POSITION (-52 m, 0). THE TRACES CORRESPOND TO THE OUTPUTS OF DETECTORS SPACED 2 m APART.

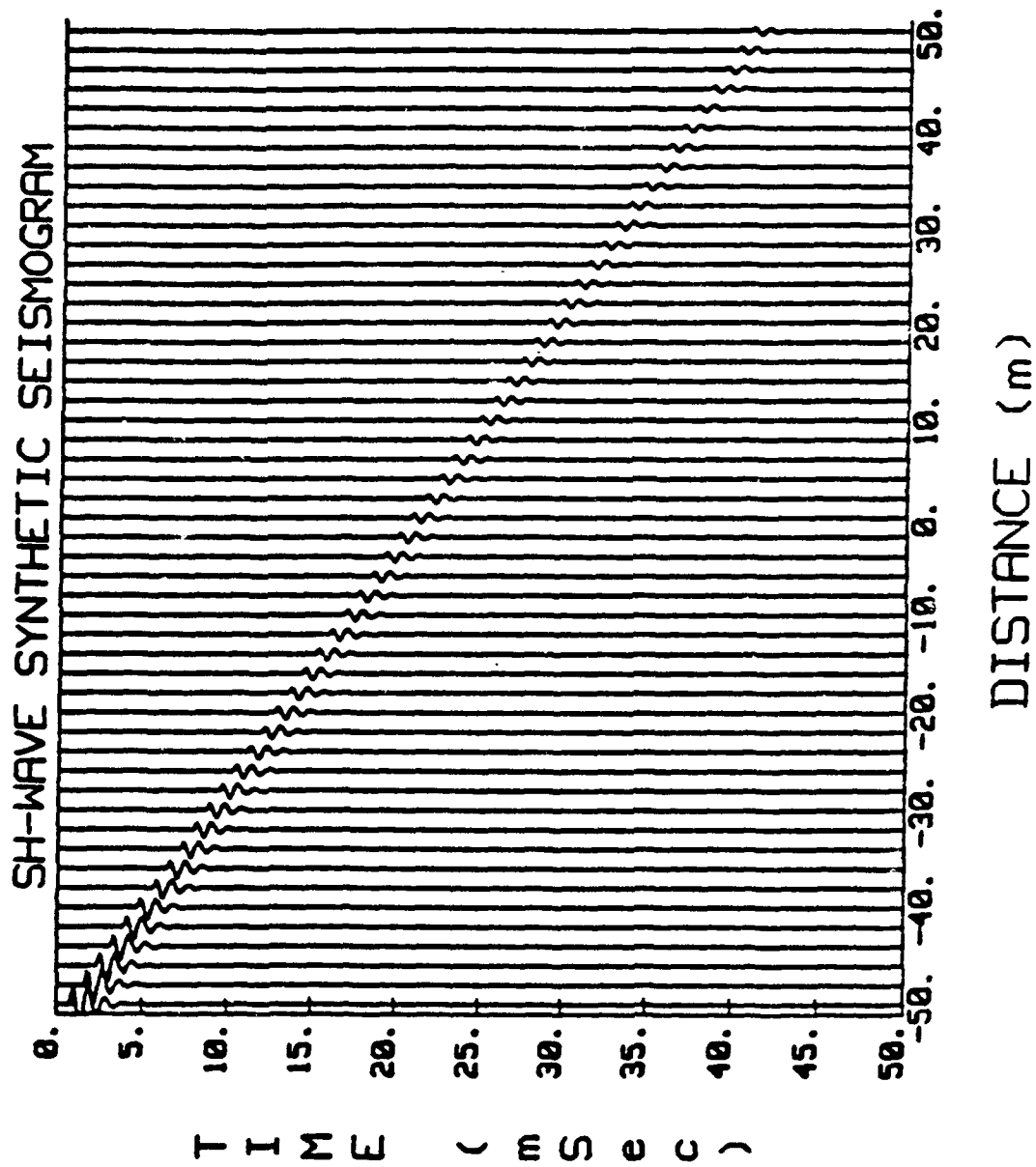


FIGURE IV-8. SYNTHETIC SEISMOGRAM OF DIRECT-TRAVELING SH-WAVES ONLY FROM AN SH-LINE SOURCE LOCATED IN A LOSSLESS MEDIUM AT THE SOURCE POSITION (-52 m, 0). THE SH-WAVE VELOCITY IN THE MEDIUM IS 2,500 m/s, AND THE DETECTOR SPACING IS 2 m. THE AMPLITUDE PLOTTING SCALE USED IN THESE TRACES IS REDUCED BY A FACTOR OF 12.5 FROM THAT IN FIGURE IV-7.

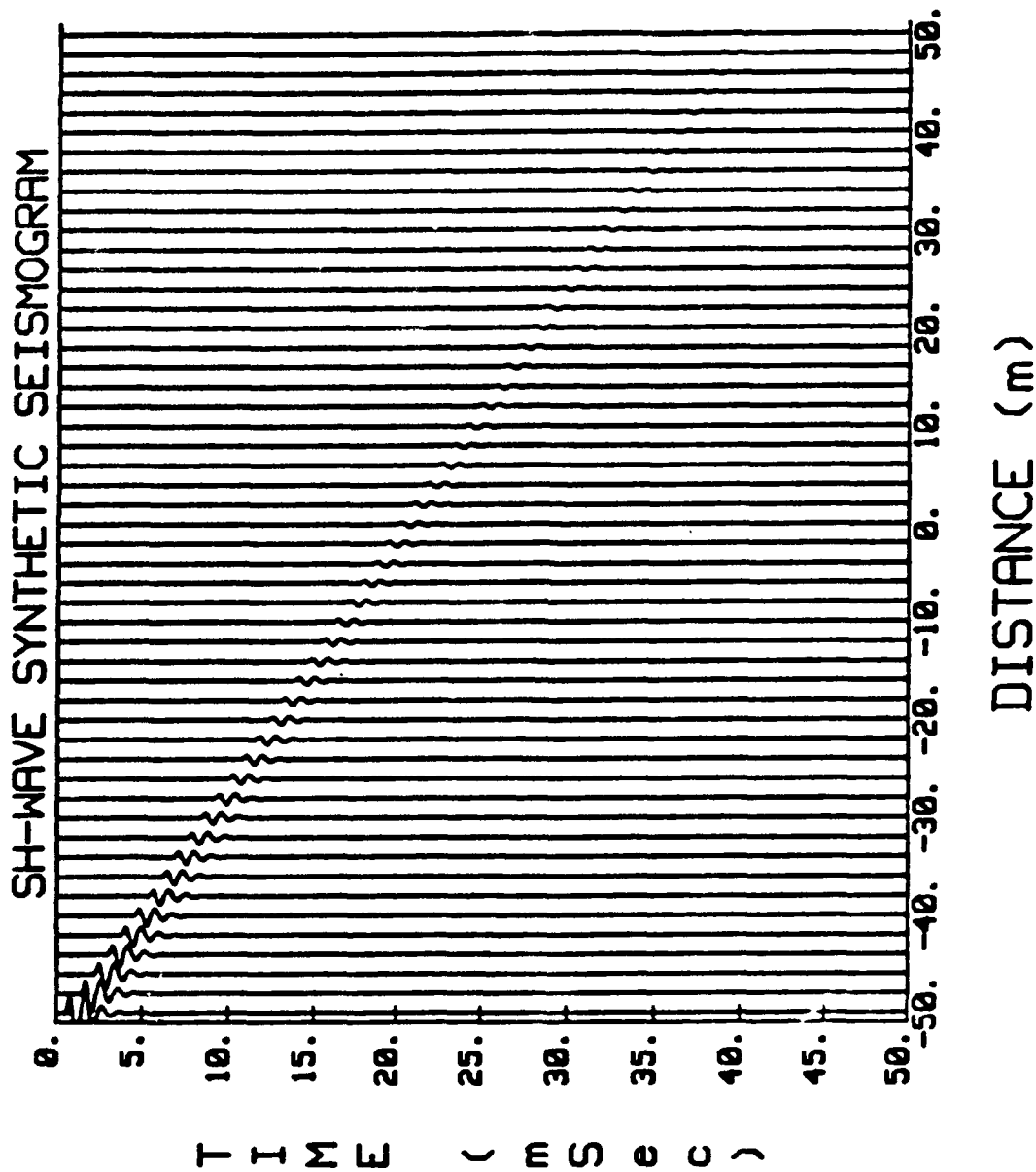


FIGURE IV-9. SYNTHETIC SEISMOGRAM OF DIRECT-TRAVELING SH-WAVES FROM AN SH-LINE SOURCE LOCATED IN A LOSSY MEDIUM AT THE SOURCE POSITION (-52 m, 0). THE SH-WAVE VELOCITY AND THE QUALITY FACTOR IN THE MEDIUM ARE $c = 2,500$ m/s AND $Q = 100$, RESPECTIVELY. THE DETECTOR SPACING IS 2 m. THE AMPLITUDE PLOTTING SCALE USED IN THESE TRACES IS THE SAME AS THAT IN FIGURE IV-8.

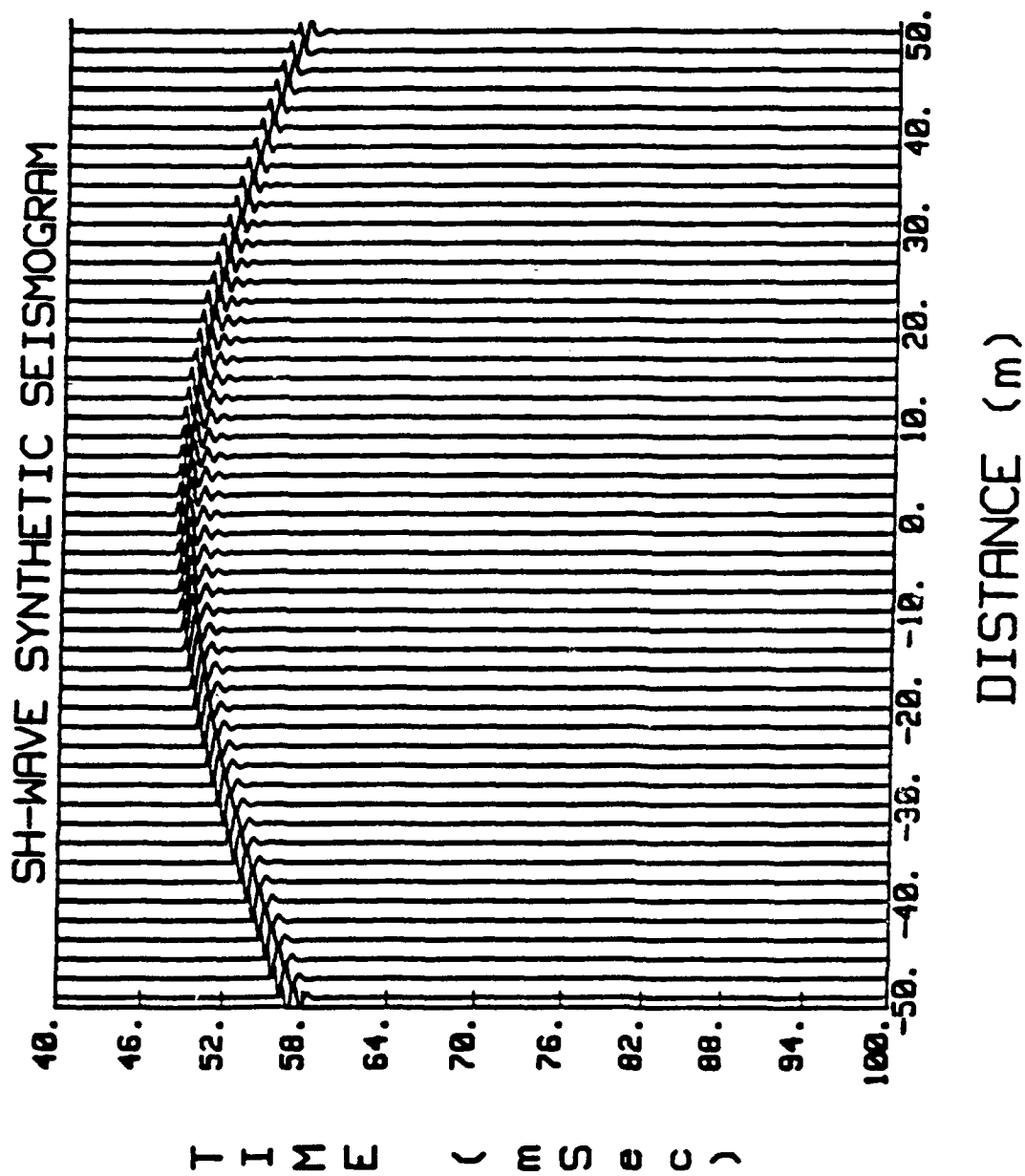
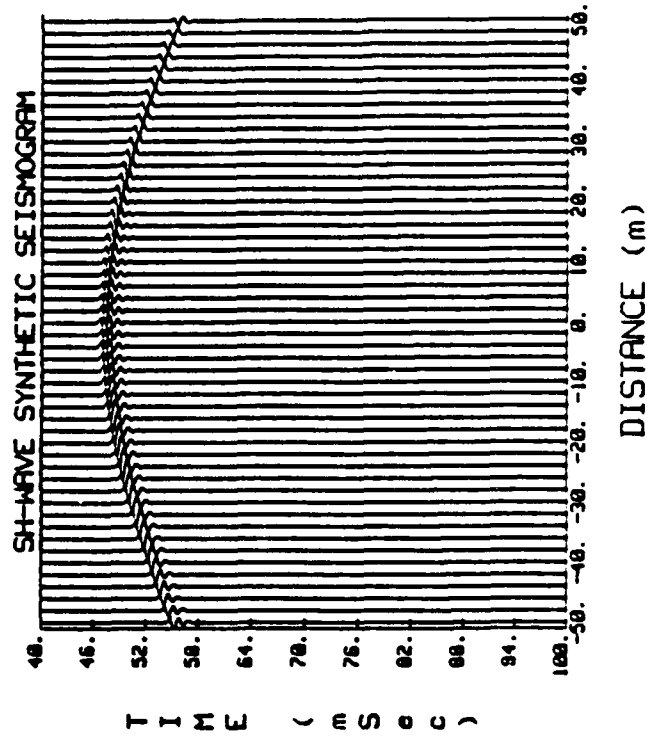
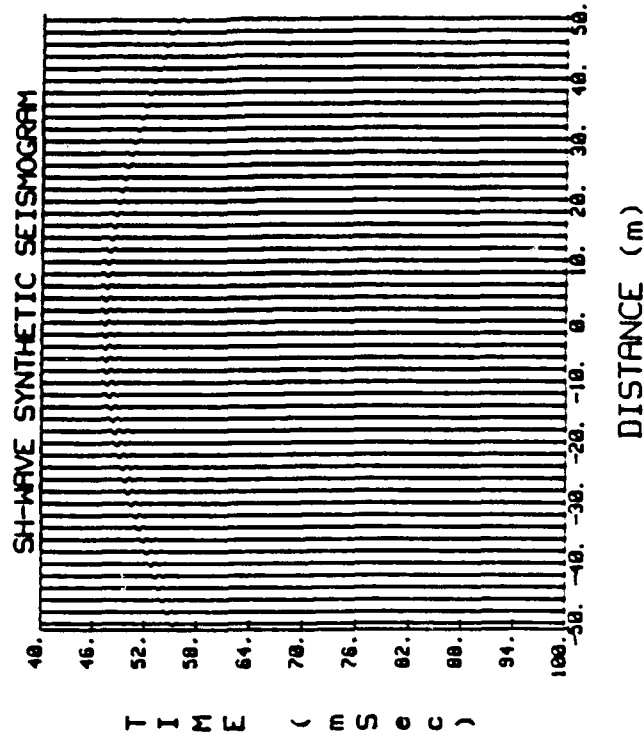


FIGURE IV-10. SYNTHETIC SEISMOGRAM OF SCATTERED SH-WAVES ONLY FROM A 2-m DIAMETER CYLINDRICAL CAVITY LOCATED IN A LOSSLESS MEDIUM AT A DEPTH OF 50 m. THE SH-WAVE VELOCITY IS 2,500 m/s. THE DETECTOR SPACING IS 2 m. THE AMPLITUDE PLOTTING SCALE USED IN THESE TRACES IS INCREASED BY A FACTOR OF FOUR ABOVE THAT IN FIGURE IV-7.



(a) Lossless Medium. The amplitude plotting scale is the same as in Figure IV-10.



(b) Lossy Medium. The amplitude plotting scale is increased by a factor of four above that in Figure IV-10.

FIGURE IV-11. SYNTHETIC SEISMOGRAMS OF SCATTERED SH-WAVES ONLY FROM A 2-m DIAMETER CYLINDRICAL CAVITY LOCATED IN A LOSSY MEDIUM AT A DEPTH OF 50 m. THE SH-WAVE VELOCITY AND THE QUALITY FACTOR OF THE MEDIUM ARE $c = 2,500$ m/s AND $Q = 100$, RESPECTIVELY. THE DETECTOR SPACING IS 2 m.

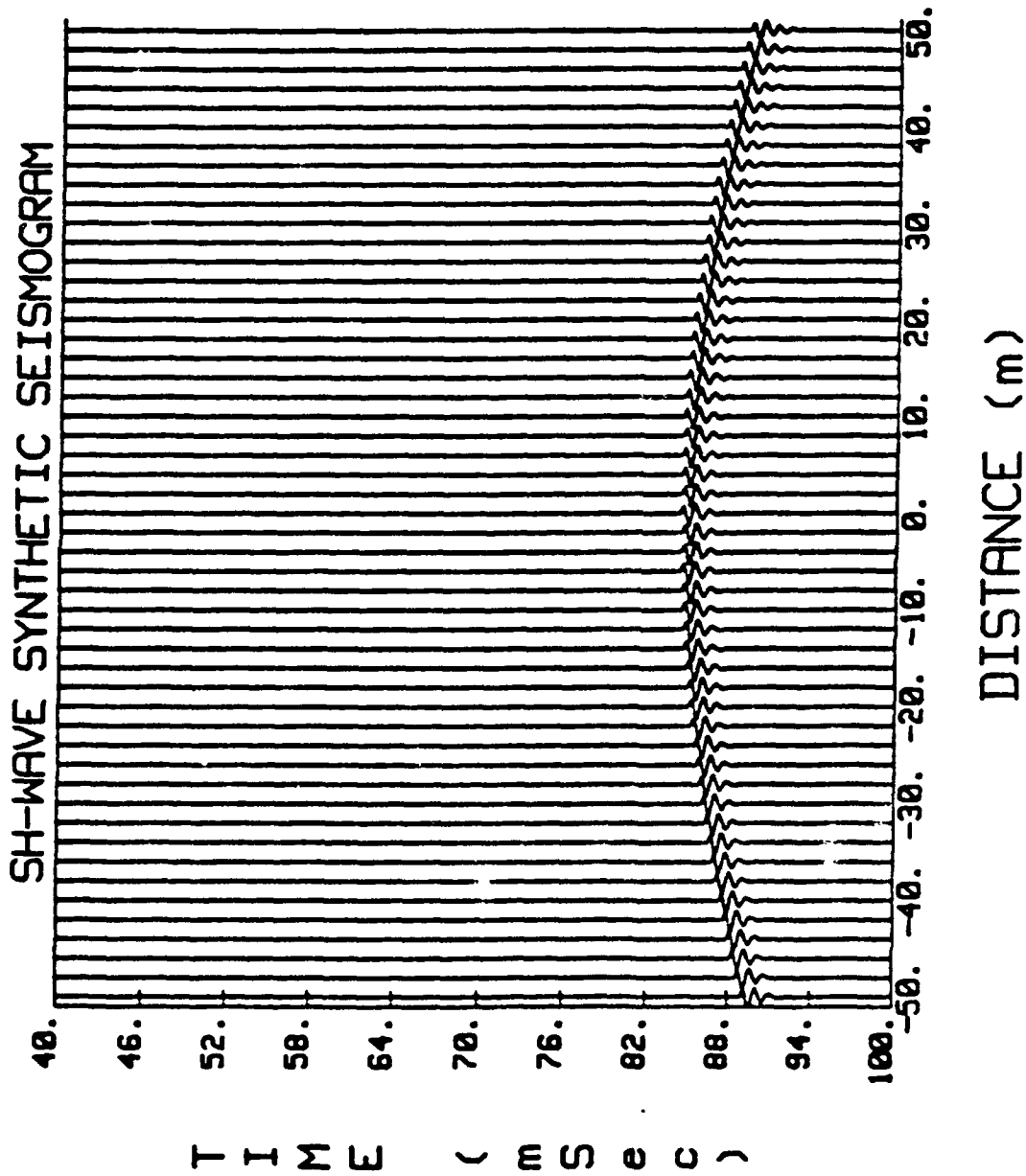
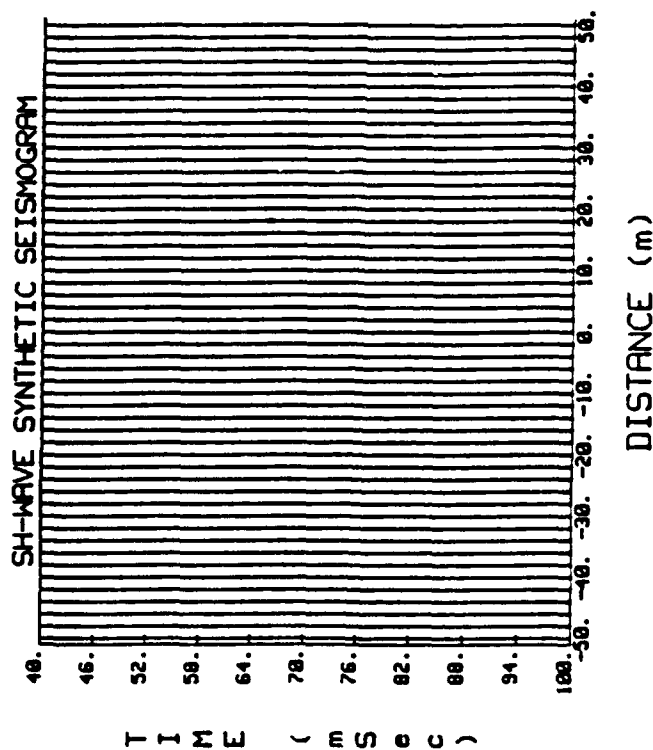
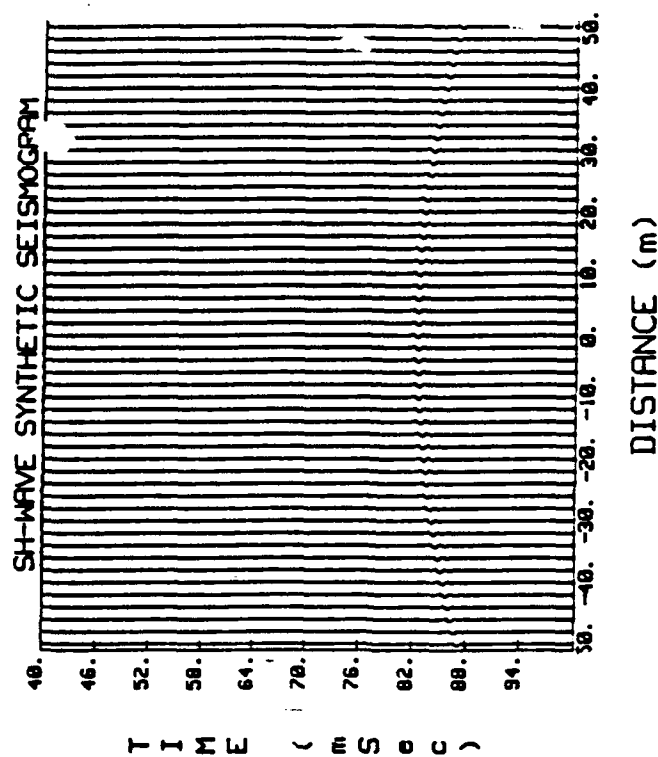


FIGURE IV-12. SYNTHETIC SEISMOGRAM OF SCATTERED SH-WAVES ONLY FROM A 2-m DIAMETER CYLINDRICAL CAVITY LOCATED IN A LOSSLESS MEDIUM AT A DEPTH OF 100 m. THE SH-WAVE VELOCITY IN THE MEDIUM IS 2,500 m/s, AND THE DETECTOR SPACING IS 2 m. THE AMPLITUDE PLOTTING SCALE IS THE SAME AS IN FIGURE IV-10.

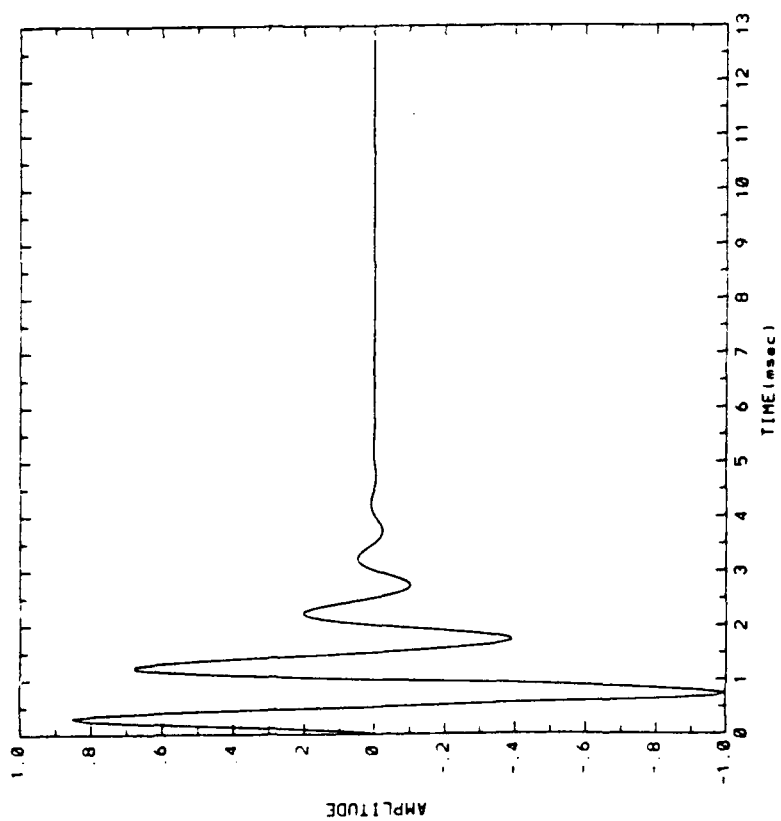


(a) The amplitude plotting scale is the same as in Figure IV-12.

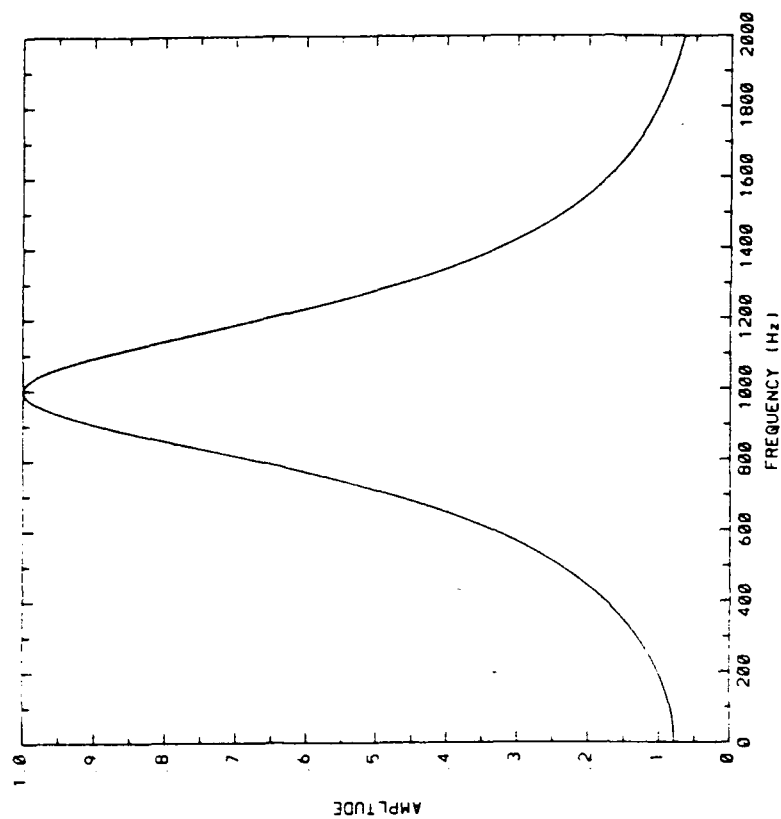


(b) The amplitude plotting scale is increased by a factor of four above that in Figure IV-12.

FIGURE IV-13. SYNTHETIC SEISMOGRAMS OF SCATTERED SH-WAVES ONLY FROM A 2-m DIAMETER CYLINDRICAL CAVITY LOCATED IN A LOSSY MEDIUM AT A DEPTH OF 100 m. THE SH-WAVE VELOCITY AND THE QUALITY FACTOR OF THE MEDIUM ARE $c = 2,500$ m/s AND $Q = 100$, RESPECTIVELY. THE DETECTOR SPACING IS 2 m.



(a) SH-wave Pulse Signal



(b) Frequency Spectrum

FIGURE IV-14. THE SH-WAVE PULSE SOURCE SIGNAL AND ITS FREQUENCY SPECTRUM

Figures IV-10, IV-11(a), and IV-11(b) show only the SH waves scattered from the cylindrical cavity located at a depth of 50 m in a lossless medium and in a lossy medium. These results show that the tunnel reflection signature in the lossy medium is significantly reduced with respect to that from a tunnel target in an ideal elastic medium. Figure IV-11(b) shows the hyperbolic reflected SH-wave pattern plotted with an increased scale factor of 800, which is about four times greater than the scale factor used to display the attenuated synthetic seismogram illustrated in Figure IV-11(a) (i.e., the effective increase in display sensitivity is a factor of 200).

Figures IV-12, IV-13(a), and IV-13(b) illustrate the synthetic seismograms of scattered SH-waves from a 2-m diameter cylindrical cavity located at a depth of 100 m. As expected, when the depth of the cavity is increased, the amplitude of scattered SH-wave reflections decrease because of the geometric spreading loss as well as because of the excess absorptive attenuation as shown in Figure IV-13(a). To adequately display the tunnel reflection signatures for these conditions, an effective scale factor of 200 relative to that in Figure IV-13(a) is used to show the synthetic seismogram for the 100-m deep tunnel in Figure IV-13(b).

C. Synthetic Seismograms of SH Waves Scattered from a Cylindrical Cavity in a Two-Layered Lossy Half-Space

The numerical method developed in Section II.D is used to compute synthetic seismograms of SH waves scattered from a cylindrical tunnel in a two-layered lossy half-space. These seismograms have been computed for the cases of a line of detectors in the bedrock and a line of detectors at the top of the surface layer. This model represents a systematic display of synthetic seismograms for several cases in which the surface-layer thickness, quality factor, and shear-wave velocity together with tunnel target depth and the detector location (either buried or surface) are independent parameters.

The model geometry is shown in Figure IV-15, and the various parameters of the calculated cases are listed in Table IV-1. All of the synthetic seismograms are computed for the SH-line source located at the position $[-52\text{m}, -(h+1)]$ and for a 2-m diameter cylindrical tunnel in a medium having a shear-wave velocity of $c_2 = 2500$ m/s. The seismic detector line having detector spacings of 2 m is transverse to the axis of the cylindrical cavity. The characteristics of the SH-line pulse signal transmitted by the line source and the number of detectors, nd , are the same as those used earlier in the unbounded medium case. Appendix G presents the practical case in which the ground overlying the tunnel target consists of a weathered surface which is typically more lossy than the deeper and more competent medium containing the tunnel cavity. The model calculations for this case are aimed at illustrating and comparing the tunnel detection results obtained when the detectors are buried (coupled in boreholes) at the depth of the competent (lower loss) ground with those obtained when the detectors are coupled to the top of the less competent ground surface.

Tables IV-2, -3, and -4 summarize parameters used in the two-layer model calculations and identify the corresponding figure numbers of the respective synthetic seismograms illustrated in Appendix G. In the illustrations of Appendix G, the figures are subdivided in three parts identified as (a), (b), and (c). The illustrations identified by (a) show the total SH-wave particle

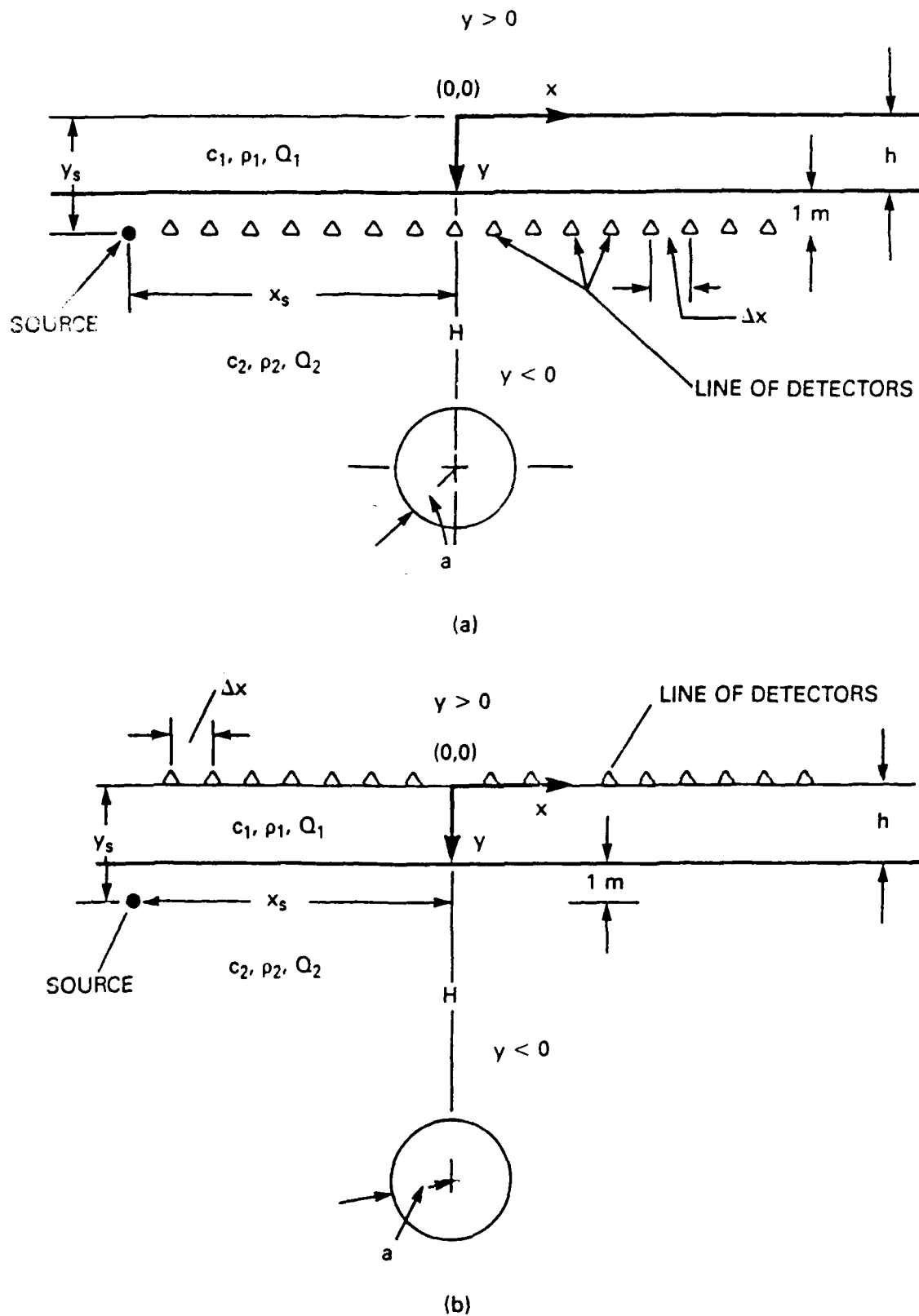


FIGURE IV-15. GEOMETRY AND MODEL PARAMETERS FOR AN SH-LINE SOURCE AND A CYLINDRICAL CAVITY IN A TWO-LAYER HALF-SPACE

- (a) Detectors in the bedrock
- (b) Detectors at the surface

TABLE IV-1
LIST OF PARAMETERS FOR THE TWO-LAYER LOSS HALF-SPACE
(Ref. Figure IV-14)

(x_s, y_s)	= SH-line source coordinates
(x, y)	= Detector coordinates
Δx	= Detector spacing
n_d	= Number of detectors
$2a$	= Cavity diameter
H	= Cavity depth
h	= Layer thickness
N	= Number of reflections
c_1	= Surface layer SH-wave velocity
c_2	= Bedrock SH-wave velocity
ρ_1	= Surface layer density
ρ_2	= Bedrock density
Q_1	= Surface layer quality factor
Q_2	= Bedrock quality factor

TABLE IV-2

TWO-LAYER MODEL WITH DETECTORS IN THE BEDROCK

$$y_s = y = -(h+1) \text{ m}$$

Tunnel Depth (H) = 50 m

<u>Figure Numbers</u>	<u>h</u> <u>(m)</u>	<u>Q₁</u>	<u>Q₂</u>	<u>c₁</u> <u>(m/sec)</u>	<u>c₂</u> <u>(m/sec)</u>	<u>ρ₁</u> <u>(kg/m³)</u>	<u>ρ₂</u> <u>(kg/m³)</u>
(G-1a, G-1b, G-1c)	5	50	100	200	2500	1500	2700
(G-2a, G-2b, G-2c)	10	50	100	200	2500	1500	2700
(G-3a, G-3b, G-3c)	5	10	100	200	2500	1500	2700
(G-4a, G-4b, G-4c)	10	10	100	200	2500	1500	2700

Tunnel Depth (H) = 100 m

(G-5a, G-5b, G-5c)	5	50	100	200	2500	1500	2700
(G-6a, G-6b, G-6c)	10	50	100	200	2500	1500	2700
(G-7a, G-7b, G-7c)	5	10	100	200	2500	1500	2700
(G-8a, G-8b, G-8c)	10	10	100	200	2500	1500	2700

$$x_s = -52 \text{ m}, \Delta x = 2 \text{ m}, nd = 51, 2a = 2 \text{ m}, \text{ and } N = 3.$$

TABLE IV-3

TWO-LAYER MODEL WITH DETECTORS AT SURFACE

$$y_s = -(h+1) \text{ m}$$

$$y = 0$$

Tunnel Depth (H) = 50 m

<u>Figure Numbers</u>	<u>h</u> <u>(m)</u>	<u>Q₁</u>	<u>Q₂</u>	<u>c₁</u> <u>(m/sec)</u>	<u>c₂</u> <u>(m/sec)</u>	<u>ρ₁</u> <u>(kg/m³)</u>	<u>ρ₂</u> <u>(kg/m³)</u>
(G-9a, G-9b, G-9c)	5	50	100	200	2500	1500	2700
(G-10a, G-10b, G-10c)	10	50	100	200	2500	1500	2700
(G-11a, G-11b, G-11c)	5	10	100	200	2500	1500	2700
(G-12a, G-12b, G-12c)	10	10	100	200	2500	1500	2700

Tunnel Depth (H) = 100 m

(G-13a, G-13b, G-13c)	5	50	100	200	2500	1500	2700
(G-14a, G-14b, G-14c)	10	50	100	200	2500	1500	2700
(G-15a, G-15b, G-15c)	5	10	100	200	2500	1500	2700
(G-16a, G-16b, G-16c)	10	10	100	200	2500	1500	2700

 $x_s = -52 \text{ m}, \Delta x = 2 \text{ m}, n_d = 51, 2a = 2 \text{ m}, \text{ and } N = 3.$

TABLE IV-4

TWO-LAYER MODEL SHOWING HIGHER ORDER REFLECTIONS IN THE SURFACE LAYER

$$y_s = -(h+1) \text{ m}$$

$$y = 0$$

$$H = 50 \text{ m}$$

Detectors in the Bedrock

Figure Numbers	N	h (m)	Q_1	Q_2	c_1 (m/sec)	c_2 (m/sec)	ρ_1 (kg/m ³)	ρ_2 (kg/m ³)
(G-17a, G-17b, G-17c)	0	5	50	100	500	2500	1500	2700
(G-18a, G-18b, G-18c)	1	5	50	100	500	2500	1500	2700
(G-19a, G-19b, G-19c)	2	5	50	100	500	2500	1500	2700
(G-20a, G-20b, G-20c)	3	5	50	100	500	2500	1500	2700

Detectors at Surface

(G-21a, G-21b, G-21c)	0	5	50	100	500	2500	1500	2700
(G-22a, G-22b, G-22c)	1	5	50	100	500	2500	1500	2700
(G-23a, G-23b, G-23c)	2	5	50	100	500	2500	1500	2700
(G-24a, G-24b, G-24c)	3	5	50	100	500	2500	1500	2700

$$x_s = -52 \text{ m}, \Delta x = 2 \text{ m}, n_d = 51, \text{ and } 2a = 2 \text{ m}.$$

motion seismograms plotted to the largest practical amplitude (effective scale factor of 200) in an effort to display the combined direct and scattered components of the detected signals. The illustrations identified by (b) show only the direct arrival SH-wave particle motion seismograms plotted to a scale which is one-half that of the illustrations identified by (a). The illustrations identified by (c) show only the scattered SH-wave particle motion seismograms plotted to a scale which is ten times that of the illustrations identified by (a).

Discussions are presented below based upon selected examples of the calculated model cases presented in Appendix G to evaluate the effects of attenuation, thickness, and SH-wave velocity in the surface layer and the location of the detectors on the tunnel detection response.

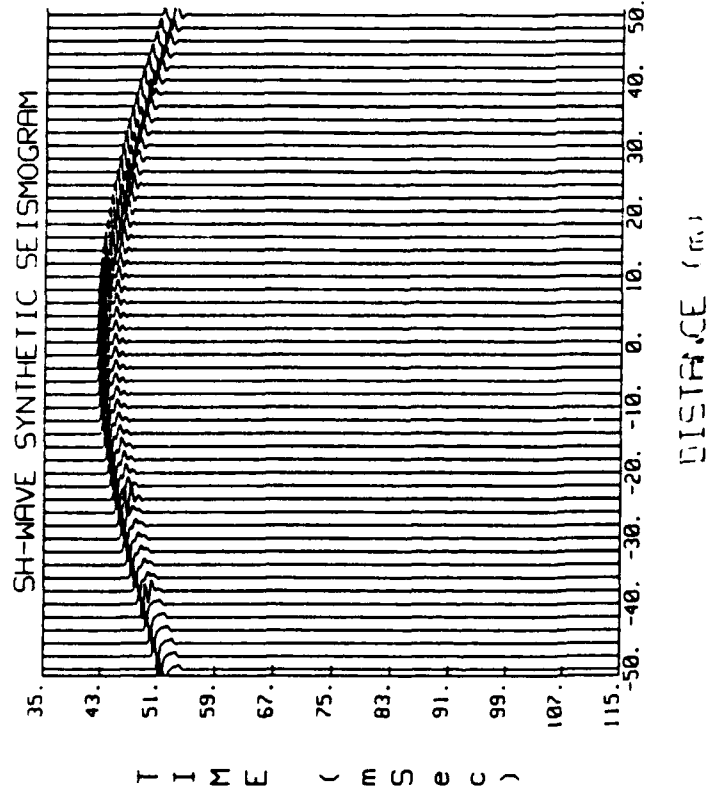
1. Effect of Surface Layer Attenuation

Examples of synthetic seismograms from Appendix G are discussed below to demonstrate the effects of surface layer attenuation on the detection of the tunnel cavity. For this purpose, the SH-wave line source is in the bedrock layer and the tunnel cavity depth is selected to be $H = 50$ m and the surface layer thickness is selected to be 5 m. The layer attenuation parameters to be compared correspond to quality factors of $Q_1 = 50$ (0.5 dB/wavelength) and $Q_1 = 10$ (2.5 dB/wavelength), and the detectors are located in the top of the bedrock layer (Figures G-1 and G-3 in Appendix G) and at the top of the surface layer (Figures G-9 and G-11 in Appendix G).

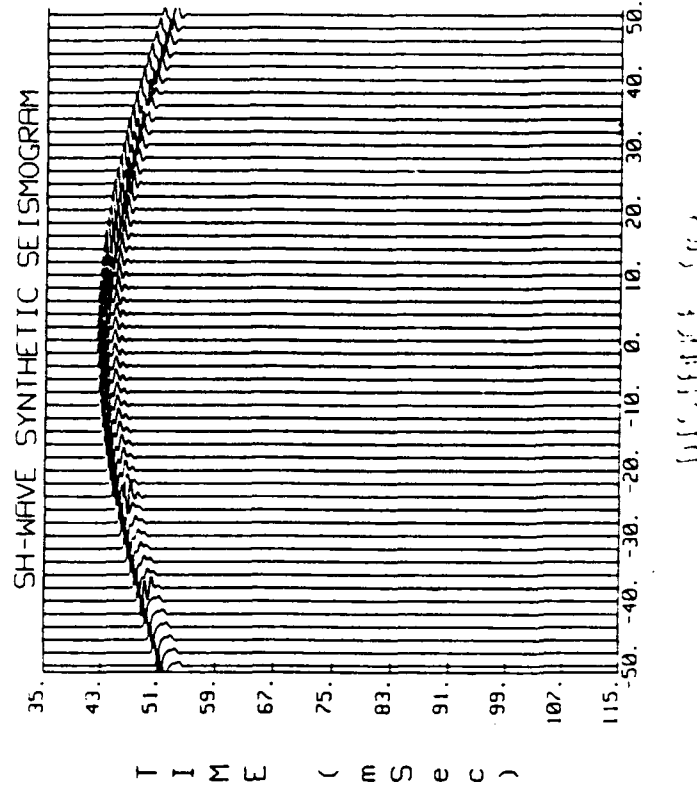
Figures IV-16 and IV-17 show the comparative effects of surface layer attenuation on the tunnel-scattered SH waves. In Figure IV-16, where the SH-wave source and detectors are in the competent bedrock layer, the tunnel detection responses are not significantly affected by the attenuation quality of the surface layer. In comparison, the responses in Figure IV-17, where the source is in the bedrock layer but the detectors are at the top of the surface layer, show a very substantial attenuation of the scattered SH-waves from the tunnel when the quality factor of the surface layer is changed from 50 to 10. The detected waveforms observed at the top of the surface layer also lack the finer details contained in the waveforms detected below the surface layer, especially in the more realistic $Q_1 = 10$ case. Figures G-5 and G-7, G-13 and G-15 in Appendix G may be used to compare corresponding surface layer attenuation effects on SH waves scattered from a tunnel target at 100 m below surface.

2. Effect of Surface Layer Thickness

Examples of synthetic seismograms from Appendix G are discussed below to demonstrate the effects of surface layer thickness on the detection of the tunnel cavity. For this purpose, the SH-wave line source is in the bedrock layer and the tunnel cavity depth is selected to be $H = 50$ m and the surface layer quality factor is selected to be $Q_1 = 50$. The surface layer thicknesses to be compared are $h = 5$ m and $h = 10$ m, and the detectors are located in the top of the bedrock layer (Figures G-1 and G-2 in Appendix G) and at the top of the surface layer (Figures G-9 and G-10 in Appendix G).

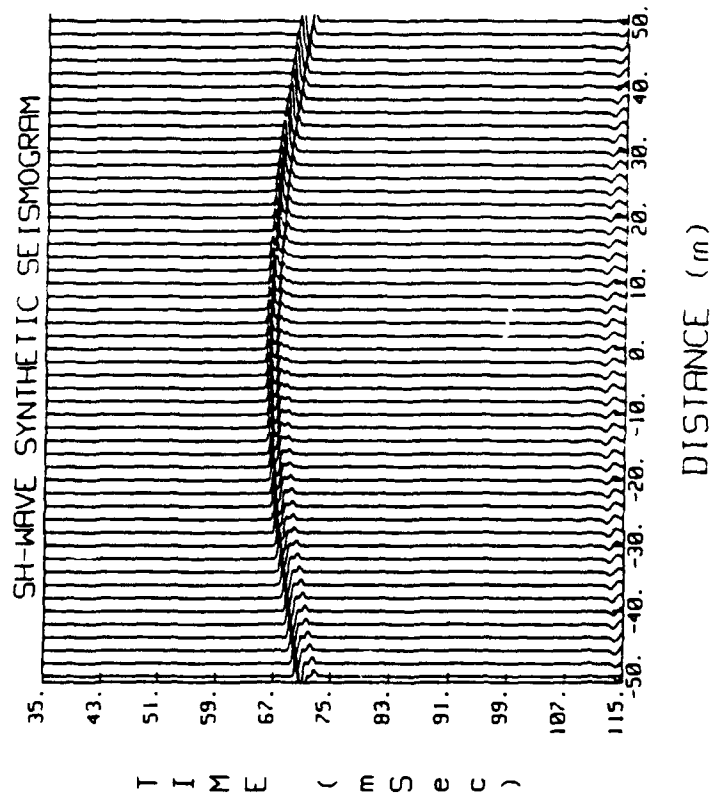


(a) The quality factor of the surface layer is $Q_1 = 50$.

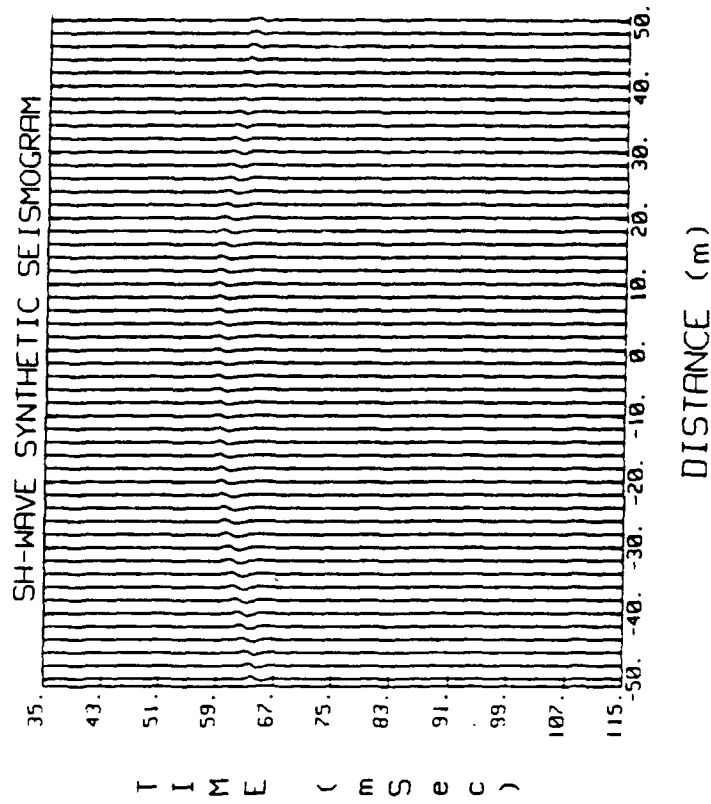


(b) The quality factor of the surface layer is $Q_1 = 10$.

FIGURE IV-16. SYNTHETIC SEISMOGRAMS OF SCATTERED SH-WAVES ONLY FROM A 2-m DIAMETER CYLINDRICAL CAVITY LOCATED IN A TWO-LAYER LOSSY HALF-SPACE AT A DEPTH OF 50 m. THE SURFACE LAYER THICKNESS IS 5 m. THE CONSTITUTIVE PARAMETERS OF THE SURFACE LAYER AND THE BEDROCK ARE $c_1 = 200$ m/sec, $\rho_1 = 1500$ kg/m³, $c_2 = 2500$ m/sec, AND $\rho_2 = 2700$ kg/m³. THE QUALITY FACTOR OF THE BEDROCK IS $Q_2 = 100$. THE SOURCE AND ARRAY OF DETECTORS HAVING A DETECTOR SPACING OF 2 m ARE IN THE BEDROCK.



(a) The quality factor of the surface layer is $Q_1 = 50$.



(b) The quality factor of the surface layer is $Q_1 = 10$.

FIGURE IV-17. SYNTHETIC SEISMOGRAMS OF SCATTERED SH-WAVES ONLY FROM A 2-m DIAMETER CYLINDRICAL CAVITY LOCATED IN A TWO-LAYER LOSSY HALF-SPACE AT A DEPTH OF 50 m. THE SURFACE LAYER THICKNESS IS 5 m. THE CONSTITUTIVE PARAMETERS OF THE SURFACE LAYER AND THE BEDROCK ARE $c_1 = 200$ m/sec, $\rho_1 = 1500$ kg/m³, $c_2 = 2500$ m/sec, AND $\rho_2 = 2700$ kg/m³. THE QUALITY FACTOR OF THE BEDROCK IS $Q_2 = 100$. THE SOURCE IS IN THE BEDROCK, AND THE ARRAY OF DETECTORS

Figures IV-18 and IV-19 show the comparative effects of surface layer thickness on the tunnel-scattered SH waves. In Figure IV-18, where the SH-wave source and detectors are in the competent bedrock layer, the tunnel detector responses are not significantly affected by the surface layer thickness. In comparison, the responses in Figure IV-19, where the source is in the bedrock but the detectors are at the top of the surface layer, show a significant (53 percent) increase in propagation time of the scattered waves as well as a noticeable loss of the finer details of the detected waveform, all of which is attributable to the added surface layer thickness. The more realistic case where the quality factor of the surface layer is $Q_1 = 10$ instead of $Q_1 = 50$ may be examined by comparing Figures G-3 and G-4, G-11 and G-12 in Appendix G to show even greater effects of layer thickness on the tunnel detection response.

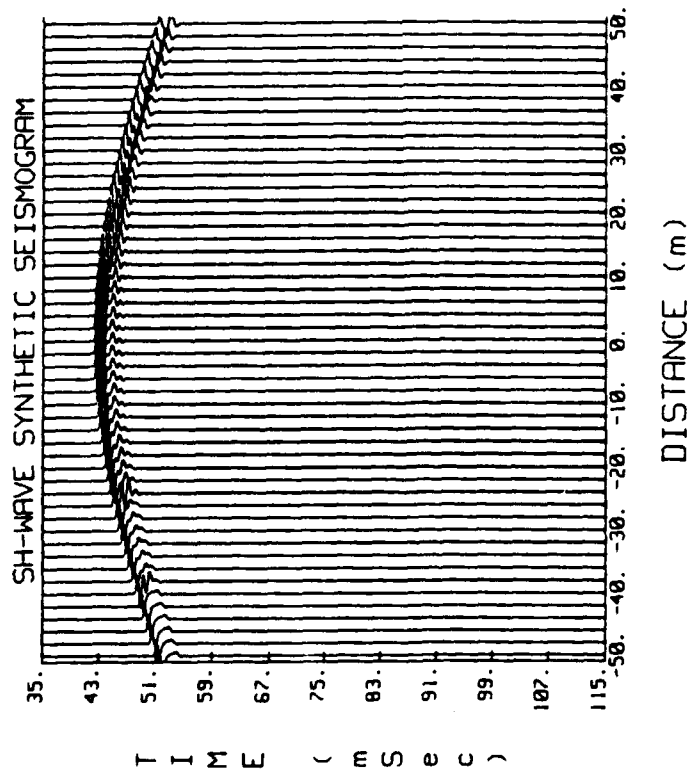
3. Effect of Surface Layer SH-Wave Velocity

Examples of synthetic seismograms from Appendix G are discussed below to demonstrate the effects of different SH-wave velocity conditions in the surface layer on the detection of the tunnel cavity. For this purpose, the SH-wave line source is in the bedrock layer and the tunnel cavity depth is selected to be $H = 50$ m and the surface layer quality factor is selected to be $Q_1 = 50$. The thickness of the surface layer is $h = 5$ m, and the SH-wave velocities to be compared are $c_1 = 200$ m/s and $c_1 = 500$ m/s, respectively, for the SH-wave detectors located in the top of the bedrock layer (Figures G-1 and G-20 of Appendix G) and at the top of the surface layer (Figures G-9 and G-24 of Appendix G).

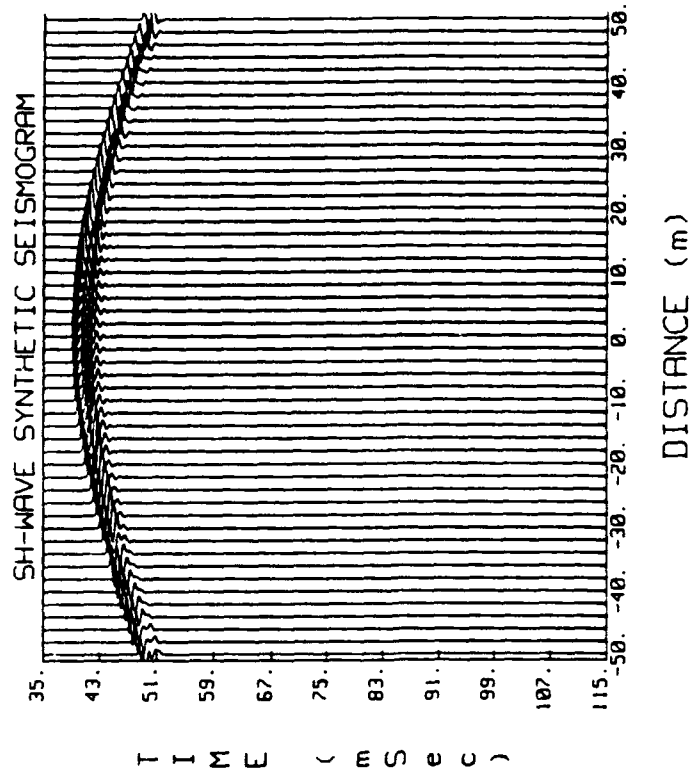
Figures IV-20 and IV-21 show the comparative effects of SH-wave velocity in the surface layer on the tunnel-scattered SH waves. In Figure IV-20, where source and detectors are in the competent bedrock layer, the tunnel detector responses are not significantly affected by differences in the surface layer velocity. [The multiple reflections within the surface layer have been numerically suppressed in Figure IV-20(a) but not in Figure IV-20(b)]. In comparison, the responses in Figure IV-21, where the source is in the bedrock layer but the detectors are at the top of the surface layer, show a significant (21 percent) decrease in propagation time of the scattered waves and a slight but noticeable increase in the curvature of the hyperbolic pattern characteristic of the tunnel target as a localized reflector. In this case, since only the SH-wave velocity of the surface layer was changed without a change in the quality factor, the details in the detected waveforms shown in Figures IV-20 and IV-21 are essentially unaffected.

4. Direct-Wave Interference

The direct wave transmitted from the SH-wave source into the surface layer will cause SH waves to be trapped in the low-velocity layer, giving rise to SH-wave groundroll interference. The trapped SH waves, known as Love waves, propagate as normal modes which are dependent upon the layer thickness and may be excited when the source is located either in the layer or in the bedrock. However, because of the elastic parameter contrasts at the layer interface, the magnitude of Love waves excited by a source below the low-velocity surface layer is significantly less than that produced by a source located in the layer. Examples of Love-wave groundroll interference are illustrated in Figures G-18 through G-20 and Figures G-22 through G-24 of Appendix G.

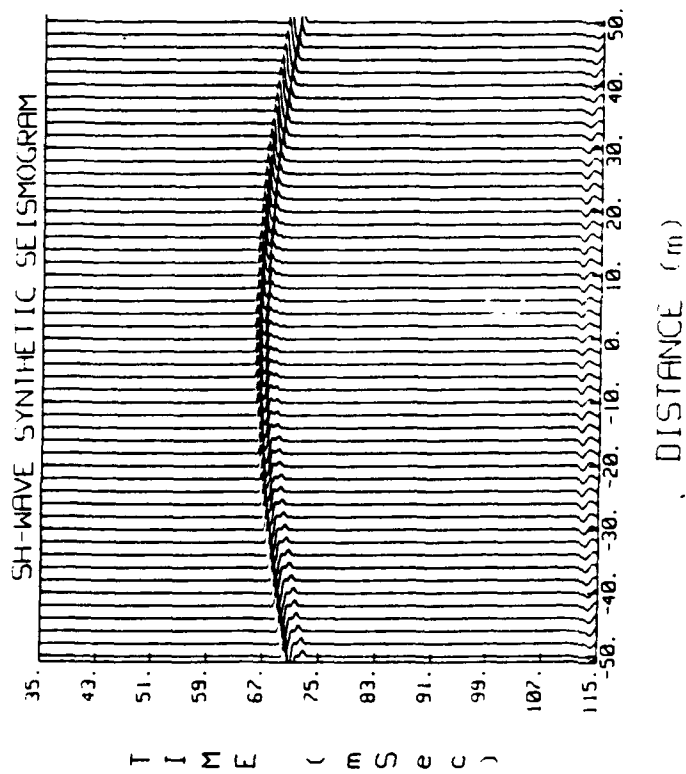


(a) $h = 5 \text{ m}$

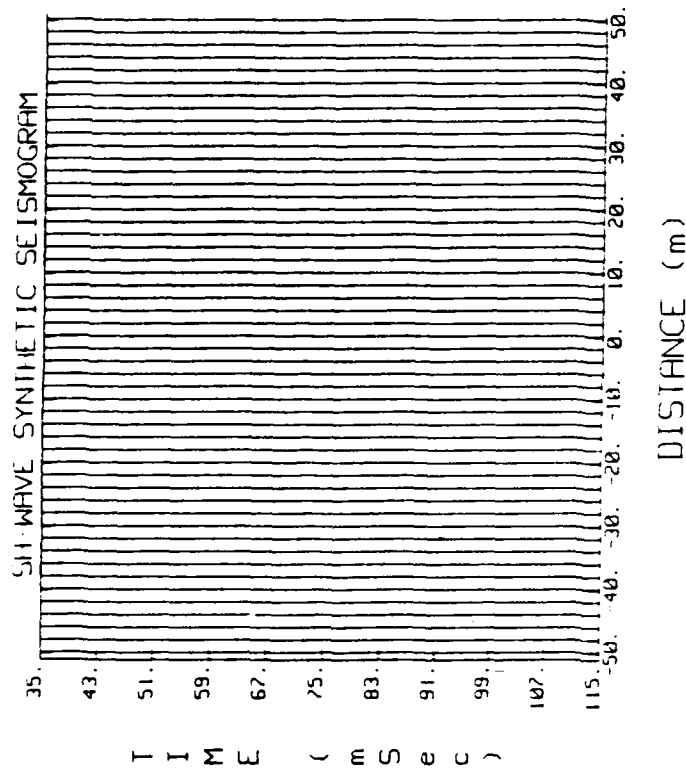


(b) $h = 10 \text{ m}$

FIGURE IV-18. SYNTHETIC SEISMOGRAMS OF SCATTERED SH-WAVES ONLY FROM A 2-m DIAMETER CYLINDRICAL CAVITY LOCATED IN A TWO-LAYER LOSSY HALF-SPACE AT A DEPTH OF 50 m. THE CONSTITUTIVE PARAMETERS OF THE SURFACE LAYER AND THE BEDROCK ARE $c_1 = 200 \text{ m/sec}$, $\rho_1 = 1,500 \text{ kg/m}^3$, $c_2 = 2,500 \text{ m/sec}$, AND $\rho_2 = 2,700 \text{ kg/m}^3$. THE QUALITY FACTORS OF THE SURFACE LAYER AND BEDROCK ARE $Q_1 = 50$ AND $Q_2 = 100$, RESPECTIVELY. THE SOURCE AND THE ARRAY OF DETECTORS HAVING A DETECTOR SPACING OF 2 m ARE IN THE BEDROCK.

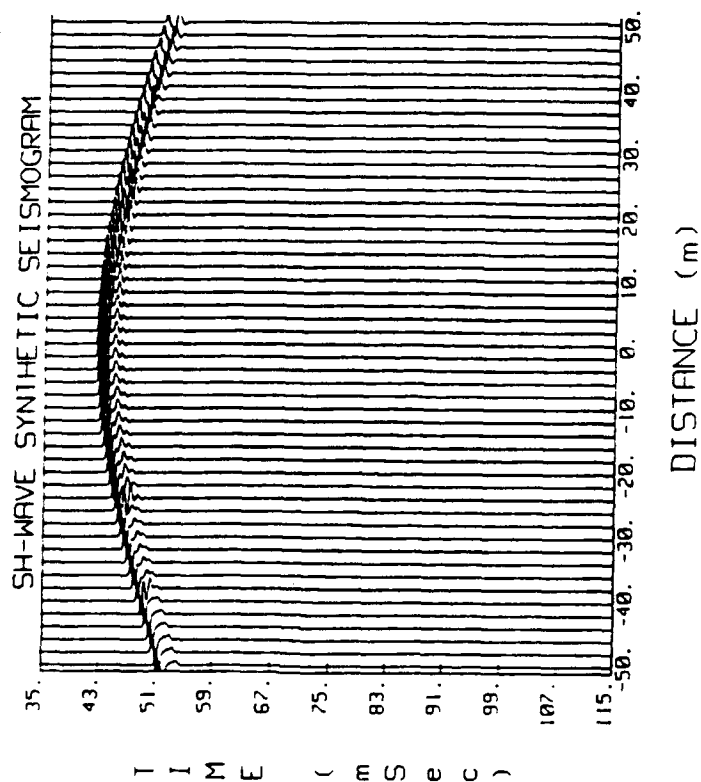


(a) $h = 5$ m

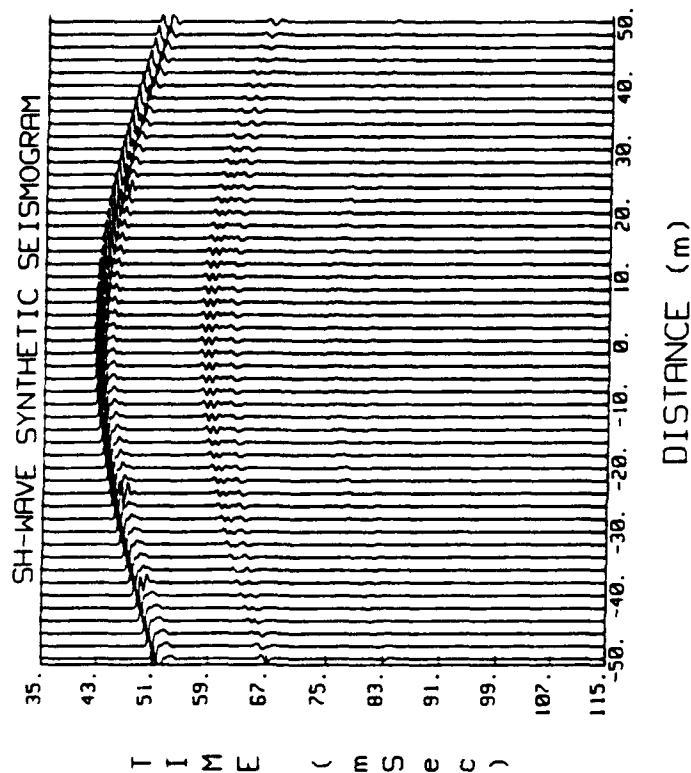


(b) $h = 10$ m

FIGURE IV-19. SYNTHETIC SEISMOGRAMS OF SCATTERED SH-WAVES ONLY FROM A 2-m DIAMETER CYLINDRICAL CAVITY LOCATED IN A TWO-LAYER LOSSY HALF-SPACE AT A DEPTH OF 50 m. THE CONSTITUTIVE PARAMETERS OF THE SURFACE LAYER AND THE BEDROCK ARE $c_1 = 200$ m/sec, $\rho_1 = 1,500$ kg/m³, $c_2 = 2,500$ m/sec, AND $\rho_2 = 2,700$ kg/m³. THE QUALITY FACTORS OF THE SURFACE LAYER AND BEDROCK ARE $Q_1 = 50$ AND $Q_2 = 100$, RESPECTIVELY. THE SOURCE IS IN THE BEDROCK, AND THE ARRAY OF DETECTORS HAVING A DETECTOR SPACING OF 2 m IS AT THE SURFACE OF THE EARTH.



(a) $c_1 = 200 \text{ m/s}$



(b) $c_1 = 500 \text{ m/s}$

FIGURE IV-20. SYNTHETIC SEISMOGRAMS OF SCATTERED SH-WAVES ONLY FROM A 2-m DIAMETER CYLINDRICAL CAVITY LOCATED IN A TWO-LAYER LOSSY HALF-SPACE AT A DEPTH OF 50 m. THE SURFACE LAYER THICKNESS IS 5 m. THE CONSTITUTIVE PARAMETERS OF THE SURFACE LAYER AND THE BEDROCK ARE $\rho_1 = 1,500 \text{ kg/m}^3$, $c_2 = 2,500 \text{ m/sec}$, AND $\rho_2 = 2,700 \text{ kg/m}^3$. THE QUALITY FACTORS OF THE BEDROCK AND THE SURFACE LAYER ARE $Q_2 = 100$ AND $Q_1 = 50$, RESPECTIVELY. THE DETECTOR SPACING IS 2 m. THE SOURCE AND THE ARRAY OF DETECTORS ARE IN THE BEDROCK.

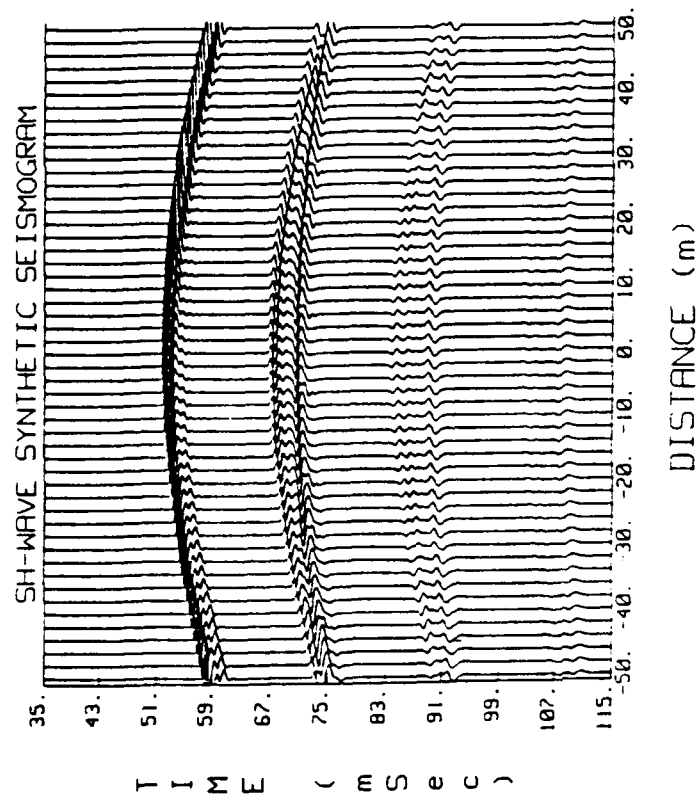
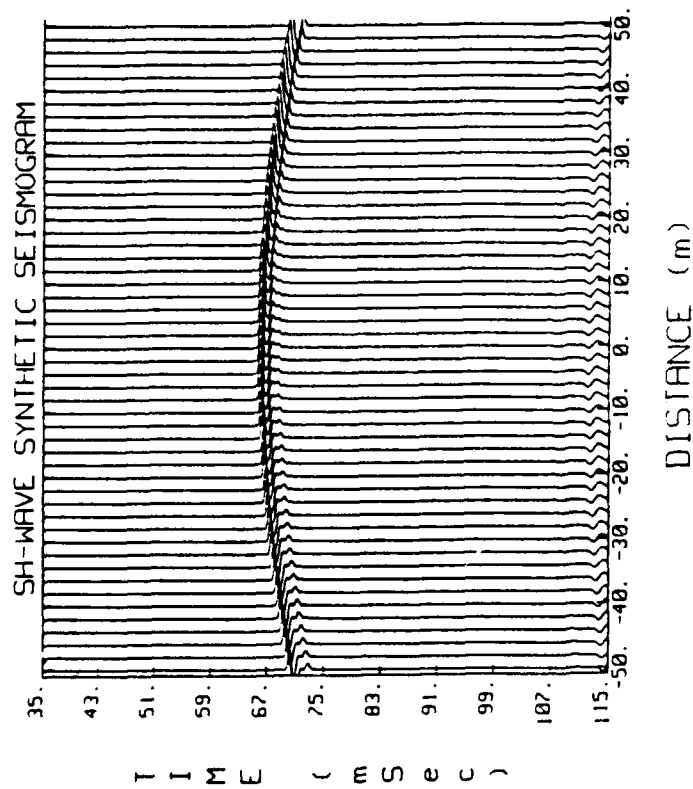


FIGURE IV-21. SYNTHETIC SEISMOGRAMS OF SCATTERED SH-WAVES ONLY FROM A 2-m DIAMETER CYLINDRICAL CAVITY LOCATED IN A TWO-LAYER LOSSY HALF-SPACE AT A DEPTH OF 50 m. THE SURFACE LAYER THICKNESS IS 5 m. THE CONSTITUTIVE PARAMETERS OF THE SURFACE LAYER AND THE BEDROCK ARE $\rho_1 = 1,500 \text{ kg/m}^3$, $c_2 = 2,500 \text{ m/sec}$, AND $\rho_2 = 2,700 \text{ kg/m}^3$. THE QUALITY FACTORS OF THE SURFACE LAYER AND BEDROCK ARE $Q_1 = 50$ AND $Q_2 = 100$, RESPECTIVELY. THE SOURCE IS IN THE BEDROCK, AND THE ARRAY OF DETECTORS HAVING A DETECTOR SPACING OF 2 m IS AT THE SURFACE OF THE EARTH.

V. SPECIALIZED TECHNIQUES FOR SH-WAVE TUNNEL DETECTION

A. Coherent Interference Reduction

A striking result, although not unexpected, in the various SH-wave synthetic seismograms presented in this study, including those computed for the lossy two-layer model, is the relatively weak amplitude of the seismic pulse signal reflected from a deep tunnel target in comparison with the direct arrival signals that travel near the surface between the source and detectors. These large non-target-related signals are coherent with the source pulse and the desired tunnel reflections since they emanate from or are excited by the same source that produces the tunnel reflection signals. Furthermore, if there are other reflecting anomalies in the tunnel host medium, these reflections will also be coherent with the desired tunnel reflection signals. Such coherent interference signals are undesirable for two reasons: (1) the strong direct arrival signals require that the field data recording system have a very wide dynamic range in order to accurately respond to and simultaneously record the very strong direct arrivals and the very weak tunnel reflections without overload distortion or loss of the desirable weak signal content; (2) any strong interference signals that arrive at the detectors simultaneously with the tunnel reflections will mask the desired signals, thereby reducing the tunnel response signal-to-noise ratio.

Most seismic digital data recording systems have a dynamic range of 15 digital bits (90 dB, or 1 part in 31,600) which, if carefully managed through specialized system design and field data acquisition techniques, is sufficient to allow the weak tunnel reflection signals to be accurately recorded. To accomplish this goal, the tunnel reflection signal-to-noise ratio must be maximized using every practical approach and resource available since strong local signals at the detectors and anomalous reflections that can mask the tunnel reflections will generally always be present. The tunnel target response signal-to-noise ratio can be maximized in two ways; namely, by reducing the interfering and/or dynamic range limiting noise and by enhancing the tunnel reflection signal by discriminating against the masking noise. Techniques for applying each of these methods are discussed below.

1. Reduction of Direct Arrival Signals

Direct arrival seismic signals, broadly referred to as ground roll, travel at or near the surface either as surface waves, near-surface body waves, or subsurface interface waves. The direct propagating path of the strongest of these signals may be considered to be essentially horizontal (parallel to the ground surface) whereas the reflection signals from deeper anomalies occur along essentially vertically oriented paths.

The strongest ground roll interference is in the form of surface (Rayleigh) waves which are two-dimensional waves locked to the surface interface and, in a practical sense, extend only a few wavelengths below the surface. They exist and propagate at approximately the same speed as shear waves by interchanging wave motions and energy between compressional and vertically polarized shear displacement motions whenever either of these wave types are initiated by the source or produced by wave-type conversion of

body-wave source signals reflected at the surface. Thus, the SH-wave technique evaluated in this study has the inherent advantage of not directly producing surface waves, provided that its source transducer does not generate either compressional waves or vertically polarized shear waves. Two other advantages of the SH-wave technique which discriminate against surface wave interference and that have been emphasized for the purpose of detecting the tunnel targets of interest are: (1) the seismic wave frequencies that reflect efficiently from a 2-meter diameter tunnel are about 400 Hz or higher and these relatively high frequency seismic waves are strongly attenuated in near-surface geological materials; and (2) the SH-wave source and detectors perform effectively only when they are coupled to the more competent materials below the surface (typically several wavelengths at the Rayleigh wave velocities characteristic of the weathered ground surface for frequencies of 400 Hz and higher). Therefore, the preferred SH-wave techniques for tunnel detection intrinsically discriminate in several ways against surface wave interference.

However, even a pure SH-wave source will generate direct arrival interference in the form of SH body waves. If the source is a broadband impulse transducer, as it must be to fulfill the performance requirements developed in this study, it will also produce unnecessary spectral components in the source pulse signal which are below 400 Hz. Since these low frequency source signal components are not attenuated as strongly as the higher frequency components, they will cause unwanted strong interference at the detectors. However, since this interference is not in the useful frequency range for detecting the small tunnels of interest, they may be removed by means of high-pass filters in the analog preamplifier circuits following each seismic detector transducer. Filters having sharp low-cut response and high stop-band attenuation are needed to effectively remove this source of low-frequency interference which may occur both as near-surface direct arrival signals and as deeper reflections. Therefore, an effective SH-wave tunnel detection system must be designed to effectively reject seismic signals at frequencies below about 400 Hz.

Another method for reducing the requirement for recording the strong direct arrival signals is simply to blank the input to the recording system for an accurately known time delay at the beginning of each recorded detector signal trace. Since the demand for wide dynamic range is imposed by the signals that arrive during the earliest trace time following the source pulse, blanking or strongly attenuating this part of the trace will eliminate the strong interference. This blanking process must generally be designed as part of the first stage of the analog preamplifier in each detector channel in order to prevent overloading the amplifier circuits and it must operate without introducing any other forms of distortion or electrical transient disturbance in the signals to be recorded after the end of the blanking interval. In this regard, most digital seismic recording systems are capable of starting their digital recording after a preset time delay; however, they are not necessarily equipped to block input circuit overloading if it should occur. Therefore, detector circuit blanking in a high-resolution seismic recording system is a technique that may require special electronic circuits to be designed and added to presently available equipment. Furthermore, as will be discussed later in connection with seismic static corrections, there is an auxiliary need to record direct arrival signals as an adjunct to successful tunnel detection, thus complicating the use of the trace-blanking technique.

2. Tunnel Reflection Signal Enhancement

The amplitude of a seismic pulse signal reflected from the tunnel target is directly proportional to the source signal amplitude (or, equivalently, to the source energy) which causes the reflection. Thus, tunnel reflections may be increased by increasing the source level provided that no undesirable effects such as loss of high-frequency spectral content through plastic deformation of the ground at the point of source coupling or by requiring unwieldy source devices or power supplies. However, a low-energy source may be employed for the same purpose by repetitively operating it to provide signal averaging enhancement of the weak tunnel reflections. This process, more precisely known as repetitive transient signal averaging, is capable of enhancing only the signal-to-noncoherent-noise ratio since any interference signals that are coherent with the desired tunnel reflections will be equally enhanced. Therefore, this process has the effective advantage of combining the energy of each repeated source pulse (by taking the repetitive source pulse time necessary to do so) to finally correspond to the energy level of a larger source. However, to be successful in significantly increasing the effective source level, the pulse signal produced by the repetitive source transducer must have an output pulse (radiated into the geologic medium) which is particularly stable in pulse timing and waveform. A new SH-wave source transducer that operates on the arc discharge principle is available to meet these requirements. The details of this device design are presented later.

Spatial signal averaging (or spatial filtering) is a means for reducing the masking effects of seismic reflections that are simultaneously received at the detectors. This method involves adjusting the times of two or more detector output traces recorded from a given source pulse but at different detector positions so as to cause the summation of the traces to overlay and advantageously add the reflected signals from the tunnel target while, as a result of this special trace time adjustment, the signals which come from other reflectors located away from the tunnel combine in a more random way. Thus, by effectively focusing the detector array on the reflections coming from a given point (the tunnel target) in the subsurface medium, those reflections will be enhanced relative to the other coherent signals whose origins or reflections are located away from the tunnel position. To accomplish this target signal enhancement data processing analysis, however, the detector positions must be relatively close together to eliminate spatial aliasing of the focal point mentioned above and the information used to adjust the trace times must be very accurate since the pulse waveforms in the tunnel reflections must be overlaid with good precision in order to produce the desired signal enhancement effect. The information used in the trace time adjustments includes data on the spacings and elevations of the source and detector positions and estimates or measurements of the seismic wave velocity profiles along the presumed propagation paths for the tunnel reflections, starting at the source location and ending at the detector locations being analyzed. Since these time adjustments must be more accurate than the time period of the basic frequency characterizing the pulse waveform, the realization of this demanding form of spatial signal averaging must be viewed as an investigative development to be studied and perfected as part of a specialized data processing and analysis program for high-resolution tunnel detection.

3. Static Corrections

Static corrections of seismic records pertain to time adjustments of the digitally recorded data to facilitate the spatial signal processing techniques such as the spatial filtering technique described above and to adjust the individual detector traces for variations in source and detector spacings and elevations as well as variations in the seismic wave velocity such as may be introduced by the irregularly weathered surface.

In the intended military field application environment of the tunnel detection system in Korea, the terrain relief is generally extreme and will require careful static parameter measurements to yield high-quality tunnel search and detection results. Accurate seismic propagation velocity profiles along the survey traverse in high relief terrain are difficult to infer from simple field tests and may be assumed to vary significantly between contrasting land forms such as ridges and valleys. To provide this needed velocity data, specialized field measurements may be performed as part of each tunnel detection sounding to be separately analyzed to yield site specific velocity information for each new source position and detector spread occupied along the survey traverse. These measurements entail recording the direct arrival signals without specific concern for acquiring reflections from possible tunnel targets. For example, when the geologic section being surveyed consists of a surface soil layer overlying bedrock, the tunnel detection system will be suitable for conducting reflection mapping surveys of the depth to the bedrock interface under and along the detector spread. An effective method for mapping the depth profile of irregular bedrock interfaces has been demonstrated by Hunger, et al. (1984) and applied to low-velocity soil layers 20-30 m thick overlying karst limestone bedrock by Singh (1984a; 1984b). In this method, designated as the reflection window technique, the source offset distance relative to the near-trace detector position must be sufficiently large to allow the bedrock reflections (traveling through the surface layer) to be detected before the direct-ground roll interference arrivals but not so large as to allow the faster-traveling refraction waves (along the surface layer-bedrock interface) to mask the bedrock reflections. This same survey layout can also be used to conduct refraction survey measurements along the soil-bedrock interface to yield information on the velocity in the bedrock layer. Both compressional and shear waves may be employed in these measurements. The detector spacings considered optimum for tunnel detection will also be appropriate for both reflection window mapping and for refraction surveys.

In addition to utilizing direct arrival measurements for determining accurate velocity determinations, supplemental measurements and quick-look field analyses can also be performed on the direct arrival signals to determine whether or not the source and detector transducers are coupled in ground of sufficiently high quality to support SH-wave operations in the desired frequency range of 400-1,600 Hz for efficient detection of the tunnel targets of interest.

B. Use of Tunnel Reflection Models in Data Analysis

The analytical and numerical models for SH-wave reflections from cylindrical cavities developed in this study have provided useful insights

into the nature of the tunnel detection problem as well as guidance for developing an effective tunnel search and detection system. In addition, these models and their variations and extensions also offer a powerful aid in analyzing the expected field survey data. The value of these models is that, given the experimental parameters of the geologic media being explored, the models can provide approximate predictions of any tunnel reflection responses that may be present. Even though such idealized predictions only approximate the actual field data, they are free of geologic noise and can provide a useful template of seismic traces and seismogram patterns that will be representative of the tunnel response. Then, by using such trial templates containing expected target responses, the model calculations may be employed as matched filters to be correlated and compared with the field survey data to extract any similar responses that may be present in the experimental records.

By applying this forward modeling approach to the field data, the information content in an entire seismic section of data becomes involved in a unique process of tunnel target response matching and extraction without the problems of instability or nonconvergence often encountered in geophysical data inversion when applied to low signal-to-noise ratio field recordings.

In order to apply this model-based data analysis technique, the field data must be processed to a certain reference status and format against which a similar ensemble of model-predicted data for various possible tunnel locations with respect to the experimental survey traverse may be compared. The processing and preconditioning the field data consists mainly of applying static corrections and velocity analysis for the field site conditions associated with the data and application of any data preprocessing options such as the spatial signal averaging technique designed to improve the tunnel response signal-to-noise ratio. By means of more advanced models developed to include compressional waves and vertically polarized shear (SV) waves, more complete insights into the complete tunnel detection problem will be gained. With this information available, additional advanced data processing techniques may be considered which employ both radial and transverse horizontal particle motion components recorded along the seismic survey line and a more general analysis based upon three-component vector displacements recorded at each detector position. An important method used in the processing and analysis of oriented three-component seismic survey data is that known as the "polarization method" reported by Gal'perin (1985) in connection with vertical seismic profile data analysis. With this method, reflected signals from the tunnel target can be separated from certain noise components by deriving spatial displacement vectors versus time (depth) so as to maximize the desired tunnel reflection signal-to-noise ratio. This method should be particularly applicable to high-resolution seismic surveys in complex geological formations as well as provide an effective means of minimizing the interference of surface waves and other near-surface coherent seismic noise.

C. Field Data Acquisition System

The seismic data acquisition system required to provide effective tunnel search and detection is a high-resolution reflection survey system

equipped specifically to employ the SH-wave techniques identified in the foregoing model studies. In particular, this system must consist of:

(1) Portable Seismic Data Recording System

- 48-channel digital data acquisition controller
- 48-channel preamplifier and filter unit
- Digital tape recorder
- Quick-look post-acquisition field processor
- Data display plotter
- Power supply

(2) Seismic Detectors and Field Cable

- Three-component geophone assembly designed for borehole clamp coupling and orientation (48 units)
- Multiconductor seismic cable designed for use with three-component geophones with recorder system connection jumpers (typical detector spread length: 240 m)
- Roll-along switch capable of being adapted for use with one-, two-, or three-component detector stations (typically 240 geophone pairs, programmable, manual operation)

(3) SH-Wave Seismic Source

- Arc discharge pulse transducer designed for operation in water-filled boreholes (equipped with orientation capability and bowspring centralizer)
- Surface power supply and control unit

(4) Borehole Auger Drill

- Truck-mount drill system (4-inch diameter, 50-foot depth capacity)

1. Portable Seismic Data Recording System

The high-resolution seismic data acquisition system must be capable of accurately recording multichannel signals in the frequency range of 400 Hz to 1600 Hz with trace time durations up to about 0.5 second in each channel. This frequency response will require digital sampling of each of the preamplifier analog detector signals at a rate of at least 4,000 samples per second and preferably higher. The dynamic range of the system must be as wide as practical but typically equivalent to 15-bit digital waveform amplitude resolution plus sign bit, corresponding a dynamic range of 90 dB in the digitized sample word. Typical analog-to-digital converters used for this purpose provide a 12-bit floating point mantissa plus sign bit and this 72-dB dynamic range is supplemented with a three-or four-bit gain range control of the analog signal amplifier ahead of the converter to provide an additional 18 dB or 24 dB overall system dynamic range. Thus, for a 48-channel recording system

operating with such an effective 16-bit word length acquired at 4,000 sample words per second and for record lengths of 0.5 second, the digital data storage requirements are 1.54 million bits per shot. If each sample word is recorded as two 8-bit bytes, each shot record will require 96,000 bytes of digital magnetic tape or memory storage. A total of 1,875 shots having 96,000 bytes each can be recorded in SEG-D format on one 10-inch 6,250 bpi reel of magnetic tape.

Certain specialized features are recommended to be incorporated in the data acquisition system to improve its high-frequency response and to limit its response to the most effective frequency range for detecting SH-wave reflections from tunnels. The definition of these features and their technical characteristics are:

- (1) Low Cut Filters: 400 Hz cut-off frequency
-60 dB/oct stop-band attenuation
- (2) Passband Emphasis: +24 dB/oct 400 Hz to 1600 Hz
- (3) Digital Sampling Rate: Increase from 4,000 samples/sec
to 8,000 samples/sec (goal)
- (4) Alias Filters: 2,000 Hz cut-off frequency
-72 dB/oct stop band attenuation
- (5) Digital Parallel Data Output Interface.

A digital recording system of this type will effectively eliminate low-frequency ambient noise and will compensate for much of the frequency-dependent absorption loss imposed by the geologic medium. Such a system configured to have 48 channels will accommodate 16 three-component seismic detectors.

Quick-look post-acquisition data processing will be used to yield information on the quality of the recorded data and the nature of the subsurface conditions currently being encountered along the survey line. The processing capabilities needed include digital filtering, trace cross-correlation, normal moveout corrections, common offset gathers, and common depth point stacking. On the anticipation that the quality and usefulness of the high-resolution seismic exploration data necessary for detecting tunnels will be difficult to determine in practice, this quick-look in-field processor can ensure that further more extensive data analysis will yield the desired results.

2. Seismic Source Transducer

High-resolution seismic exploration for tunnels requires that the source and detector transducers be coupled to competent ground so as to convey elastic wave signals having frequency content up to about 2,000 Hz. Such coupling cannot be achieved with either the source or the detectors emplaced at the ground surface unless the competent bedrock tunnel host formation happens to outcrop along the desired seismic survey line. Therefore, in general, the source and detector transducers must be designed to operate in boreholes drilled to reach subsurface ground conditions which are competent enough to support high-frequency elastic waves.

An efficient broadband seismic pulse transducer technique was recently developed by Southwest Research Institute for use in high-resolution borehole seismic applications (Peters and Owen, 1985). This transducer is capable of generating accurately repetitive pressure pulse waveforms in fluid-filled boreholes to produce elastic wave pulses in the drilled geological formation. The transducer operates by producing a high-energy-rate electric discharge in a self-contained aqueous electrolyte solution to produce intense pressure pulses. Electrical energy up to approximately 1,000 joules is stored on a high-voltage capacitor and is discharged in the arc chamber within a time interval of a few hundred microseconds to produce a positive pressure pulse having a peak pressure of several atmospheres. This arc discharge generator may be operated at a pulse repetition rate of approximately 10 pulses/min in boreholes 4-6 inches in diameter.

Figure V-1 illustrates the general design concept of the electric arc discharge pulse transducer. This figure shows the cylindrical electrodeless arc discharge chamber in which a small channel of liquid electrolyte is vaporized to produce the plasma arc discharge pressure pulse. This pulse is coupled to the borehole fluid through the flexible cylindrical sleeve forming the electrolyte chamber. Such pressure pulses are generated each time the charged high-voltage capacitor is switched across the electrodes on the upper and lower ends of the chamber.

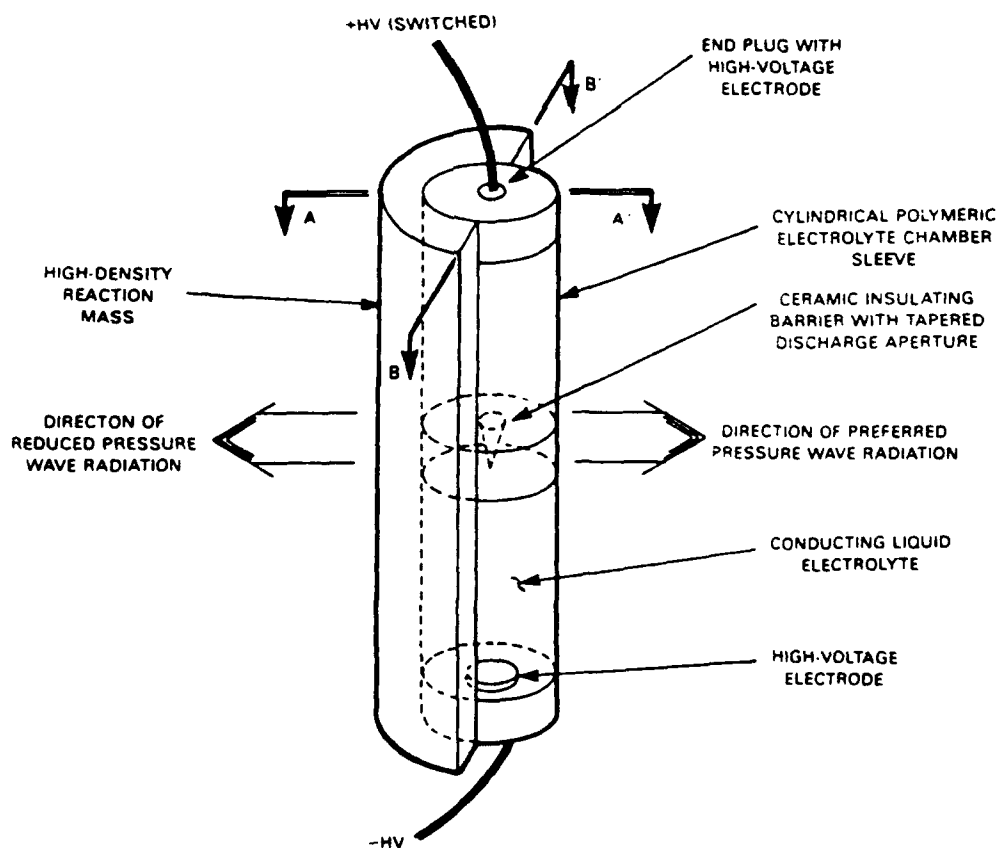


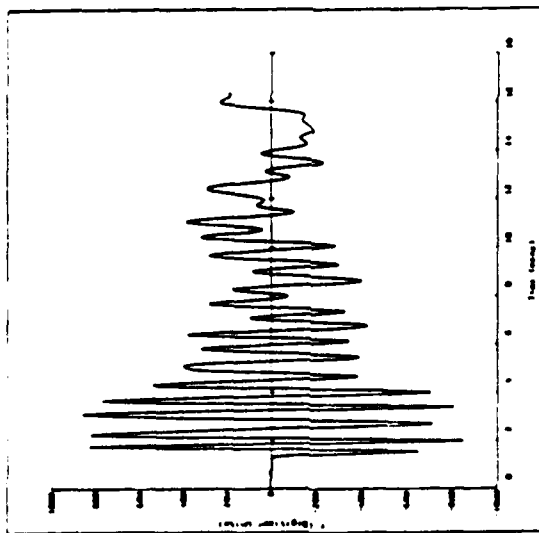
FIGURE V-1. ELECTRODELESS ARC DISCHARGE TRANSDUCER FOR GENERATING ASSYMETRICAL LATERAL FORCE IN A BOREHOLE

The high-density reaction mass shown surrounding one half of the arc discharge chamber in Figure V-1 serves to produce the asymmetrical lateral force in the borehole necessary for exciting horizontally polarized shear waves. The asymmetrical force is oriented in the plane A-A' and horizontally polarized shear waves are radiated away from this point source transducer in the plane B-B'.

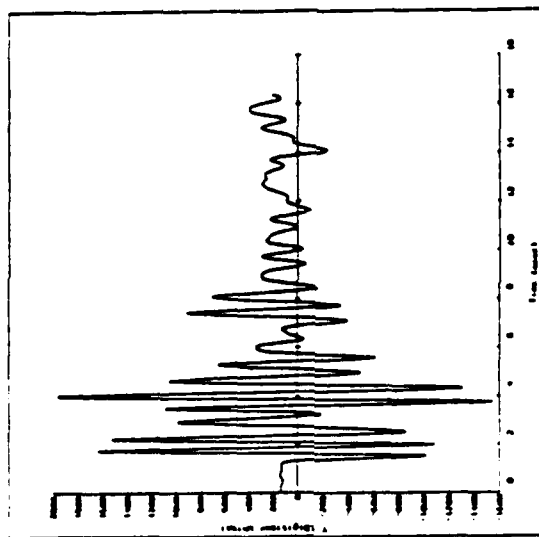
A vertical array consisting of several devices of this type spaced at a distance about 0.5 meter (less than one-half wavelength at the highest frequency of interest) and timed to produce a downward end fire-directed pulse can provide a very efficient controlled source of SH waves for tunnel detection. For example, an array of ten SH-type arc discharge elements in a 4.5-meter long array will produce a 30-degree half-power radiation beam pattern at a frequency of 1,000 Hz. An array of this type would provide a total energy of 5,000 joules per pulse in a water-filled borehole approximately 4 inches in diameter drilled to the depth required to reach the competent geological medium.

In the general form described above, the basic borehole arc discharge transducer can be designed to generate either SH-wave pulses (with reaction mass attached) or compressional wave pulses (without reaction mass attached). Preliminary SH-wave pulse experiments were recently conducted using the U.S. Bureau of Mines 500-joule arc discharge source probe with a lead half-cylinder reaction mass attached. Figure V-2 illustrates the results of these preliminary tests in which the source transducer having the reaction mass attached was placed in one water-filled borehole in a limestone formation and a hydrophone detector was placed in a second water-filled borehole located approximately 3.05 meters away from the source. Figure V-2(a) shows the compressional wave pulse waveform transmitted horizontally between the boreholes without the lead reaction mass attached to the source transducer. With the reaction mass attached, the source probe was rotated until the strongest shear wave obtainable was observed superimposed on the compressional wave pulse. Figure V-2(b) shows the superimposed SH wave and indicates the shear wave velocity in the limestone to be about 50.1 percent of the compressional wave velocity. The hydrophone was then lowered in two-meter depth intervals below the source to show the improved SH-wave/P-wave ratio characteristic of the downward (and upward) directed SH-wave radiation from the source transducer. The SH wave pulse signals detected at downward depth offsets of 2, 4, and 6 meters are shown in Figures V-2(c) through V-2(d). The SH-wave pulse signals observed in these tests are judged to be much stronger than the compressional wave pulses since the hydrophone detector used in the experiments is not well suited for the detection of shear waves. These tests indicate that the asymmetrical force generated around the circumference of the borehole by this arrangement is effective in generating SH wave pulses.

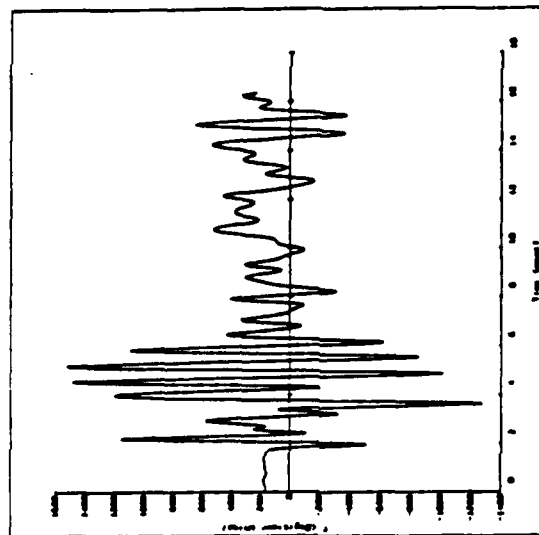
The SH-wave source transducer must be oriented so that its asymmetrical force is directed transverse to the seismic survey line. For this purpose, the SH-wave source transducer must be equipped with a clamping mechanism by which it may be held at a fixed orientation. A detachable metal suspension tube of square cross-section may be used to handle and orient the source transducer in the proper direction and hold it in place in the relatively shallow boreholes anticipated for field use while the clamping mechanism is operated.



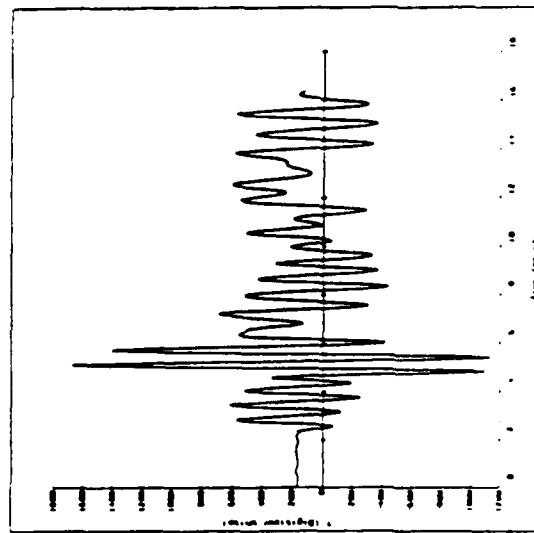
(a) Without Lead Reaction Mass Attached
Source Depth = 42m
Detector Depth = 42m



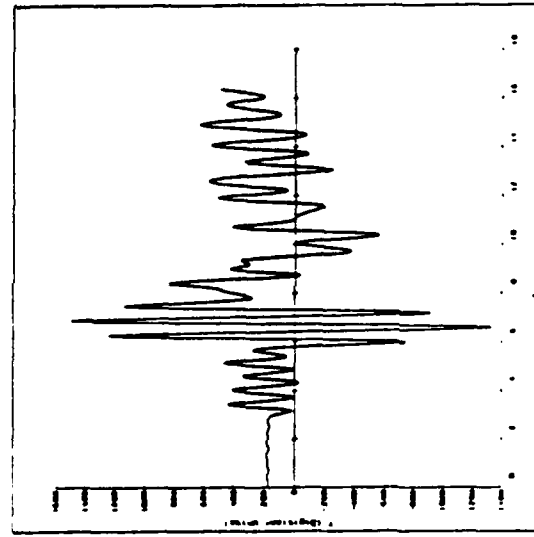
(b) With Lead Reaction Mass Attached
Source Depth = 42m
Detector Depth = 42m



(c) With Lead Reaction Mass Attached
Source Depth = 42m
Detector Depth = 44m



(d) With Lead Reaction Mass Attached
Source Depth = 42m



(e) With Lead Reaction Mass Attached
Source Depth = 42m

FIGURE V-2. PRELIMINARY TESTS OF ARC DISCHARGE PULSE TRANSDUCER MODIFIED TO PRODUCE ASYMMETRICAL PRESSURE FORCE ON BOREHOLE WALL TO GENERATE HORIZONTALLY POLARIZED SHEAR WAVES

3. Seismic Detector Transducers

Precision digital-grade three-component seismic detectors are required for use with the high-resolution seismic exploration system. In addition, each of these detectors must be equipped with a clamping mechanism by which it may be rigidly coupled to the borehole wall. With such mechanical coupling, the detector boreholes are not required to have a borehole fluid content.

The seismic detectors recommended for use with the system are acceleration sensitive geophones mounted in a three-component configuration. The seismic detectors should be mounted on a specialized triaxial-sensor borehole-conforming contact shoe which will be rigidly locked against the borehole wall by means of a pneumatically-expanded rubber pressure boot. A detachable metal suspension tube of square cross-section or other device may be attached to this downhole assembly to allow it to be handled and oriented in the proper direction and hold it in place while the clamping boot is being inflated. An air compressor and pressure regulating control unit will be needed to supply pneumatic inflation of the boots. The combination geophone cable and inflation air hose on the downhole detector units will be designed to allow retrieval of the unit.

4. Custom Seismic Survey Cable

Reflection and refraction seismic exploration for tunnel targets will require a special-purpose detector layout cable having a sufficient number of electrical conductor-pair circuits and interval-spaced take-outs to connect the planned spread of seismic detectors to the 48-channel seismic data acquisition system. This cable must have groups of three conductor-pair take-outs per detector station to accommodate the use of three-component geophone sensors at each station when desired. The three take-outs at each station should be spaced 0.5 meter apart and color coded to represent the connections for the x-horizontal, y-horizontal, and z-vertical geophones contained in the borehole detector assemblies. Each borehole detector station must be emplaced along the seismic line at approximately 2.5 meter spacings to prevent spatial aliasing in the field data, and the cable interval spacing between take-outs should be 2.75 meters. The cable should also be segmented in hanks of 66 meters length with 24 detector stations per segment and color-coded end connectors which will allow each segment to be moved forward and properly connected to the leading end of the cable on the survey line after each 24 source shots are completed. Since the 24 three-component detectors will require 72 conductor pairs, the total number of conductor pairs for a three-segment cable layout ($3 \times 66 \text{ m} = 198 \text{ m}$ length) will be 216 pairs. This number of pairs can be conveniently switched into the 48-channel data recording system using a standard 240-detector-station roll-along switch. This relatively large number of conductor pairs (216 pairs) can be reduced to 144 pairs and still allow the use of three cable segments if multiple take-outs are used in operating the composite cable. With this arrangement, the multiple take-outs on the conductor pairs are separated 48 detector stations apart so that no two detectors are simultaneously attached to the same pair to introduce erroneous signals into the recorded data. The roll-along switch is programmed to switch the conductor pairs by being back-wired to pick up appropriate repeat connections to the previously used pairs having detectors at new forward take-out positions. The 66-meter cable hanks having 24 three-component take-outs and 144

conductor pairs are estimated to have a weight of approximately 50 pounds using #28 AWG conductors in each pair for good cable strength and reliability in the field.

Next, by operating the seismic data acquisition system in a split-spread configuration composed of two three-hank cables as described above, the same cable design and 240-detector roll-along switch can be used to cover twice the total traverse line length for each setup of the data recording system (truck). This is accomplished by means of a patch panel by which the individual geophones (conductor pairs) are prewired to configure the desired detectors (i.e., single-vertical, single-horizontal, dual-horizontal, or three-component) to be sequentially selected by the 240-detector roll-along switch without overflow of the number switch positions. The use of the patch panel also allows the selected detectors to be directly connected to their analog preamplifiers and low-cut filters ahead of the roll-along switch for maximum signal-to-noise ratio.

5. Roll-Along Switch

The system must be equipped with a 240-circuit roll-along geophone switch to accommodate the special seismic cable and detector pairs as configured by the patch panel used to set up the detector stations for field operations. Roll-along switches of this type are conventional components which are commercially available from several suppliers.

6. Borehole Auger Drill

A light-duty shallow borehole auger drill is required as a permanent part of the high-resolution seismic system since efficient operation of the system is expected to require the use of boreholes for source and detector coupling on a regular basis. This drill should have a 3-1/2-inch diameter borehole drilling capability to a nominal depth of 15 meters using spade-bit and auger technology (dry drilling) and a 4-1/2-inch diameter helical screw bit designed especially for enlarging and compacting the augered hole walls to stand open without the need for casing and to provide compacted hole rigidity for good seismic coupling. The boreholes used for the seismic source transducer will require water to be present or added for proper operation. The boreholes used for the seismic detectors will not require water filling for sensor operation.

7. Spare Parts

Spare parts are required for the various system components which receive routine field handling such as the source and detector transducers, cables, borehole clamping mechanisms, borehole drill, and related sub-components. Certain spare electronic modules are also required to maintain the digital data recording system and the arc discharge source transducer system.

8. Field Vehicles

Two field vehicles are required to support the operation of the high-resolution seismic exploration system: a mobile data recording and system transport vehicle, and a dedicated drill truck.

VI. CONCLUSIONS AND RECOMMENDATIONS

The theoretical analyses and computer evaluations of SH-wave seismic reflection techniques carried out in this study have yielded important insights and useful results which demonstrate the feasibility of detecting subversive intrusion tunnels of military interest. Based upon these results, the seismic detectability of tunnels 2 m in diameter at depths of 100 m or more in hard rock geological formations is judged to be technically feasible and practical using SH waves, provided that certain equipment capabilities, field application techniques, and data analysis methods are employed. The primary findings and conclusions gained from this study are:

- (1) Seismic Detectability of Tunnels: Horizontally polarized shear (SH) waves offer certain intrinsic geophysical advantages for detecting tunnels based upon their shorter wavelength at practical seismic frequencies, their reduced tendency to excite surface ground roll interference, and the fact that SH waves do not suffer wave-type conversion losses when reflections occur at geologic interfaces oriented parallel to the shear wave polarization.

Plane wave scattering analysis was used to show the frequency dependence and angular dependence of SH-wave scattering from cylindrical cavities. The effective frequency range for detecting the tunnels of interest is the two-octave band of 400-1,600 Hz since spectral components in the incident wave below 400 Hz provide only a marginal response from the small tunnel cavity cross-section and spectral components above about 1,600 Hz are attenuated significantly and tend to be scattered from the many natural inhomogeneities in the rock formation that are smaller than the tunnel.

- (2) Coherent Interference and Masking: Interference caused by direct seismic waves traveling from source to detector was illustrated in synthetic seismograms derived using homogeneous half-space and two-layer half-space models. For the SH waves modeled, the amplitude ratios of reflections from a 100-meter deep tunnel to the direct arrival ranged from about -32 dB for a lossless half-space to -55 dB for the case where the seismic detectors are located at the surface of a low-quality layer overlying the tunnel host bedrock medium. Table VI-1 summarizes these reflection-to-direct arrival ratios for the various half-space models and tunnel cavity depths evaluated.

These results clearly show the importance of providing a wide dynamic range in the field data acquisition system. The results also present quantitative information on the influences of tunnel target depth on the SH-wave reflections as well as the effects of a lossy surface layer on the detection effectiveness.

- (3) Effects of Low-Quality Surface Layer: The simplified field procedures afforded by the use of surface-coupled seismic detectors greatly diminish the effectiveness of the seismic tunnel detection concept. In the model cases where the detector responses were located at the top of a thin low-quality ($Q_1 = 10$) surface layer, the layer attenuation introduces reductions in the tunnel reflection

TABLE VI-1

RATIO OF SH-WAVE TUNNEL REFLECTIONS TO DIRECT
SH-WAVE INTERFERENCE FOR THE LAYERED HALF-SPACE MODEL

Model Description	(SH-Wave Tunnel Reflection) Direct SH-Wave Amplitude (dB)		Reference Figures in Volume II Appendix G
	Tunnel Depth = 50 m	Tunnel Depth = 100 m	
Two-layer half-space with source and detector in the bedrock.			
Surface layer thickness $h = 5$ m Bedrock quality factor $Q_2 = 100$ Surface Layer $Q_1 = 50$:	-26	-32	G-1 & G-5
Surface Layer $Q_1 = 10$:	-26	-32	G-3 & G-7
Surface layer thickness $h = 10$ m Bedrock quality factor $Q_2 = 100$ Surface Layer $Q_1 = 50$:	-26	-32	G-2 & G-6
Surface Layer $Q_1 = 10$:	-26	-32	G-4 & G-8
Two-layer half-space with source with source in the bedrock and detector at top of surface layer.			
Surface layer thickness $h = 5$ m Bedrock quality factor $Q_2 = 100$ Surface Layer $Q_1 = 50$:	-26	-34	G-9 & G-13
Surface Layer $Q_1 = 10$:	-44	-49	G-11 & G-15
Surface layer thickness $h = 10$ m Bedrock quality factor $Q_2 = 100$ Surface Layer $Q_1 = 50$:	-32	-40	G-10 & G-14
Surface Layer $Q_1 = 10$:	-50	-55	G-12 & G-16

Notes: (1) Cylindrical SH-wave source
(2) 2-meter diameter tunnel

(3) Surface layer $v_{s1} = 200$ m/sec
(4) Bedrock layer $v_{s2} = 2,500$ m/sec

amplitudes of approximately 24 dB compared with the reflection amplitudes detectable in the top of the bedrock. The practical influences of surface geophone coupling efficiency and variability among conventionally deployed detectors can be anticipated to introduce additional losses in the detection of tunnels. The combined effects of surface layer losses imposed on the tunnel target reflections and the stronger direct arrival interference when the detectors are located on the surface lead to the conclusion that effective tunnel search and detection cannot be achieved using surface-coupled seismic detectors.

- (4) Specialized Data Acquisition and Processing Techniques: Field data acquisition and analysis of SH-wave reflections from tunnel targets in field terrain such as the DMZ of Korea require special considerations and techniques not normally used in conventional seismic exploration practice. These requirements stem largely from the high-frequency seismic signals needed for resolving the small tunnel cavities of interest. They include: (1) the use of a subsurface-coupled orientable SH-wave seismic source and subsurface-coupled three-component detectors capable of being oriented relative to the source orientation and survey line layout; (2) special site-characterizing measurements to provide detailed information on the behavior of the very short wavelength signals and corrections for static site conditions such as topographic elevations, seismic velocity variations in near-surface layers, and the thickness and subsurface shear-wave coupling quality of the surface materials; and (3) the use of optimum detector layouts, source locations, and repetitive signal averaging to enhance the tunnel reflection signals during the field data acquisition process so as to provide sufficient quality data for subsequent processing and analysis.

Given high-quality field data, processing techniques for analyzing these data must be applied carefully and with an objective view toward the results because of the complex geological structure of the tunnel host medium. That is, no substantial experience is available to indicate whether conventional data processing algorithms will be effective when applied to the high-resolution seismic survey for tunnel detection. Therefore, while standard methods of velocity analysis and spatial filtering are planned to be used to their fullest extent, supplemental concepts designed to respond specifically to the tunnel target seismic responses are also recommended for investigation and potential use. For this purpose, the computer models developed in this study can be used to provide certain predictions of tunnel target responses which, through proper data comparison methods, may be used as correlation references for selectively extracting tunnel reflections from any spatially complex structural responses.

- (5) Field Survey System Specifications: The hardware components needed to implement the high-resolution SH-wave reflection seismic technique were defined based upon the general findings of the model studies and analyses. These components can be obtained by adapting certain commercial equipment and prototype developments to the indicated needs. For example, a 48-channel digital data recording system capable of providing a 4,000 sample/sec sampling rate and 15-bit

digital resolution is specified as the basic field survey system. Then, by adding special-purpose components such as borehole-coupled detectors capable of providing three-component seismic measurements and sharp cut-off low-cut filtering in each channel, the recording system can be made to respond primarily to high-resolution SH waves in the frequency range of 400-1,600 Hz.

Another specialized component part of this system is a borehole SH-wave source capable of generating horizontally-polarized pulse signals covering the required frequency range. This requirement can be met by an A prototype arc discharge transducer recently developed for another borehole seismic application using compressional waves has now been demonstrated to be capable of producing the desired SH waves. This component, because of its important features of precision pulse waveform timing, pulse-to-pulse waveform repeatability, broadband seismic frequency spectrum up to about 2,000 Hz, respectable energy level of 1,000 joules/pulse, and efficient operation as either a compressional-wave or shear-wave pulse source, make it an ideal device for this application. The additional system components needed to make the SH-wave reflection seismic survey system complete and fully self-contained were also specified, including a customized seismic field cable, a programmable roll-along switch capable of handling either one-, two-, or three-component seismic detector stations, and a light-duty borehole drill.

- (6) Recommendations: The results of this theoretical and numerical model study of SH-wave detection of tunnel cavities, suggests several recommendations for continuing the studies and applying the results. These recommendations are:
- (a) Implement the specified SH-wave seismic exploration system in prototype form for purposes of experimental deployment, evaluation, and further development;
 - (b) Develop and demonstrate field application procedures and data processing methods which are capable of acquiring high-quality seismic survey data and extracting tunnel target responses under practical field operating conditions;
 - (c) Extend the use of the SH-wave numerical models to other study cases which may be more accurately and more completely representative of the field conditions encountered in the tunnel search and detection environment of Korea;
 - (d) Conduct advanced development model studies in which compressional waves and vertically-polarized waves are incorporated in the analyses. These models will allow the complete responses of tunnels to be studied, including the conversion and interchange of the seismic wave types between compressional and shear waves, the characterization of seismic waves reflected from tunnels which are oriented obliquely with respect to the seismic survey traverse, and the use of these numerical models to produce target-matched responses for possible use in specialized tunnel detection data processing.

REFERENCES

- Achenbach, J.D., Wave Propagation in Elastic Solids, North Holland, Amsterdam, 1975.
- Aki, K. and Larner, K.L., "Surface Motion of a Layered Medium Having an Irregular Interface Due to Incident Plane SH-Waves," Journal of Geophysical Research, Vol. 75, pp. 933-954, 1970.
- Aki, K. and Richards, P.G., Quantitative Seismology, Theory and Methods, W.H. Freeman and Company, New York, 1980.
- Apsel, R.J., "Dynamic Green's Functions for Layered Media and Applications to Boundary Value Problems," Ph.D. Thesis, University of California, San Diego, CA, 1979.
- Bouchon, M. and Aki, K., "Discrete Wave-Number Representation of Seismic-Source Wave Fields," Bulletin of the Seismological Society of America, Vol. 67, No. 2, pp. 259-277, 1977.
- Bouchon, M. and Aki, K., "Near Field of Seismic Source in a Layered Medium with Irregular Interface," Geophysical Journal Research Astronomical Society, Vol. 50, No. 3, pp. 669-684, 1977.
- Brekhovskikh, L.M., Waves in Layered Media, Academic Press, Inc., 1960.
- Buchanan, D.J., "The Scattering of SH-Channel Waves by a Fault in a Coal Seam," Geophysical Prospecting, Vol. 34, pp. 343-365, 1986.
- Cherry, J.T., "The Azimuthal and Polar Radiation Pattern Obtained from a Horizontal Stress Applied at the Surface of an Elastic Half-Space," Bulletin of the Seismological Society of America, Vol. 52, pp. 27-36, 1962.
- Datta, S.K., "Scattering of Elastic Waves," in Mechanics Today, Vol. 4, Nemat Nasser, Editor, Pergamon Press, Oxford, 1978.
- Datta, S.K. and El-Akily, N., "Diffraction of Elastic Waves in a Half-Space I: Integral Representation and Matched Asymptotic Expansions," Modern Problems in Elastic Wave Propagation, J. Miklowitz and J.D. Achenbach, Editors, Wiley Interscience, New York, NY, pp. 197-218, 1978.
- deHoop, A.T., "Modification of Cagniard's Method for Solving Seismic Pulse Problems," Applied Science Research, B8, pp. 349-356, 1960.
- deHoop, A.T., "Pulsed Electromagnetic Radiation from a Line Source in a Two-Media Configuration," Radio Science, Vol. 14, No. 2, pp. 253-268, 1979.
- El-Akily and Datta, S.K., "Response of a Cylindrical Shell to Disturbances in a Half-Space," Earthquake Engineering and Structural Dynamics, Vol. 8, pp. 469-477, 1980.

El-Akily and Datta, S.K., "Response of a Circular Cylindrical Shell to Disturbances in a Half-Space: Numerical Results," Earthquake Engineering and Structural Dynamics, Vol. 9, pp. 477-487, 1981.

Ewing, W.M., Jardetzky, W.S., and Press, F., Elastic Waves in Layered Media, McGraw-Hill Book Company, 1957.

Futterman, W.I., "Dispersive Body Waves," Journal of Geophysical Research, Vol. 67, No. 13, pp. 5279-5291, 1962.

Gal'perin, E.I., The Polarization Method of Seismic Exploration, D. Reidel Publishing Co., 1984.

Gal'perin, E.I., Vertical Seismic Profiling and Its Exploration, D. Reidel Publishing Co., 1985.

Garvin, W.W., "Exact Transient Solution of the Buried Line Source Problem," Proceeding of Royal Society of London, Serie A, Vol. 234, pp. 528-541, 1956.

Grant, F.S. and West, G.F., Interpretation Theory in Applied Geophysics, McGraw-Hill Book Company, New York, 1965.

Greenfield, R.J., "Seismic Radiation from a Point Source on the Surface of a Cylindrical Cavity," Geophysics, Vol. 43, No. 6, pp. 1071-1082, 1978.

Gregory, R.D., "An Expansion Theorem Applicable to Problems of Wave Propagation in an Elastic Half-Space Containing a Cavity," Proceedings Cambridge Philosophysical Society, Vol. 63, pp. 1341-1367, 1967.

Gregory, R.D., "The Propagation of Waves in an Elastic Half-Space Containing a Cylindrical Cavity," Proceeding of the Cambridge Philosophical Society, Vol. 67, pp. 689-710, 1970.

Harrington, R.F., Time-Harmonic Electromagnetic Fields, McGraw-Hill Book Company, New York, 1961.

Haskell, N.A., "Crustal Reflection of Plane SH Waves," Journal Geophysical Research, Vol. 65, pp. 4147, 1960.

Helbig, K., and Mesdag, C.S., "The Potential of Shear-Wave Observations," Geophysical Prospecting, Vol. 30, pp. 413-431, 1982.

Helmberger, D.V., "The Crust-Mantle Transition in the Bering Sea," Bulletin of the Seismological Society of America, Vol. 58, pp. 179-214, 1968.

Hunter, J.A., Pullan, S.E., Burns, R.A., Gagne, R.M., and Good, R.L., "Shallow Seismic Reflection Mapping of the Overburden-Bedrock Interface with the Engineering Seismograph--Some Simple Techniques," Geophysics, Vol. 49, No. 8, pp. 1381-1385, 1984.

Ichikawa, M., Koshaka, S., Komaki, S., and Onda, I., "Theoretical and Experimental Studies of Shear Wave Generator, Part I: Wave Fields Radiated from Several Types of Force Systems," Journal of Physics of the Earth, Vol. 23, pp. 205-218, 1975.

Johnson, L.R., "Green's Function for Lamb's Problem," Geophysical Journal Research Astronomical Society, Vol. 37, pp. 99-131, 1974.

Kamel, A. and Felsen, L.B., "Hybrid Ray-Mode Formulation of SH Motion in a Two-Layer Half-Space," Bulletin of the Seismological Society of America, Vol. 71, No. 6, pp. 1763-1781, 1981.

Kong, J.A., Electromagnetic Wave Theory, John Wiley and Sons, Inc., New York, 1986.

Lamb, H., "On the Propagation of Tremors Over the Surface of an Elastic Solid," Transactions of the Royal Society of London, Vol. 203, Serie A, pp. 1-42, 1904.

Lewis, T.S., and Kraft, D.W., "Scattering of Long-Wave Length Elastic Waves by a Cylindrical Obstacle in a Solid," Journal of Applied Physics, Vol. 47, No. 4, pp. 1265-1269, 1976.

Lewis, T.S., and Kraft, D.W., and Hom, N., "Scattering of Elastic Waves by a Cylindrical Cavity in a Solid," Journal of Applied Physics, Vol. 47, No. 5, pp. 1795-1798, 1976.

Love, A.F.H., "A Treatise on the Mathematical Theory of Elasticity," 4th Edition, Dover Publications, New York, 1944.

Miller, G.F., and Pursey, H., "The Field and Radiation Impedance of Mechanical Radiators on the Free Surface of a Semi-Infinite Isotropic Solid," Proceedings of the Royal Society of London, Serie A, Vol. 223, pp. 521-544, 1954.

Miklowitz, J., "Recent Developments in Elastic Wave Propagation," Applied Mechanics Review, Vol. 13, pp. 865-878, 1960.

Mitra, M., "An SH-Point Source in a Half-Space with a Layer," Bulletin of the Seismological Society of America, Vol 53, No. 5, pp. 1031-1037, 1963.

Morse, P.M. and Freshbach, H., Methods of Theoretical Physics, McGraw-Hill Book Company, New York, 1973.

Newlands, M., "The Disturbance Due to a Line Source in a Semi-Infinite Surface Layer," Philosophical Transaction, Serie A, Vol. 245, pp. 214-307, 1952.

Ohtsu, M. and Uesugi, S., "Analysis of the SH Wave Field in a Half-Space by the Boundary Element Method," Earthquake Engineering and Structural Dynamics, Vol. 1, No. 1, pp. 141-161, 1984.

Onda, I. and Komaki, S., "Waves Generated from a Linear Horizontal Traction with Finite Source Length on the Surface of a Semi-Infinite Elastic Medium, with Special Remarks on the Theory of Shear Wave Generator," Bulletin of the Earthquake Research Institute, Vol. 46, pp. 1-23, 1968.

Pao, Y.H. and Mow, C.C., The Diffraction of Elastic Waves and Dynamic Stress Concentrations, Crane-Russak, New York, 1973.

Parra, J.O., "SH Wave Scattering from a Cylindrical Cavity - Task I-a, Theory," Quarterly Progress Report No. 1 and 2, USAE WES Contract No. DACA39-86-K-0017, SwRI Project 14-1421 (October 1, 1986 to April 30, 1987).

Pekeris, C.L., "The Seismic Buried Pulse," Proceedings of National Academic of Science, U.S., Vol. 41, pp. 629-639, 1955.

Pekeris, C.L., Alterman, Z., and Abramovics, F., "Propagation of an SH-Torque Pulse in a Layered Solid," Bulletin of the Seismological Society of America, Vol. 53, No. 1, pp. 39-57, 1963.

Peters, W.R., Owen, T.E., "A New Boarehole Seismic Probe for Coal Seams and Other Applications," Technical Memorandum, Bureau of Mines Denver Research Center, Contract No. H0212006, February 1985; SwRI Project No. 14-6423.

Reshef, M. and Kosloff, D., "Applications of Elastic Forward Modeling to Seismic Interpretation," Geophysics, Vol. 50, No. 8, pp. 1266-1272, 1985.

Sato, R., "Formulation of Solutions for Earthquake Source Models and Some Related Problems," Journal of Physics of the Earth, Vol. 17, No. 2, pp. 101-110, 1969.

Shah, A.H. and Wong, K.C., "Single and Multiple Scattering of Elastic Waves in Two Dimensions," Journal of Acoustic Society of America, Vol. 74, pp. 1033-1043, 1983.

Singh, S., "High-Frequency Shallow Seismic Reflection Mapping in Tin Mining," Geophysical Prospecting, Vol. 32, pp. 1033-1044, 1984.

Singh, S., "Reflection-Window Mapping of Shallow Bedrock," Geophysical Prospecting, Vol. 34, pp. 492-507, 1986.

Sneddon, I.N., Elements of Partial Differential Equations, McGraw-Hill Book Company, Inc., New York, 1957.

Stinson, D.C., Intermediate Mathematics of Electromagnetics, Prentice-Hall, Inc., New Jersey, 1976.

Tsang, L. and Redar, D., "Numerical Evaluation of Transient Acoustic Waveforms Due to a Point Source in a Fluid-Filled Borehole," Geophysics, Vol. 44, pp. 1706-1720, 1979.

Tygel, M. and Hubral, P., "Transient Representation of the Sommerfeld-Weyl Integral with Application to the Point Source Response from a Planar Acoustic Interface," Geophysics, Vol. 50, No. 12, pp. 2889-2891, 1985.

Ushahov, V.M., Shcherbinskii, and Pervalou, S.P., "Reflection and Transformation of Linearly Polarized Shear Waves by a Plane and by Flaws," Defektoskopiya, No. 7, pp. 70-75, 1983.

Ushahov, V.M., Shcherbinskii, and Vopilkin, "Reflection and Transformation of Linearly Polarized Shear Waves at Defects," Defektoskopiya, No. 9, pp. 17-23, 1983.

White, J.E., Seismic Waves: Radiation, Transmission and Attenuation, McGraw-Hill Book Co., New York, 1965.

White, R.M., "Elastic Wave Scattering at a Cylindrical Discontinuity in Solid," Journal of Acoustic Society of America, Vol. 30, pp. 771-777, 1958.

Wong, H.L., Trifunac, M.C., "Scattering of Plane SH Waves by a Semi-Elliptical Canyon," International Journal of Earthquake Engineering and Structural Dynamics, Vol. 3, pp. 157-165, 1974.

Wong, H.L., and Trifunac, M.D., "Surface Motion of a Semi-Elliptical Alluvial Valley for Incident Plane SH Waves," Bulletin of the Seismological Society of America, Vol. 64, pp. 1389-1408, 1974.